WCAP-17794-NP
Revision 0

November 2013

10x10 SVEA Fuel Critical Power Experiments and New CPR Correlation: D5 for SVEA-96 Optima3

WCAP-17794-NP
Revision 0

10x10 SVEA Fuel Critical Power Experiments and New CPR Correlation: D5 for SVEA-96 Optima3

Uff Bergmann
Mattias Hemlin
Kjell Bergman
Jean-Marie Le Corre

November 2013

Prepared by: Gunilla Norbäck*
Project Management and Administration

Verified by: Patricia Quaglia*
Safety and Licensing

Approved by: Sam Skidmore, Acting Manager *
Fuel Engineering Licensing

*Electronically approved records are authenticated in the electronic document management system.

Westinghouse Electric Company LLC
1000 Westinghouse Drive
Cranberry Township, PA 16066, USA

ABSTRACT

This report describes the development of a new critical power ratio (CPR) correlation for Westinghouse SVEA-96 Optima3 boiling water reactor (BWR) fuel assemblies. This new CPR correlation is referred to as D5. The new D5 CPR correlation for the SVEA-96 Optima3 assembly and the bases for its acceptance are presented in this report.

TABLE OF CONTENTS

LIST OF TABLES

LIST OF FIGURES

1 SUMMARY

This report describes the development of a new critical power ratio (CPR) correlation for Westinghouse SVEA-96 Optima3 boiling water reactor (BWR) fuel assemblies. This new CPR correlation is referred to as D5. The development of the D5 CPR correlation was aimed at a more physical modeling approach, as opposed to just establishing a mathematical correlation with data. In particular, the dryout physics related to the [

]^{a,c}. Thus, a new CPR correlation form is proposed different from the previous general forms for Westinghouse 10x10 SVEA fuel. CPR correlations based on full sets of critical power data have previously been established for the SVEA-96, SVEA-96+, SVEA-96 Optima, and SVEA-96 Optima2 designs.

The new D5 CPR correlation for SVEA-96 Optima3 fuel and the bases for its acceptance are presented in this report.

The D5 CPR correlation introduces [ ]^{a,c}, and has a form that departs from earlier CPR correlations such as the ABBD1.0, ABBD2.0 and D4 CPR correlations documented in References 1, 2, and 8 where the dryout data were correlated by adapting a CPR correlation of the critical quality/boiling length type, [ ]^{a,c}. Significant changes have been introduced in the new D5 CPR correlation relative to the ABBD1.0, ABBD2.0, and D4 correlations. These changes were intended to more effectively capture the physical characteristics of the dryout phenomenon, including during a transient, as well as observed trends in critical power. These improved features can be summarized as follows:
[

]$^{a.c}$

- [
  ]^{a,c}

Based on these new features, the D5 CPR correlation offers a significant improvement to nuclear safety by allowing more accurate determination of the margins to dryout for every fuel rod in the core.

In addition to the improvements in modeling, the D5 CPR correlation is based on a broader experimental database than previously tested. Three different test series have been performed to support the D5 CPR correlation development and are documented in this report. These test series utilized a 24-rod SVEA-96 Optima3 sub-bundle with three different axial power shapes.

The SVEA-96 Optima3 database has the following improved characteristics:

- Test range for mass flow extended to both lower and higher flows.
- Diversity of data more evenly distributed among the three axial power profiles.
- Rod power peaking tests (for R-factor) performed for all three axial power profiles, including at low mass flow.
- Power in single rods reduced to simulate the conditions in rods containing burnable absorbers (Gd) and dummy rods (with zero power) in a repaired bundle.

The above testing scope was feasible thanks to the unique flexibility of the FRIGG thermal-hydraulic loop to quickly change between different radial (rod) power profiles.

The tests include measurements of critical power at pressures between [ ]^{a,c} bar and an inlet subcooling temperature range between [ ]^{a,c} K. The mass flux range in the tests is [ ]^{a,c} kg/(m^{2}s), based on the lower section of the fuel assembly. However, the data collected at mass flux below [ ]^{a,c} had to be removed from the database, due to large uncertainties in the flow measurements. The critical power measurements were performed for [ ]^{a,c} different local power distributions to capture the influence on critical power of various local peaking factors and various peak power rod locations.

The D5 correlation predicts the measured critical powers over the entire steady-state database with a mean error of [ ]^{a,c} and a standard deviation of [ ]^{a,c}. Note that the negative mean error will not be credited in licensed applications.

2 INTRODUCTION

This report describes the development and qualification of a new CPR correlation for the latest generation of SVEA-96 water cross BWR fuel referred to as "SVEA-96 Optima3." The new CPR correlation is named "D5." The SVEA-96 Optima3 fuel assembly is the latest developed design from an evolutionary line of SVEA-96 designs, i.e., SVEA-96, SVEA-96+, SVEA-96 Optima2, and SVEA-96 Optima3 assemblies. These fuel assemblies are all composed of four sub-bundles in a 5x5 lattice configuration with one fuel rod missing. The cross-sectional layout of the SVEA-96 Optima3 fuel design is shown in Figure 2-1.

The incentive for developing the SVEA-96 Optima3 design was to support the current industry move toward higher energy cycles and requests for improved reliability, in particular with regard to the debris fretting failure mode. This goal was accomplished principally by an enhanced spacer design relative to SVEA-96 Optima2.

The general objectives for the new spacer design of the SVEA-96 Optima3 are to:

1. Reduce the risk for fuel damage due to debris fretting.

2. Maintain or improve the excellent dryout performance of SVEA-96 Optima2.

3. Reduce two-phase pressure drop and hence improve core thermal-hydraulic stability performance.

Each of the four sub-bundles of the SVEA-96 Optima3 fuel assembly consists of 24 fuel rods in a 5×5-1 lattice. Three of the fuel rods in each sub-bundle are part-length rods (PLRs). Two of the PLRs are two-thirds of the length of a full-length rod and are placed adjacent to the central channel of the water cross. The third PLR in each sub-bundle is one-third of the length of a full-length rod and is placed in the outer corner of the sub-bundle.

The test sections consist of 24-rod bundles simulating SVEA-96 Optima3 fuel sub-bundles operated in BWRs. Indirectly heated rods connected to several individual rectifier units make it possible to control the local power (i.e., relative rod power) distribution in a simple way to test a wide range of local power distributions. The objectives of these tests and the CPR evaluation program were as follows:

1. Determine the steady-state critical power capability of the SVEA-96 Optima3 assembly over a wide range of simulated BWR operating conditions. The range of BWR operating conditions must be sufficient to provide a CPR correlation that will be acceptable for predicting the critical power behavior of the SVEA-96 Optima3 assembly over the entire steady-state and transient operating range of BWRs for design and licensing applications.

2. Confirm that the D5 CPR correlation for SVEA-96 Optima3 fuel adequately describes the steady-state critical power database. Establish appropriate biases and uncertainties for licensing applications. Since the correlation was developed from steady-state data, it will provide best-estimate CPR values for steady-state applications.

3. Confirm that the D5 CPR correlation for the SVEA-96 Optima3 fuel established under steady-state conditions provides an adequate description of the changes in critical power (ΔCPR) during transients. This confirmation is performed by comparing the CPR predictions for transient conditions with available transient critical power test data. The Westinghouse methodology for performing this confirmation is illustrated for the BISON code documented in Reference 3.

The D5 CPR correlation is intended to be applied for reload safety analysis and core supervision according to the methodologies approved by the U.S. Nuclear Regulatory Commission (US-NRC).

The test matrix was selected to cover the typical steady-state and transient operating range expected for BWRs and to sufficiently cover off-nominal conditions to allow its application to transient and accident conditions. Particular emphasis has been placed on capturing the dependence on local power distributions within the bundle since this is expected to be the major bundle-specific effect.

The D5 CPR correlation developed for SVEA-96 Optima3 fuel introduces a new correlation form, based on [

]^{a,c}. The new correlation was developed based on [ ]^{a,c} steady-state and [ ]^{a,c} transient critical power points utilizing a full-scale 24-rod sub-bundle. The correlation database contains chopped cosine, top-skewed, and bottom-skewed axial power shapes. The critical power measurements were performed for more than [ ]^{a,c} different local power distributions to capture the influence on critical power of various local peaking factors and various peak power rod locations. Of the [ ]^{a,c} steady-state critical power points, [ ]^{a,c} were used to set the correlation form and the majority of the empirical constants. All data points were used to set the rod-specific constants and to evaluate the correlation prediction statistics.

[

]^{a,c}

The ability of the correlation to match the experimental data is reflected by the average percent deviation of the correlation prediction relative to the measured critical power over the entire data range. The D5 correlation for SVEA-96 Optima3 fuel predicts the measured steady-state critical powers with a mean error of [ ]^{a,c} and a standard deviation of [ ]^{a,c} over the entire steady-state SVEA-96 Optima3 database. Note that the negative mean error will not be credited for licensing applications.

Conservative transient application of the correlation has been illustrated for implementation of the correlation in the BISON dynamic system transient code. Power increase and flow reduction transient tests were simulated demonstrating conservative prediction of the onset of dryout.

The evaluation in Section 7 provides an illustration using the BISON dynamic code of the Westinghouse methodology for confirming that the new CPR correlation based on steady-state data conservatively

predicts CPR behavior under transient conditions. This methodology can also be used to confirm that CPR changes during transient events are conservatively treated in other licensed transient codes.

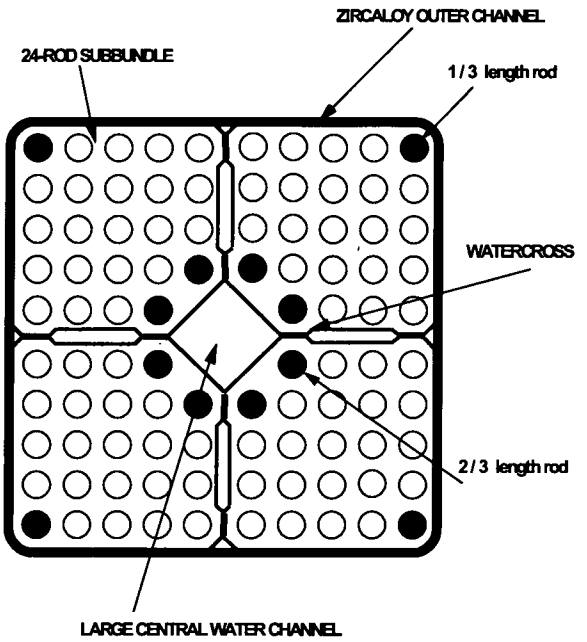

Figure 2-1 Cross Section of SVEA-96 Optima3 Assembly

3 TEST FACILITY

3.1 DESCRIPTION

The SVEA-96 Optima3 critical power tests were performed in the FRIGG loop in the Westinghouse laboratories in Västerås, Sweden. The measurements on SVEA-96 Optima3 started in 2005 with fuel rods of cosine axial power shape (measurement SF24XC) and continued in 2006 by measurements with fuel rods of top and bottom-peaked axial power shapes (SF24XT and SF24XB). The FRIGG loop has been utilized for many years to perform thermal-hydraulic tests in support of the Westinghouse BWR nuclear program.

A diagram of the FRIGG loop is shown in Figure 3-1. The loop contains a main circulation loop with the test section, a cooling circuit, and a purification system. The head of the main circulation pump can be continuously controlled by means of a variable speed motor. When steam is produced in the test section, the loop pressure is controlled by regulating the cold water flow to spray nozzles in the condenser. Heat is removed by a heat exchanger in the cooling circuit from which water is pumped to the spray nozzles. During start-up and heat balance tests, the loop is filled with water, and the pressure is regulated by balancing the amount of water by means of the feedwater pump and a drainage valve. The inlet subcooling is controlled by feeding water from the cooling circuit into the main circulation loop upstream of the pump.

The loop is designed for a maximum pressure of 100 bar and a maximum temperature of 311°C. Carbon steel is used throughout as a construction material, and water quality is carefully controlled. Demineralized and degassed water is used for filling the loop. Purification is continuous during the tests to keep water quality within specified limits. Normally water conductivity is in the range of 0.15-0.30 μS/cm.

3.2 TEST SECTION

The test section consists of a pressure vessel, a Zircaloy flow channel, and a SVEA 5x5-1 sub-bundle with 24 heater rods. Three of the fuel rods in each sub-bundle are part-length rods. Two of the PLRs are two-thirds of the length of a full-length rod and are placed adjacent to the central channel of the water cross. The third PLR in each sub-bundle is one-third of the length of a full-length rod and is placed in the outer corner of the sub-bundle. To avoid deformation at extreme test conditions, the flow channel is reinforced by an outer support structure. Pressure taps are connected to the flow channel at different elevations as shown in Figure 3-3. The pressure transmission lines are brought out of the test section through an instrumentation ring.

An orifice plate is installed at the inlet of the flow channel to provide an even distribution of flow into the channel. The orifice plate has a loss coefficient of five velocity heads, which is close to the lower tie plate with the **TripleWave**™ debris filter losses in standard SVEA-96 Optima3 fuel.

The heated rods are constrained by eight Inconel sleeve spacers on the heated length. Additional Inconel sleeve spacers are positioned at the inlet and outlet of the test section. The axial locations of the spacers and the pressure taps (DP) are shown in Figure 3-3. SP2-XB – SP8-XB, have [ ]^{a,c}

[ ]^{a,c}, but not SP1-XA. Figure 3-2 shows the SVEA-96 Optima3 spacer with [ ]^{a,c}, named XB in Figure 3-3.

The pressure vessel top flange contains pressure seals similar in design to valve stem packing seals which retain the heater rods in fixed position. The difference in thermal expansion between the heater rods and the pressure vessel is off-set via O-ring pressure seals in the bottom flange.

Dimensions of the test sections are compared with SVEA-96 Optima3 design parameters for a core with 3.81 m active length fuel in Figure 3-4. The design dimensions of the SVEA-96 Optima3 test section which might affect dryout are not identical to those of the standard SVEA-96 Optima3 reload fuel assembly. [

]^{a,c}

The numbers assigned to the heater rods in Figure 3-4 are used to identify the heater rods in Appendices A, B, and C. As shown in Figure 3-4, the heater rod numbering scheme identifies the rod location in the sub-bundle.

Table 3-1 through Table 3-3 and Figure 3-5 through Figure 3-7 show the axial power shapes used in the three 24-rod sub-bundle test series.

3.3 HEATER RODS

The heater rods used in the tests are indirectly heated. Each heater rod contains a heater element, electrical insulation, Inconel-600 cladding, and [ ]^{a,c}. The heater element is made from a Monel K-500 tube. The heater element terminals consist of a solid nickel transition piece welded to the Monel tube at one end and to a copper electrode brazed to the Monel tube at the other end. The heater-rod non-uniform axial power profiles were generated by laser cutting a spiral on the Monel tube with a variable pitch.

The power ratings of the heater rods in the test sections at 380V dc are as follows:
[

]^{a,c}

Sketches of a full-length rod and a cosine-shaped axial power distribution two-thirds length heater rod are shown in Figure 3-8 and Figure 3-9, respectively.

[

]^{a,c}

[

]a,c

The electrical insulation was machined from solid boron nitrite (BN) pieces. After the BN sleeves were assembled over the heater element, grooves were cut axially to hold the thermocouples in position. Then the heater element assembly was inserted into the oversized Inconel tube used as cladding. The final heater rod dimensions were obtained by swaging the heater assembly to its final dimensions. The swaging operation also provided good contact between the heater element, the insulation material, and the cladding inner surface assuring good heat transfer with low variability from the heating element to the cladding surface.

The thermocouples (dryout detectors) are embedded between the cladding and the insulation sleeves. The full-length rod thermocouple extensions are routed from the top end of the heater rod, and the part-length extensions are routed from the bottom end. The thermocouples used were 0.5 mm unground, Inconel-sheathed, type K, with Magnesium oxide (MgO) insulation. The thermocouple wire used was of premium grade. The thermocouple tips were backfilled with BN powder and compacted by swaging to provide a faster response to temperature changes.

Figure 3-10 shows the axial positions of thermocouples in the cosine axial power shape sub-bundle tests. Figure 3-11 shows the axial locations of the thermocouples in the 24-rod sub-bundle bottom-peaked axial power shape tests. Figure 3-12 shows the axial positions of the thermocouples in the top-peaked axial power shape 24-rod sub-bundle tests. The radial orientation of the thermocouple just downstream of the end of heated length is also given in Figures 3-10 to 3-12. All eight thermocouples of the full-length rods are distributed evenly at eight radial positions. Under the second and third spacer from the outlet in the cosine rods, and under the first spacer in the top-peaked rods, two radially opposite thermocouples are used. Table 3-1 through Table 3-3 show the axial power shapes used in the three 24-rod sub-bundle test series.

It should be noted that in Figure 3-11 and Figure 3-12 [

]a,c

As shown in Figure 3-12, 15 A-type, 6 B-type, 2 two-thirds-length and 1 one-third-length rods were used in the top-peaked axial sub-bundle tests. [

]^{a,c}

3.4 POWER SUPPLY AND CONTROL

For the sub-bundle tests, electrical power to the heater rods was supplied by a 4.2 MW dc electrical power system operating at 380 V. The system consisted of seven units (rectifiers) rated at 600 kW each, two rectifiers rated at 4000 kW, and two rectifiers rated at 4800 kW.

The upgraded FRIGG loop has a very flexible system for connecting the individual heater rods to selected units. This configuration provides the capability to conveniently obtain numerous combinations of relative rod powers by adjusting the computer signals that control the voltage across each unit. It is this capability which allows a thorough determination of sub-channel factors (e.g., R-factors) providing the relative dryout sensitivity of each fuel rod.

3.5 INSTRUMENTATION

The parameters defining the operating conditions during the tests consist of temperature, pressure, flow, differential pressure, and bundle power. These variables and the method by which they are monitored are defined as follows:

p (bar) is the pressure at the test section outlet. The pressure is measured with a precision pressure transducer in the test section inlet. Estimated accuracy in the measured pressure is ± 0.5 bar.

ΔT sub (°C) is the inlet subcooling. This parameter is defined as the difference between the saturation temperature at the test section outlet and the test section inlet temperature. The temperatures were measured with type-K premium grade thermocouples for the SVEA-96 Optima3 sub-bundle tests. Estimated accuracy in the measured inlet subcooling is ± 1°C.

Q (kW) is the power provided to the coolant by the rod bundle. The power is obtained by the summation of the power generated by each heater rod. Heater rod power is calculated as the product of measured current through each rod multiplied by the measured voltage drop across the rod group in which the heater rods are connected. Heater rod current is measured by a calibrated precision shunt connected to the ground electrical leads.

The bundle power is obtained by reducing the measured power by 0.4% to account for the heat generated in heater rod extensions at the inlet and outlet. This power is dissipated in the flanges and is not delivered to the coolant. The estimated accuracy in measured bundle power is ± 1% of the reading at power levels typical at dryout.

G = $\dot{m}$ /A (kg/m^2/s) is the mass flux. A is the flow area in the lower section of the test bundle at room temperature. The flow rate, $\dot{m}$, is measured with an orifice plate in the recirculation line. The estimated accuracy in G is 20 kg/m^2/s.

[

]^{a,c}

Rosemount differential pressure (D/P) cells, calibrated to an accuracy of ± 0.5% of full scale, were used to measure pressure drops across various part of the bundle and across the main line flow meter. The main line flow meter was equipped with two D/P cells having different ranges in order to minimize the flow measurement error due to errors in differential pressure measurements.

Thermocouples were located at five elevations along the test vessel in order to measure the fluid temperature in the annulus between the pressure vessel and the flow channel (i.e., the temperature in the bundle differential pressure transmission lines).

3.6 DATA ACQUISITION SYSTEM

A typical data acquisition system is shown in Figure 3-13. Signals reflecting important parameters (e.g., temperature, voltage, current differential pressure, and mass flow) are connected to HP3852A data loggers. A sampling frequency of 1.0 Hz was used.

In addition to the data collecting function, the computer was also used as a dryout monitor by utilizing software which allows it to recognize a temperature rise over the initial local temperature in up to 120 heater rod thermocouples. In this case the computer identified the channel(s) indicating dryout. Steady-state dryout is assumed to occur for a minimum measured temperature rise of 25°C.

In addition to the dryout indication, two additional limits were used to protect the bundle. A temperature rise of 50°C and a temperature above 450°C automatically cause a decrease in bundle power of 25%. A temperature rise of 75°C causes the bundle power to be shut off completely.

The dryout monitoring function must be in operation before power is provided to the test section. When dryout was detected, the loop conditions were kept constant for about 20 seconds to clearly define average loop conditions at dryout for that test point.

3.7 CRITICAL POWER TESTING PROCEDURE

The measuring instruments used and the data acquisition system are discussed in Sections 3.5 and 3.6. The tests were recorded in blocks of a maximum size of 2400 samples of each parameter, which corresponds to 2400 seconds at a sampling frequency of 1 Hz. Each block generally included several critical power measurements at different mass flows.

The procedure for establishing critical power was as follows:

1. The test identification number was entered into the computer.

2. The target local power distribution was entered into the computer, which established the corresponding rectifier settings.

3. The target bundle inlet subcooling temperature, system pressure, and mass flux were established.

4. The bundle power was slowly increased in small steps. The power was increased until a temperature excursion exceeding 25°C occurred and triggered an alarm. All the thermocouples were connected to the data loggers, and their outputs recorded during the test. In addition, selected thermocouple outputs were displayed on a monitor in the control room.

Table 3-1 Cosine Axial Power Profile

Node Nr from BHL[1]	Relative Power	Relative Power	Relative Power
(-)	One-Third-Length Rod	Two-Thirds-Length Rod	Full-Length Rod

a,c

Table 3-2 Bottom-Peaked Axial Power Profile

Node Nr from BHL[1]	Relative Power	Relative Power	Relative Power
(-)	One-Third-Length Rod	Two-Thirds-Length Rod	Full-Length Rod

a,c

Table 3-3 Top-Peaked Axial Power Profile			
Node Nr from BHL[1]	Relative Power	Relative Power	Relative Power
(-)	One-Third-Length Rod	Two-Thirds-Length Rod	Full-Length Rod

a,c

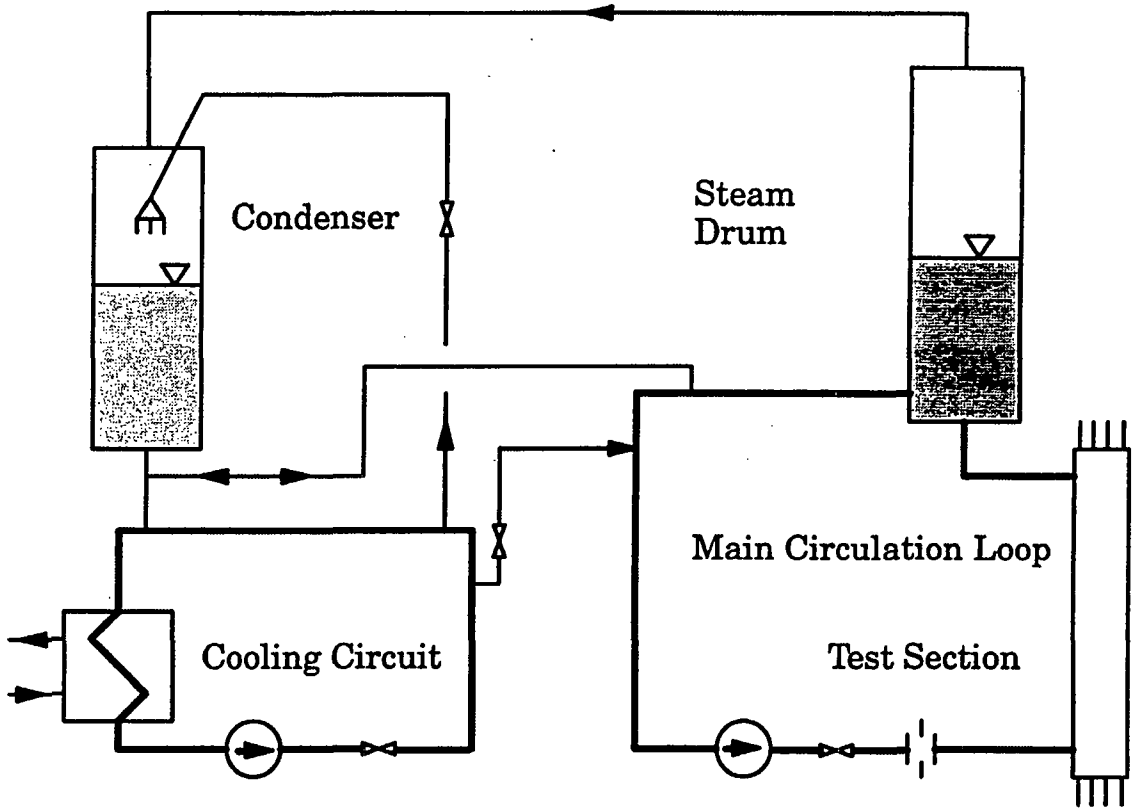

Figure 3-1 FRIGG Loop Diagram

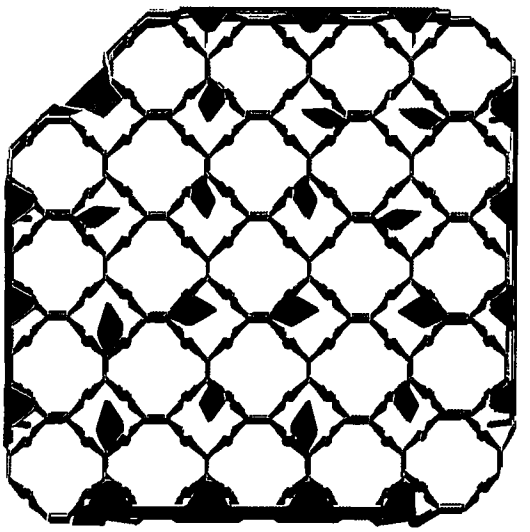

Figure 3-2 SVEA-96 Optima3 Spacer with Mixing Vanes
(named XB in Figure 3-3, the spacers without mixing vanes are named XA in the same figure)

a,c

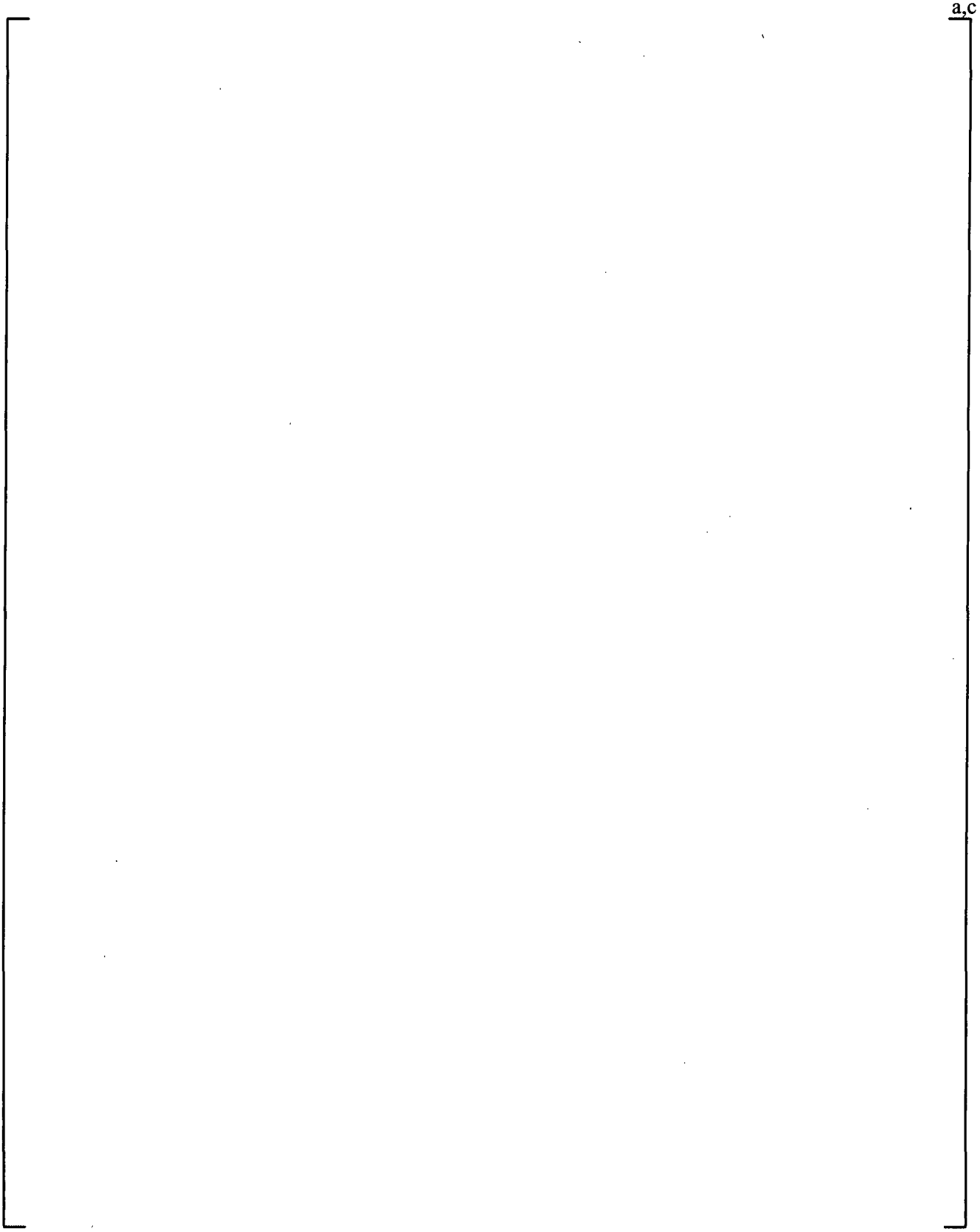

Figure 3-3 Axial Positions of Spacers and Pressure Taps in the Cosine Test

a,c

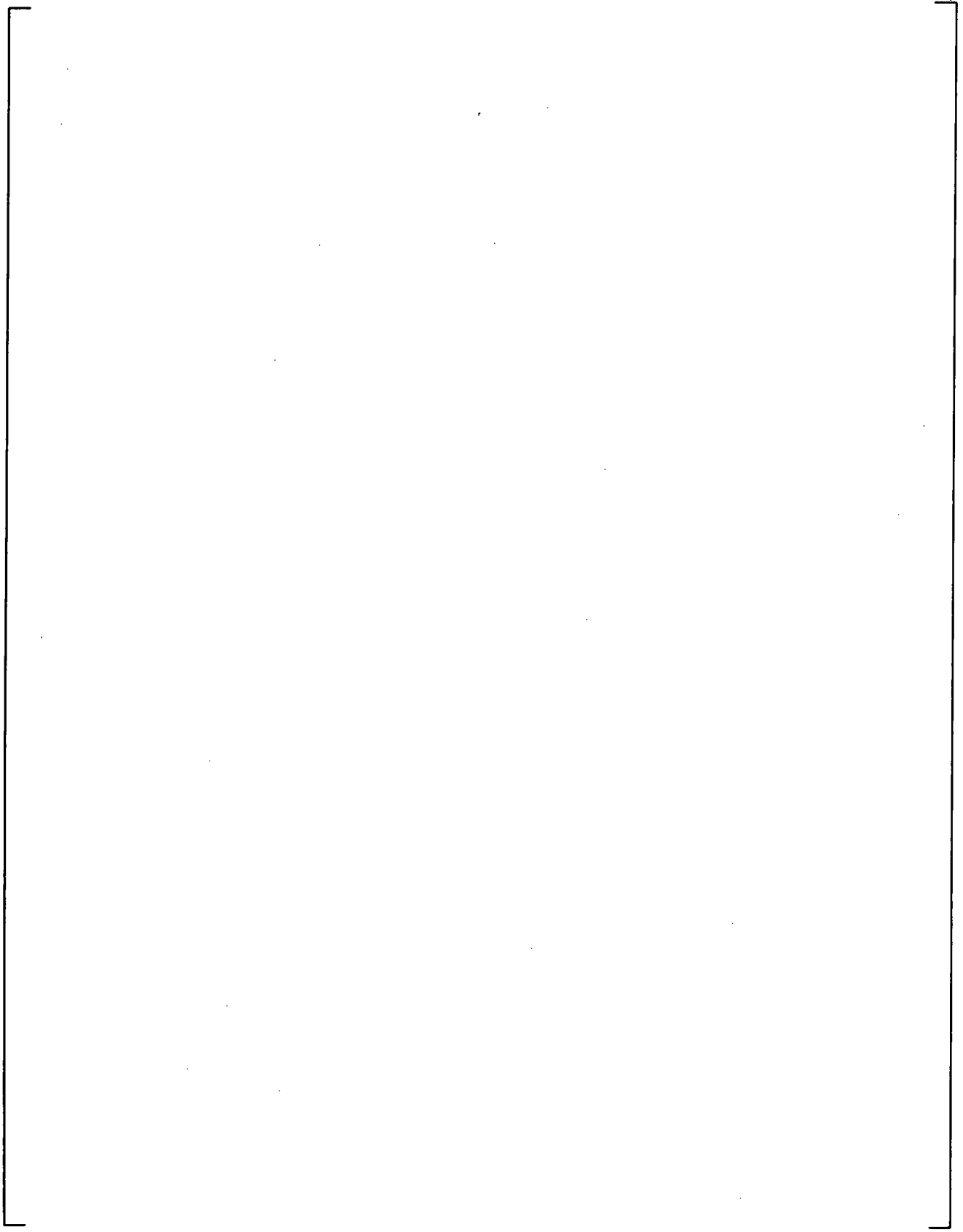

Figure 3-4 Test Sections Data and Numbering of Rods in the FRIGG Loop

a,c

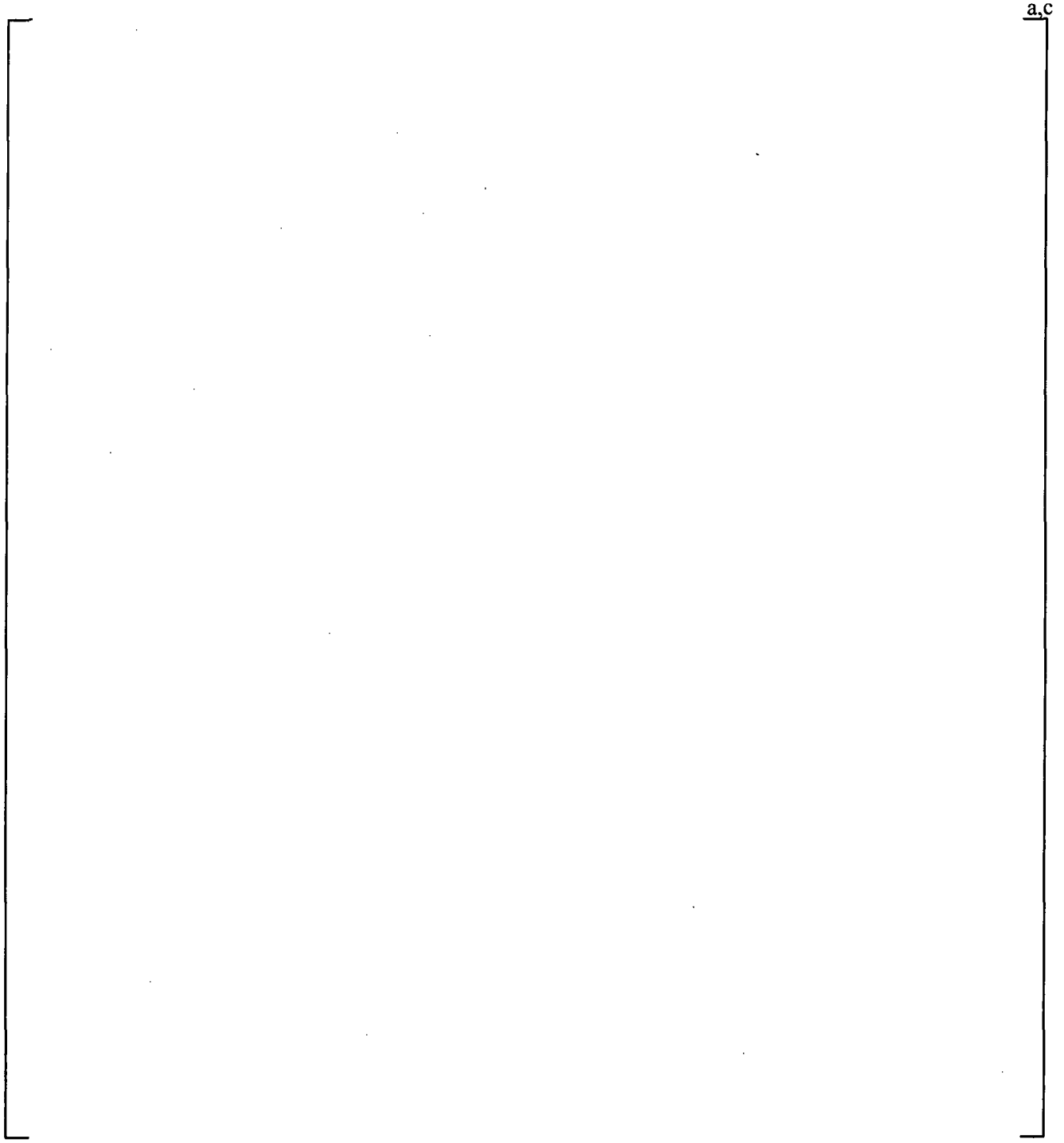

Figure 3-5 Axial Power Shape Used in the FRIGG Test (Cosine Axial Power Shape)

a,c

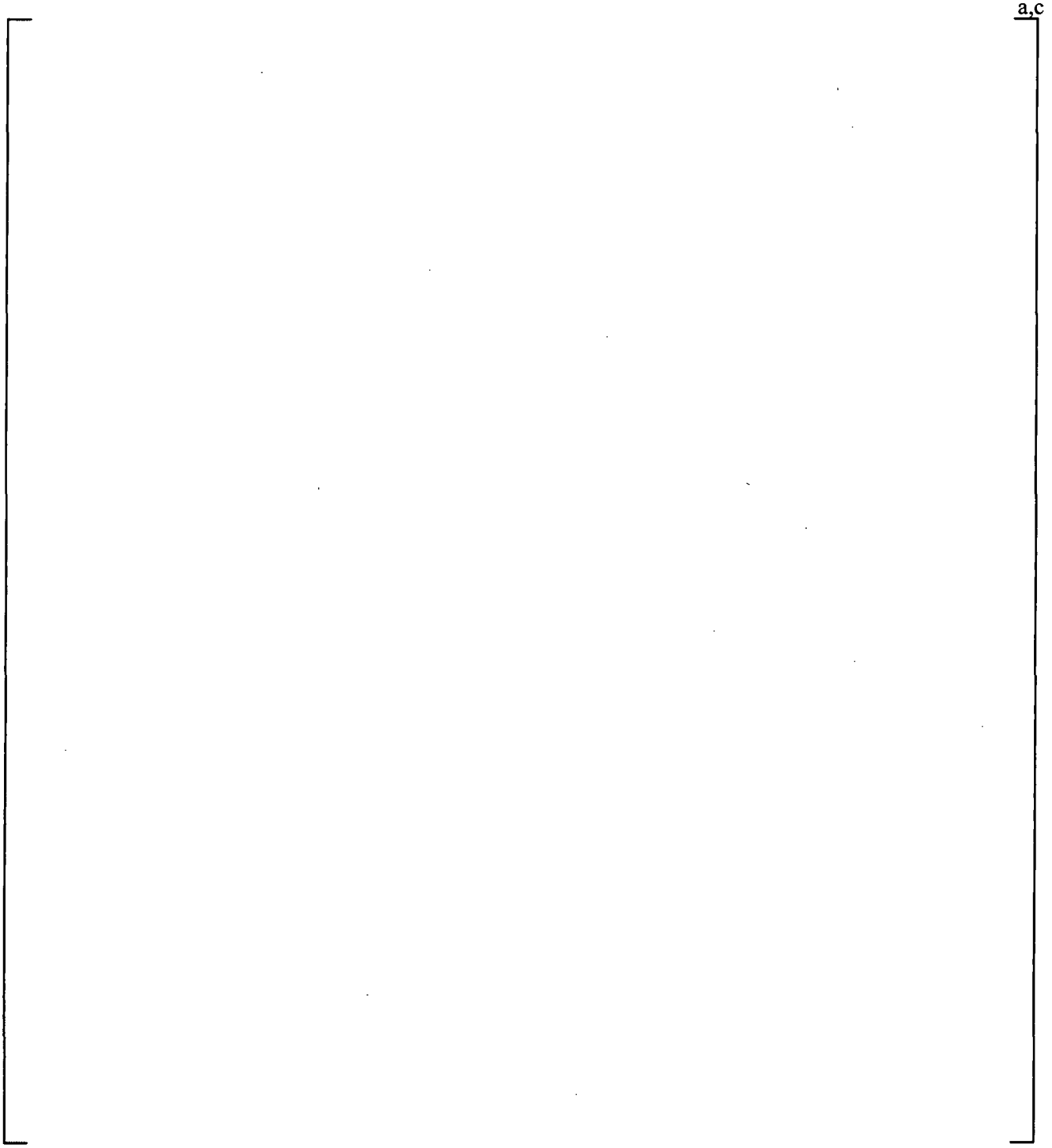

Figure 3-6 Axial Power Shape Used in the FRIGG Test (Bottom-Peaked Axial Power)

a,c

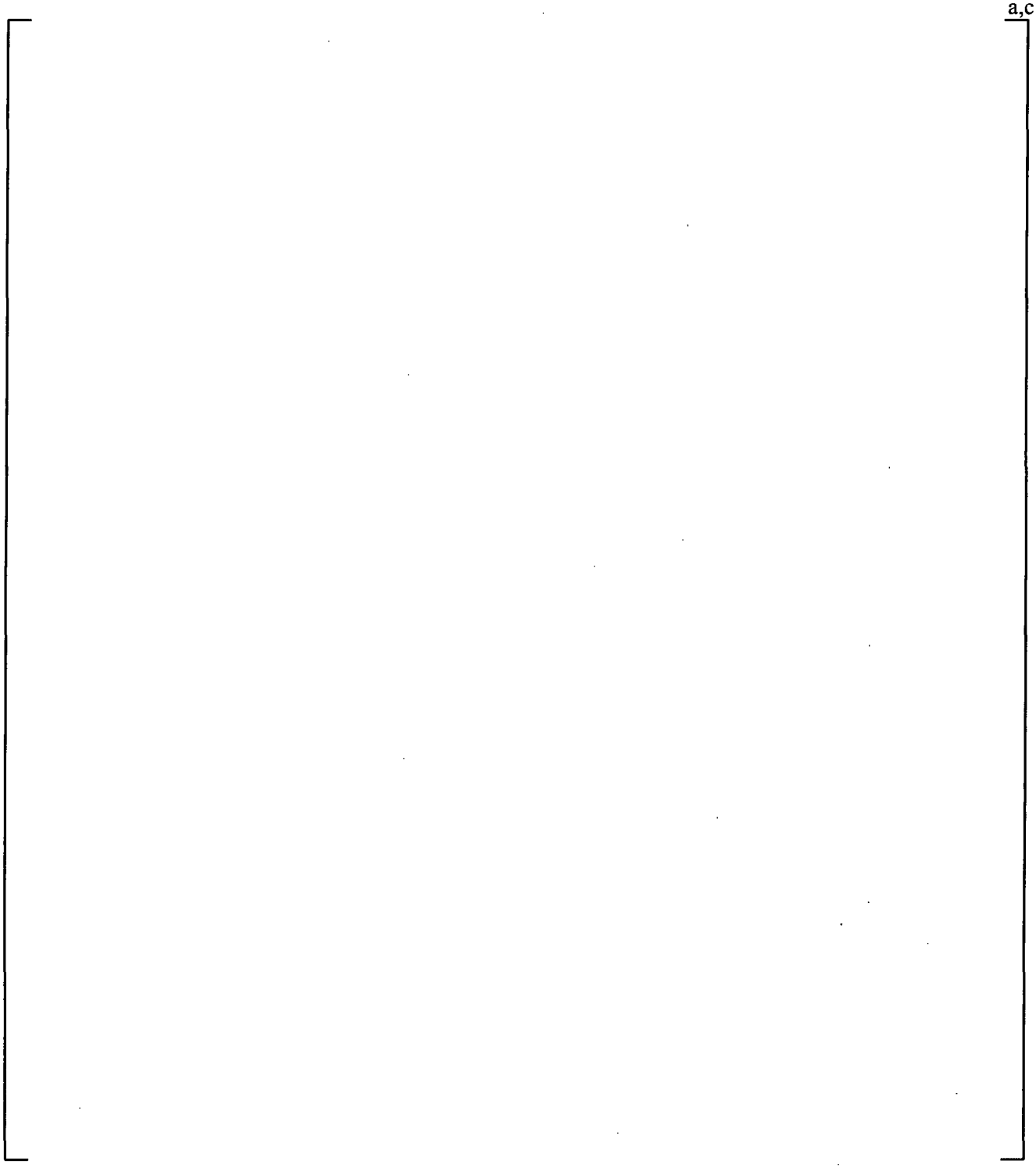

Figure 3-7 Axial Power Shape Used in the FRIGG Test (Top-Peaked Axial Power)

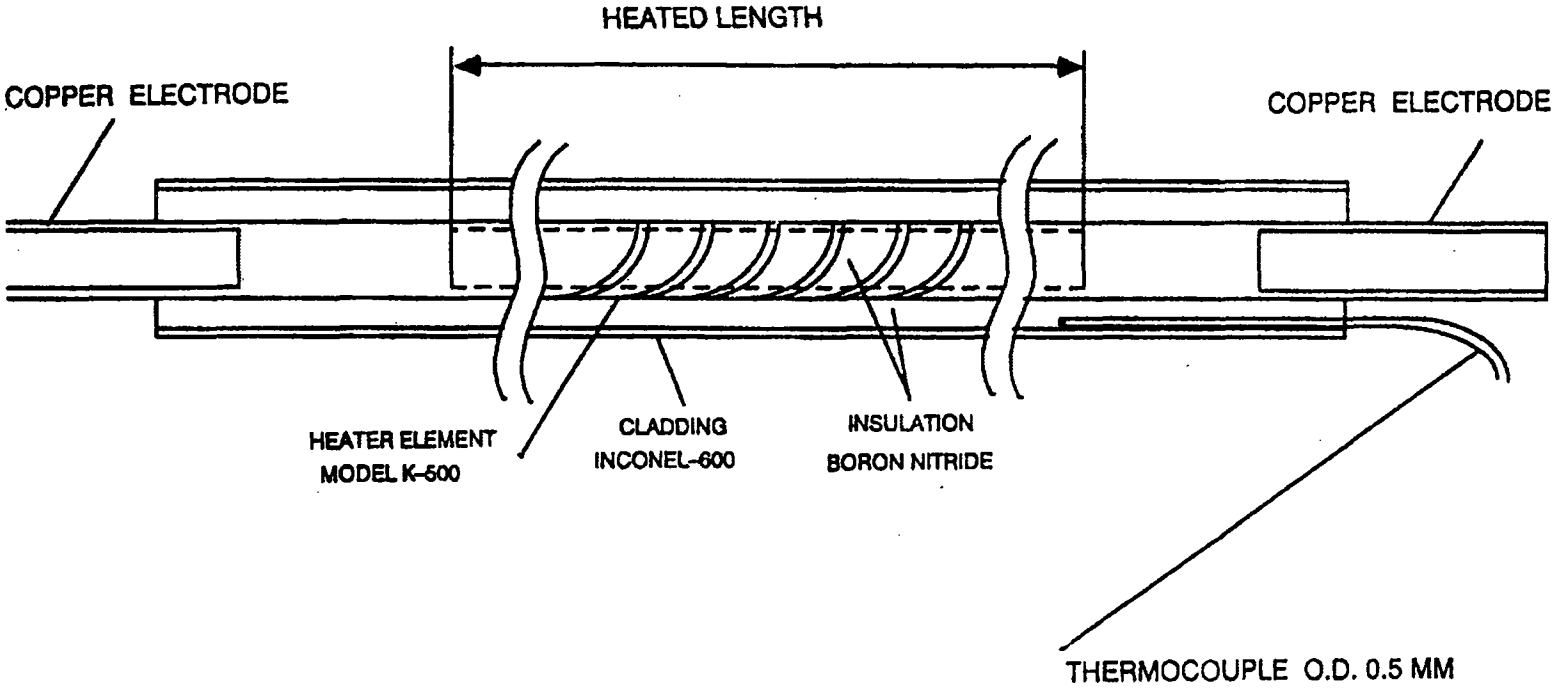

Figure 3-8 Heater Rod Design

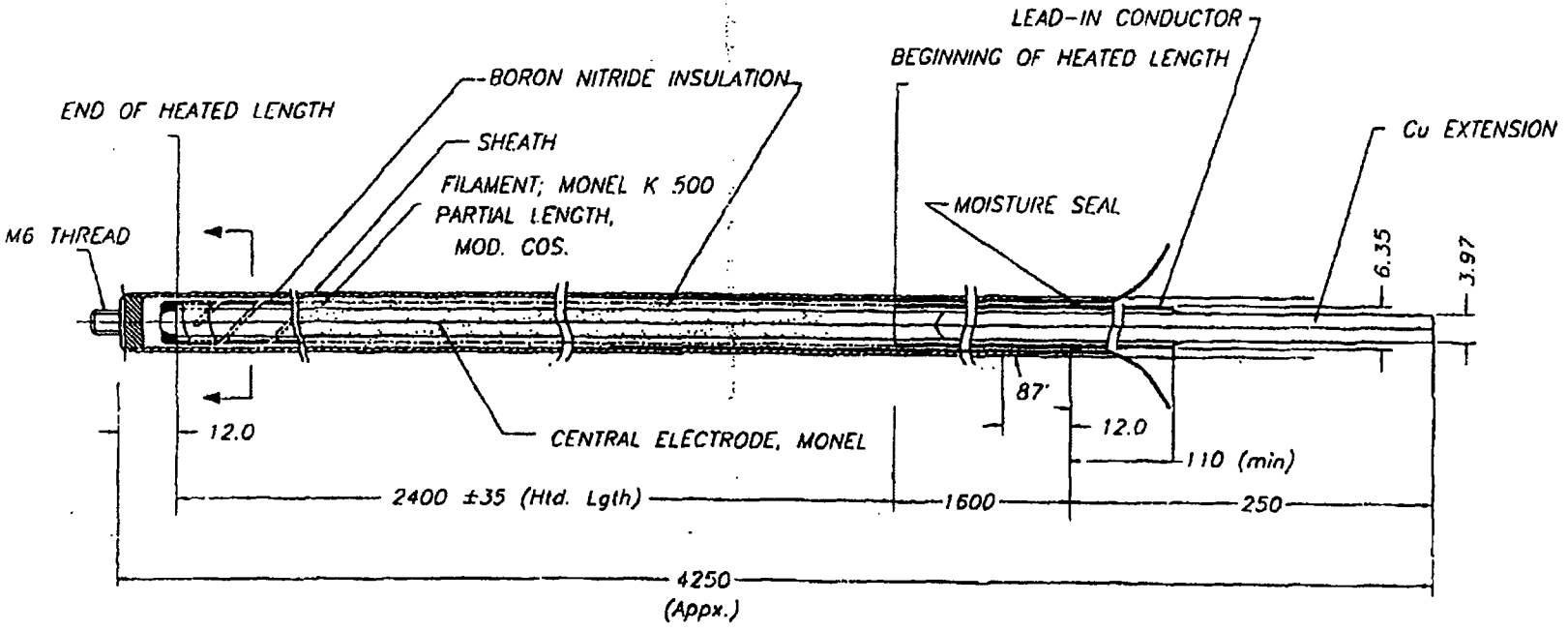

Figure 3-9 Part-Length Heater Rod Design, Chopped Cosine

a,c

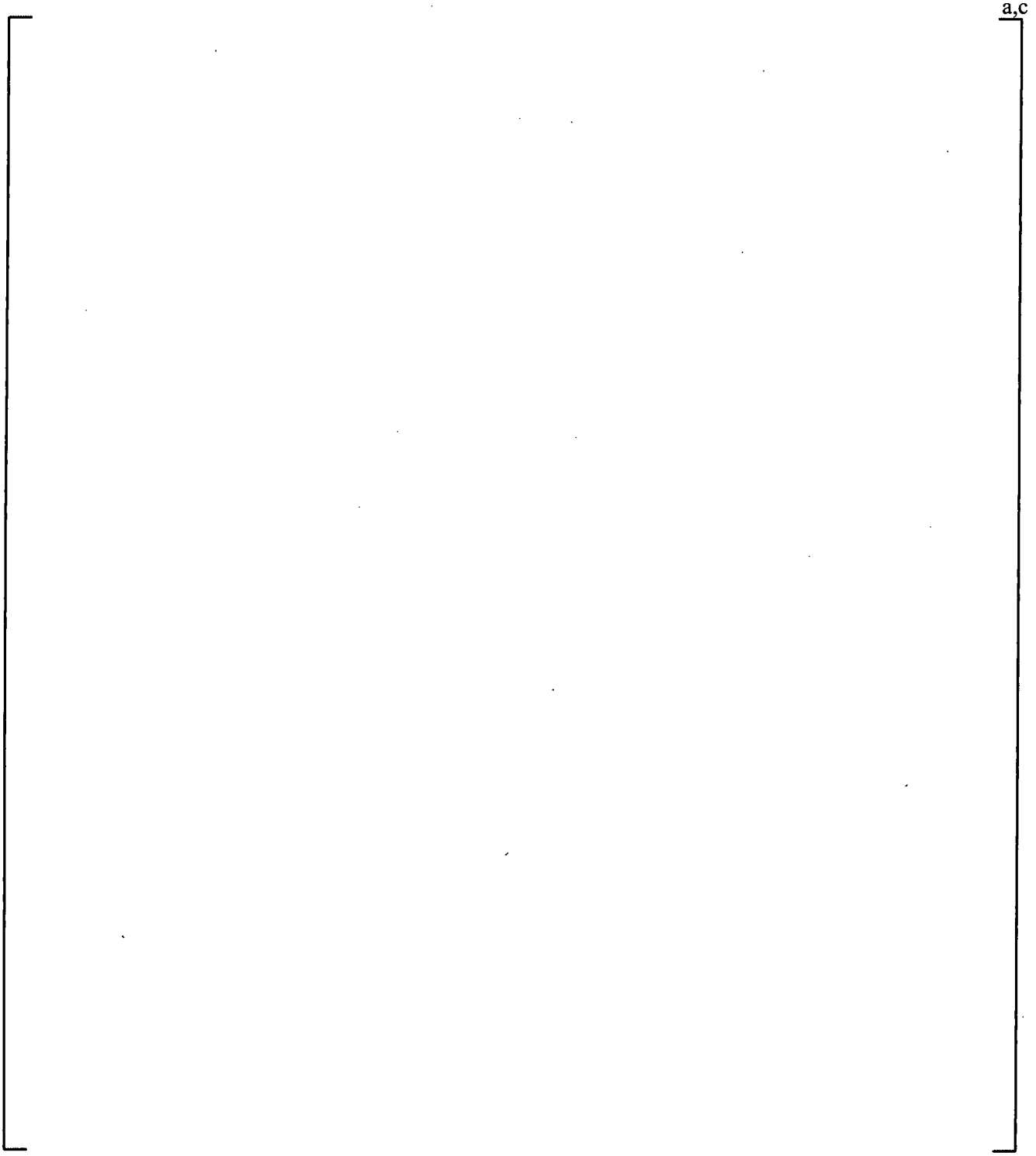

Figure 3-10 Rod Types and Axial Positions of Spacers and Thermocouples, TCs, in the Cosine Test

a,c

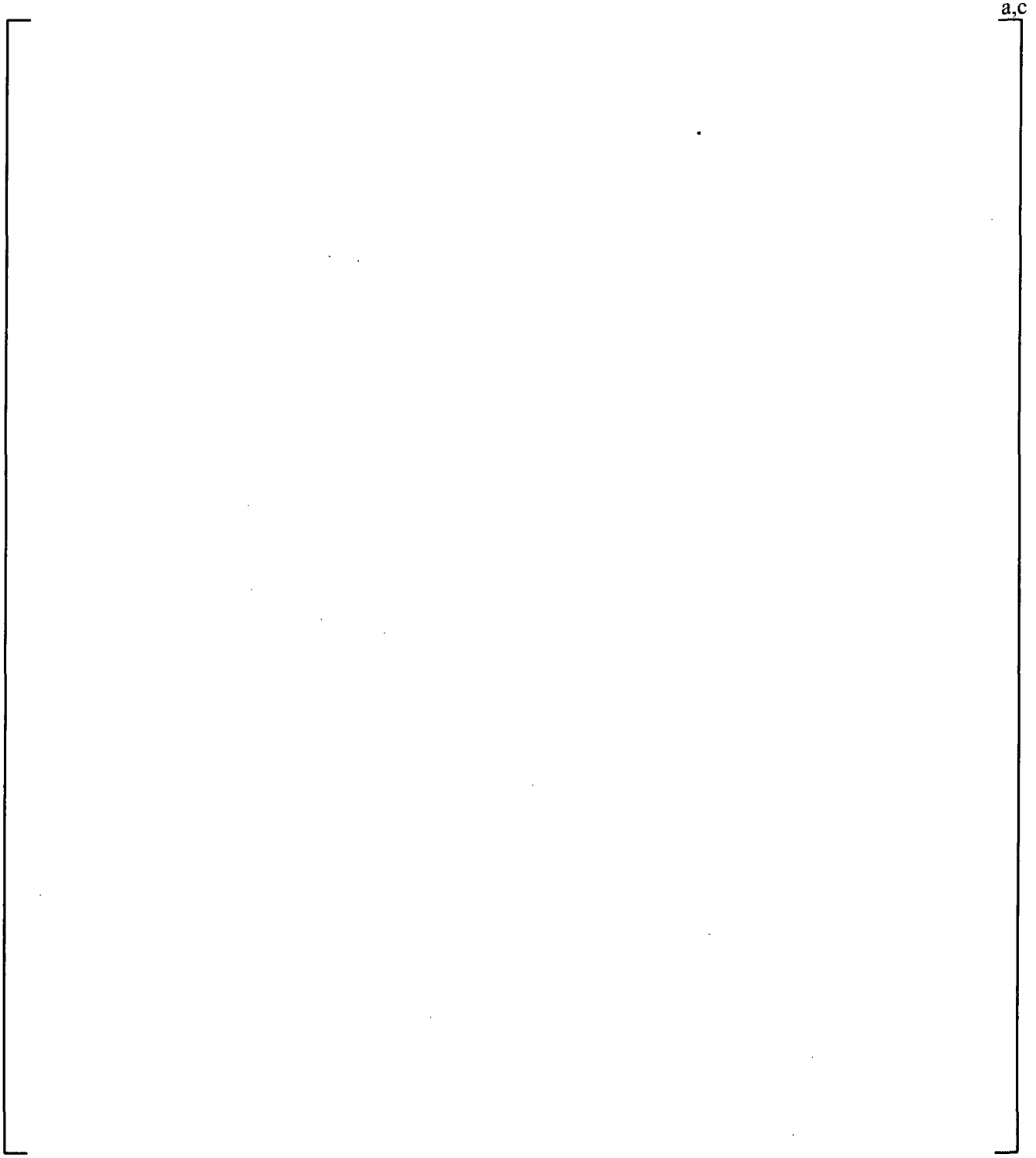

Figure 3-11 Rod Types and Axial Positions of Spacers and Thermocouples in the Bottom Test

a,c

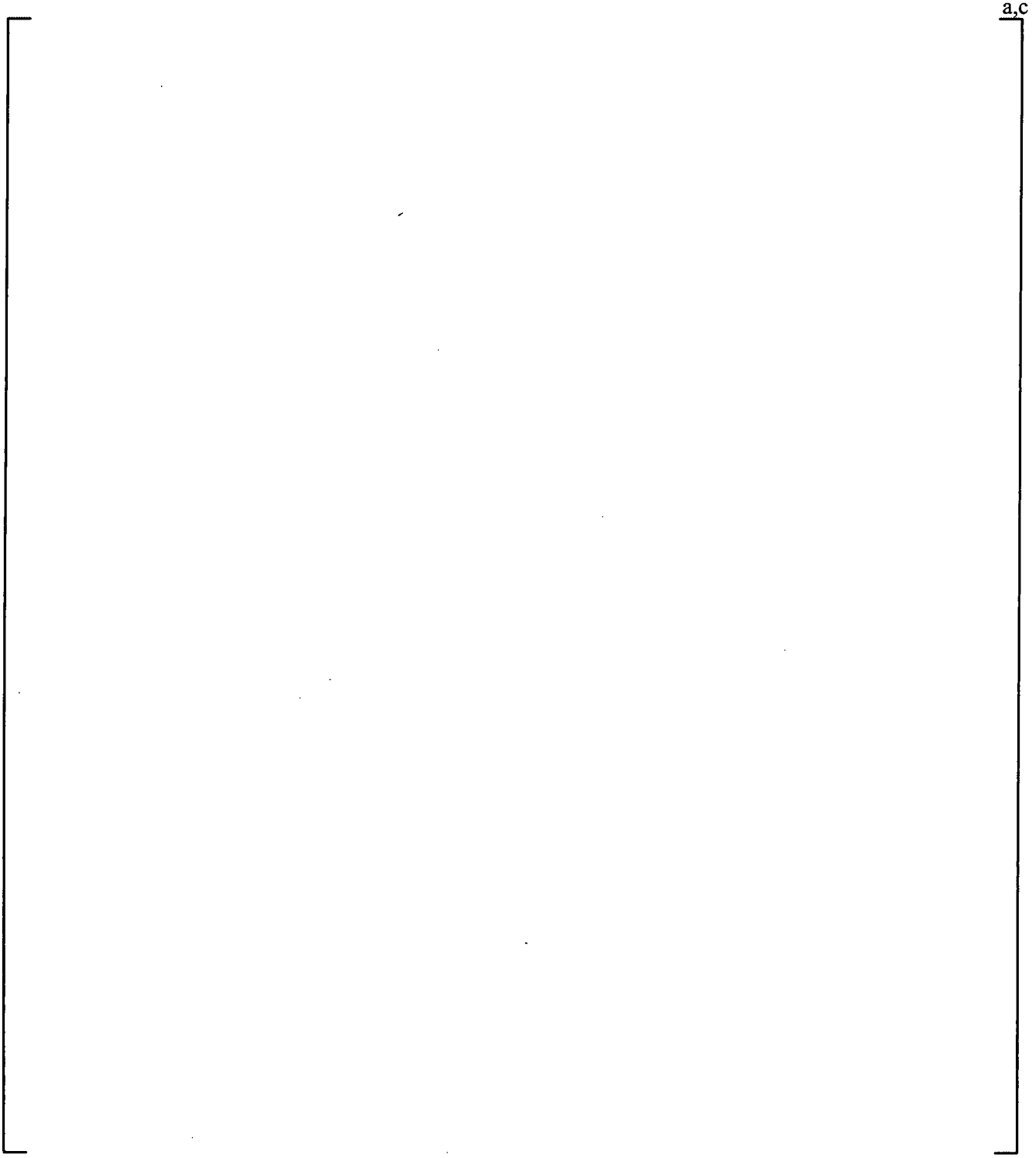

Figure 3-12 Rod Types and Axial Positions of Spacers and Thermocouples in the Top Test

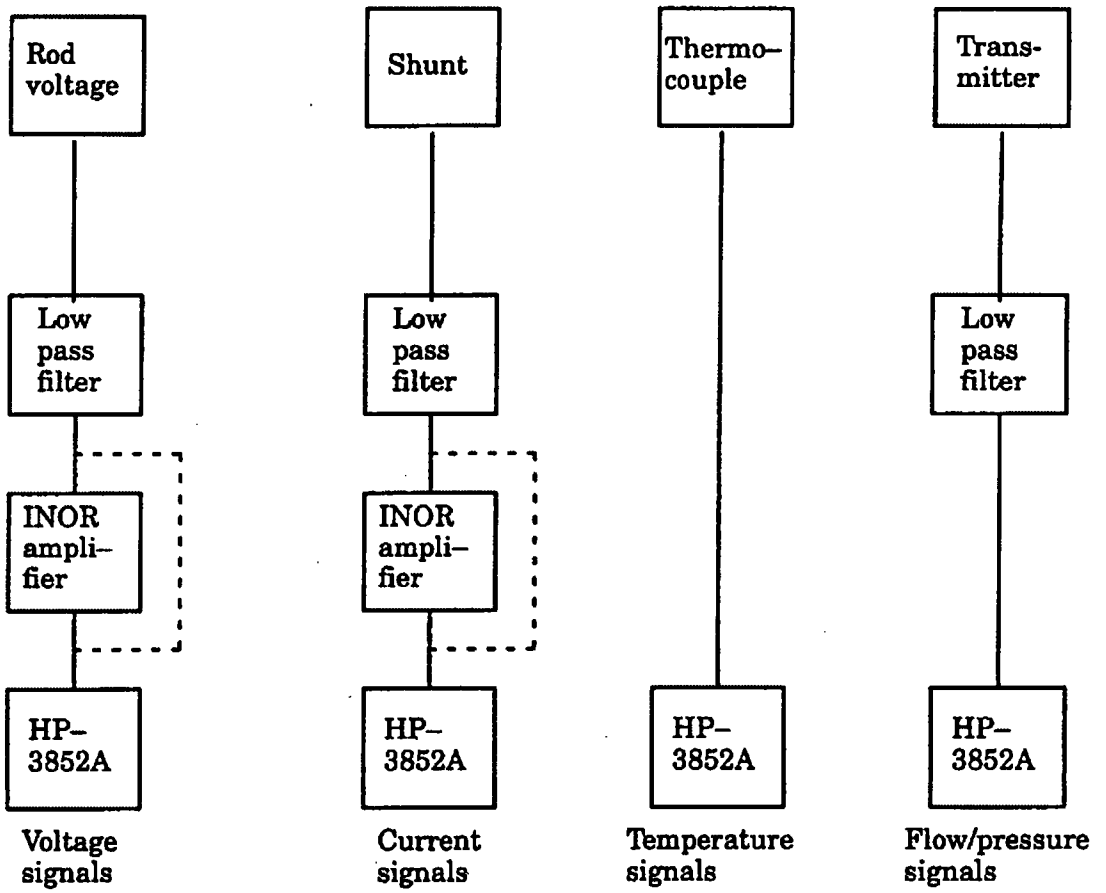

Figure 3-13 Data Acquisition System

4 TEST PROGRAM

As discussed in Section 3, the test program included three separate test series. These series were performed with full-scale SVEA-96 Optima3 24-rod sub-bundle test sections. The three sub-bundle test series differ with respect to the axial power shape provided by the heater rods. Sub-bundle data were obtained for cosine, bottom-peaked, and top-peaked axial power shapes. The test results for the three sub-bundle test series are given in Appendix A (cosine axial power shape), Appendix B (bottom-peaked axial power shape), and Appendix C (top-peaked axial power shape). The test series are identified by the following test identification ranges:

Axial Power Shape	Initial Test Point	Final Test Point	Data Point Table
Cosine	1011-1-RA2(1)	1282-5-VK1	Appendix A
Bottom-Peaked	1013-1-RB2	1382-4-EC14	Appendix B
Top-Peaked	1013-1-RA2	1347-17-EG3	Appendix C

Note:
1. "1011" in the table is the number of the measurement file, "RA2" denotes the radial power distribution and "1" means that it was the first data point with RA2.

The number of data points and local power distributions in the cosine, bottom-peaked, and top-peaked test series are summarized in Table 4-1. Of the collected data points [ ]^{a,c} are not used for correlation development due to unexpected results for one of the rods in the measurements with bottom-peaked axial power shape. This is described in detail in Section 6.3. The actual local power distributions given for the test series in Appendices A, B, and C of this document correspond exactly to just one of the data points in each series. The local power distributions actually measured for each data point, and the R-factor corresponding to that distribution, were used in the correlation derivation and evaluation.

4.1 RANGE OF TEST PARAMETERS

The ranges of test parameters over which the sub-bundle critical power tests were conducted are shown in Table 4-2.

Histograms displaying the ranges of mass flux, pressure, inlet subcooling, and local power distribution as reflected by the CPR correlation R-factor values are shown in Figure 4-1 through Figure 4-4 for all cosine, bottom-peaked, and top-peaked axial power shape tests, respectively. The numbers of data points obtained in each parameter range (mass flux, pressure, inlet subcooling) are shown in Table 4-3 through Table 4-6 for all axial power shape tests: cosine, bottom-peaked, and top-peaked axial power shape tests, respectively.

[

]^{a,c}

[

]a,c

4.2 JUSTIFICATION FOR RANGE OF TEST PARAMETERS

The critical power performance of a test bundle is a function of mass flux, system pressure, inlet subcooling, axial power distribution, and local power distribution. The range of the test parameters for which the critical power tests were conducted is presented in Section 4.1. Justification for the ranges is summarized in the following subsections.

4.2.1 Mass Flux

Critical power is a strong function of mass flux. Therefore, data were obtained at numerous points [ ]a,c over the range of mass flux considered to establish the correlation at various values of pressure, inlet subcooling, and bundle local powers.

The mass flux varied from about [

]a,c. The typical range of mass flux representing normal operations and AOOs is [ ]a,c. The mass flux points used for the tests cover this expected operating range.

4.2.2 System Pressure

Data were obtained at [

]a,c. This range provided sufficient data to determine the system pressure dependence of critical power over the expected range of application of the correlation. [

]a,c

4.2.3 Inlet Subcooling

It is well known (e.g., References 1, 2, 5, and 8) that critical power is a reasonably linear function of the inlet subcooling at constant mass flux and system pressure. [

]a,c

[

]^{a,c} A

10°C inlet subcooling corresponds to the reactor normal operating condition, and 47°C inlet subcooling covers the Loss of Feedwater Heating Anticipated Operational Occurrence.

4.2.4 Axial Power Distribution

Sub-bundle critical power data were obtained for a chopped cosine axial power distribution as well as for bottom-peaked and top-peaked axial power shapes. The cosine axial power shape is reasonably representative of typical operation. The bottom-peaked and top-peaked axial power shapes were selected to capture the effect of axial power shape over the range expected in reactor operation.

4.2.5 Local Power Distribution

The critical power performance of a test bundle is dependent on the test bundle local power distribution. One advantage of the FRIGG test loop is that the test bundle local power distribution can be easily varied. Systematic series of tests were conducted to investigate the critical power performance at various local peaking factors and various peak power rod locations. SVEA-96 Optima3 critical power measurements were obtained [ ]^{a,c} to establish the effect of local power distribution on critical power. Appendices A, B, and C of this document show the nominal local power distributions tested. The local power distribution may differ slightly from point-to-point in tests with the same nominal radial power distribution. The local power distribution actually measured for each data point was used in the correlation development and evaluation.

The local power distributions used in the tests were designed to establish the local power distribution dependence of the bundle critical power performance. The local power distributions involve rods with peaking factors between [

]^{a,c}

4.2.6 Combinations of Parameters

In order to confirm that the parameter ranges considered in the Critical Power tests cover the combinations of conditions expected during typical reactor application, the parameter ranges expected during reactor operation are superimposed on the ranges of test points for combinations of parameters to which Critical Power is considered to be sensitive. As discussed in Section 5, [

]^{a,c}

[

]^{a,c}

4.2.7 Summary

The discussion of the range of individual parameters in subsections 4.2.1 through 4.2.5 can be summarized as follows. The ranges of parameters shown in Figure 4-1 through Figure 4-4 were selected to cover values of parameters impacting Critical Power expected during normal BWR operations as well as AOOs and relevant accidents. In selecting the test matrices, greatest emphasis is placed on those regions in which the reactor will usually operate. Therefore, while [

]^{a,c}

A side by side comparison of the range of the parameters in the tests with that of a typical reactor application is shown in Table 4-7. The combined range is based on the composite range of all the tests. As discussed in subsection 4.2.6 and seen in Table 4-7, the range for a typical application is adequately bounded by the measurement range.

4.3 DATA VALIDATION CRITERIA AND PROCEDURES

Data validation is supported with instrumentation performance reliability checks. All data collection instrumentation is periodically calibrated to assure the accuracy of the data.

The data validation process is further reinforced by assuring that all instrumentation is checked for proper operation prior to the performance of each test. Before and after each shift, a reading from every transmitter is recorded and compared with the expected value for that transmitter. In the event of an abnormal reading, corrective actions are taken before the test is run. In addition, the following checks are performed at the beginning of each test period:

1. A heat balance is calculated to insure that power, flow, and temperature measurements are correct.

2. The overall pressure drops across the bundle at different flow rates are measured.

3. The sum of the power generated by each heater rod is compared with the sum of the power outputs from each power supply unit for all test points. These two bundle power measurements are accepted if they agree to within ±1%.

Critical power reference test points are repeated to assure that the measurements are stable. The reference points for the SVEA-96 Optima3 test series are defined by the following nominal conditions:

[

]a,c

The reproducibility of the critical power was found to be very good for the SVEA-96 Optima3 test series. Examples of the reproducibility are shown in Table 4-8. When the small differences in test parameters are accounted for, the reproducibility of the measured critical powers is excellent.

Conversion of the data to engineering units by the computer allowed preliminary test validation to be done upon completion of a run and before the data analysis took place. This preliminary validation provided immediate feedback on facility operation and data collecting equipment performance.

After the instrumentation had been functionally checked, and the test parameters and performance had been compared with the test matrix, the final data validation was performed during the data reduction and analysis stage.

4.4 SHIFT IN AXIAL POSITION OF SPACERS

The inspection of the bundle after the demounting of the cosine assembly showed that spacers 3, 4, and 5 had shifted downstream about 25 mm while spacers 6 and 7 were shifted slightly upstream. The collected data does not indicate if this shift came before, during, or after the dryout measurements. The following spacer shifts were measured in mm, ("+" for downstream and "–" for upstream):

Spacer number	1	2	3	4	5	6	7	8
Axial shift in mm	+1	+3	+29	+20	+25	-5	-10	+8

The estimated impact this may have on critical power is based on two dryout measurements in FRIGG on the SVEA100B design, with six and seven spacers respectively. This impact is related to the changes in spacer distances upstream from each thermocouple position. Since spacers 3, 4, and 5 shifted by about the same distance, the possible impact on dryout power is an improvement in margin of 1%, at the most, for the axial position under spacer 2, level 23, and a corresponding decreased margin under spacer 5, level 62. The axial position of dryout is very spread out in the measurements using cosine axial power shape, which reduces the impact of a difference in one spacer position. [

]a,c

a,c

[

]

[

]a,c

There was no significant spacer shift in the measurements on top- and bottom-peaked axial power shapes.

4.5 DATA TRENDS

This section shows trends in the measured Critical Power data. These trends are addressed to confirm that the SVEA-96 Optima3 Critical Power database is physically realistic and consistent with similar measurements obtained for other assembly designs. The figures in this section show the measured data points and the corresponding D5 correlation predictions. The D5 CPR correlation is described in Section 5. The correlation predictions of critical power data are denoted with suffix "Pred." Furthermore, it should be noted that some spurious spread is introduced into the data when it is plotted in this manner since all of the points were not obtained at precisely the intended target conditions of the respective figure.

A test bundle is referred to with a designation such as SF24X. The designation SF24XC (S = SVEA, F = FRIGG, 24 = number of rods, X = a serial label, C = cosine shape) stands for dryout power measurements on a SVEA-96 Optima3 sub-bundle test section with the cosine axial power shape. The designation SF24XB refers to dryout power measurements on a SVEA-96 Optima3 sub-bundle test section with the bottom-peaked axial power shape. The designation SF24XT refers to dryout power measurements on a SVEA-96 Optima3 sub-bundle test section with the top-peaked axial power shape.

The results from the cosine-peaked (SF24XC), bottom-peaked (SF24XB), and top-peaked (SF24XT) tests at approximately [ ]a,c are compared with correlation predictions for the uniform and optimized local power distributions, respectively, in Figure 4-9 and Figure 4-10. "Uniform" local power distributions are intended to provide the same power to each of the 21 full-length heater rods. The term "optimized" refers to a rod power distribution that gives the highest dryout power for a given set of mass flux, system pressure, inlet subcooling, and axial power shape conditions. The optimized [

]a,c

The critical power decreases as the axial power shapes become more top-peaked in Figure 4-9 through Figure 4-10. This tendency is in agreement with measurements obtained for other assembly designs such as the SVEA-96, SVEA-96+, and SVEA-96 Optima2 design discussed in References 1, 2, and 8. The monotonic increase in Critical Power as a function of mass flux is also consistent with other designs and the data obtained in other facilities. Therefore, the trends in these data reflect the expected dependence on assembly flow and axial power shape based on previous testing of earlier designs and the physical nature of the dryout process for various local power distributions.

Trends in exit pressure and inlet subcooling for various local power distributions are shown for the cosine-peaked axial power distribution (test bundle SF24XC), bottom-peaked axial power distribution

(test bundle SF24XB) and the top-peaked axial power distribution (test bundle SF24XT) in Figure 4-11 through Figure 4-16, Figure 4-17 through Figure 4-22, and Figure 4-23 through Figure 4-28, respectively.

The influence of inlet subcooling at an exit pressure of approximately [

]^{a,c}

Critical power as a function of pressure for various constant mass flows and inlet subcooling are shown in Figure 4-13 to Figure 4-16 for the cosine-peaked axial power shape, in Figure 4-19 to Figure 4-22 for the bottom-peaked axial power shape and Figure 4-25 to Figure 4-28 for the top-peaked axial power shape. As shown in these figures, [

]^{a,c} The same type of behavior as a function of system pressure was observed for the SVEA-96, SVEA-96+, and SVEA-96 Optima2 design reported in References 1, 2, and 8 and is also consistent with other earlier designs.

The purpose of providing data trend plots in Figure 4-11 through Figure 4-28 is to show that the trends in the data are physically reasonable and consistent with expectations. D5 predictions are included in these figures to help the correlation review as previously requested in the review of the ABBD1.0, ABBD2.0, and D4.1 Correlations (References 1, 2, and 8). Note that non-smooth variations can sometimes be observed in both measured and predicted data trends when the parameters supposed to be constants varied slightly due to experimental constraints. This is a consequence of the difficulties to predefine operating conditions, not of measurement uncertainty. However, these variations do not perturb the overall trend.

The axial position of dryout as a function of mass flux, pressure, and subcooling is plotted in Figure 4-29 through Figure 4-31. The trend that the axial position of dryout moves upstream as a function of flow has been seen for earlier designs, but it can be noted that at normal operating conditions, with bottom-peaked or cosine axial power shape, the probability of dryout is very spread out axially from the end of heated length and down to a level of 1.9 meters. This indicates that the spacer distances, that are shorter in the upper half of the bundle and longer in the bottom half, are well optimized.

Table 4-1 Number of Points in SVEA-96 Optima3 Test Series

Test Series – Characterized by Axial Power Shape	Total Number of Points	Number of Points used in D5 Development	Number of Local Power Distributions	Number of Local Power Distributions used in D5 Development

a,b,c

Table 4-2 Range of Test Parameters

Test Parameter	Measured Range	Range Used in D5 Correlation Development

a,b,c

Table 4-3 Number of Data Points in Various Parameter Ranges (All Three Axial Power Shapes)

Mass flux [kg/m^2/s]			Pressure [bar]			Subcooling [K]		
Lower bound	Upper bound	# of data points	Lower bound	Upper bound	# of data points	Lower bound	Upper bound	# of data points

a,b,c

Note: Range is defined as Lower Bound < parameter value ≤ Upper Bound.

Table 4-4 Number of Data Points in Various Parameter Ranges (Cosine Axial Power Shapes)

Mass flux [kg/m^2/s]			Pressure [bar]			Subcooling [K]		
Lower bound	Upper bound	# of data points	Lower bound	Upper bound	# of data points	Lower bound	Upper bound	# of data points

a,b,c

Note: Range is defined as Lower Bound < parameter value ≤ Upper Bound.

Table 4-5 Number of Data Points in Various Parameter Ranges (Bottom-Peaked Axial Power Shapes)

Mass flux [kg/m^2/s]			Pressure [bar]			Subcooling [K]		
Lower bound	Upper bound	# of data points	Lower bound	Upper bound	# of data points	Lower bound	Upper bound	# of data points

a,b,c

Note: Range is defined as Lower Bound < parameter value ≤ Upper Bound.

Table 4-6 Number of Data Points in Various Parameter Ranges (Top-Peaked Axial Power Shapes)

Mass flux [kg/m^2/s]			Pressure [bar]			Subcooling [K]		
Lower bound	Upper bound	# of data points	Lower bound	Upper bound	# of data points	Lower bound	Upper bound	# of data points

a,b,c

Note: Range is defined as Lower Bound < parameter value ≤ Upper Bound.

Table 4-7 Range of Parameters

	Mass Flux [kg/m^2/s]	**Outlet Pressure [bar]**	**Subcooling [K]**	**Relative Rod Power (sub-bundle)**

a,b,c

Table 4-8 Examples of Test Reproducibility

Test ID	Pressure [bar]	Subcooled Temperature [K]	Flow [kg/s]	Mass Flux [kg/m2/s]	Dryout Power [kW]
Cosine Axial Power Shape					

a,b,c

a,b,c

Figure 4-1 Histogram for all SVEA-96 Optima3 Tests, Frequency versus Mass Flux (Top-, Cosine, and Bottom-peaked Axial Power Profile)

a,b,c

Figure 4-2 Histogram from all SVEA-96 Optima3 Tests, Frequency versus Pressure (Top-, Cosine, and Bottom-peaked Axial Power Profile)

a,b,c

Figure 4-3 Histogram from all SVEA-96 Optima3 Tests, Frequency versus Subcooling (Top-, Cosine, and Bottom-peaked Axial Power Profile)

a,b,c

Figure 4-4 Histogram from all SVEA-96 Optima3 Tests, Frequency versus R-factor (Top-, Cosine, and Bottom-peaked Axial Power Profile)

a,b,c

Figure 4-5 Range of Test Parameters (Pressure vs. Mass Flux) Compared with Typical Application Range

a,b,c

Figure 4-6 Range of Test Parameters (Pressure vs. Subcooling) Compared with Typical Application Range

a,b,c

Figure 4-7 Range of Test Parameters (Subcooling vs. Mass Flux) Compared with Typical Application Range

a,b,c

Figure 4-8 Range of Test Parameters (R-factor vs. Mass Flux) Compared with Typical Application Range

a,b,c

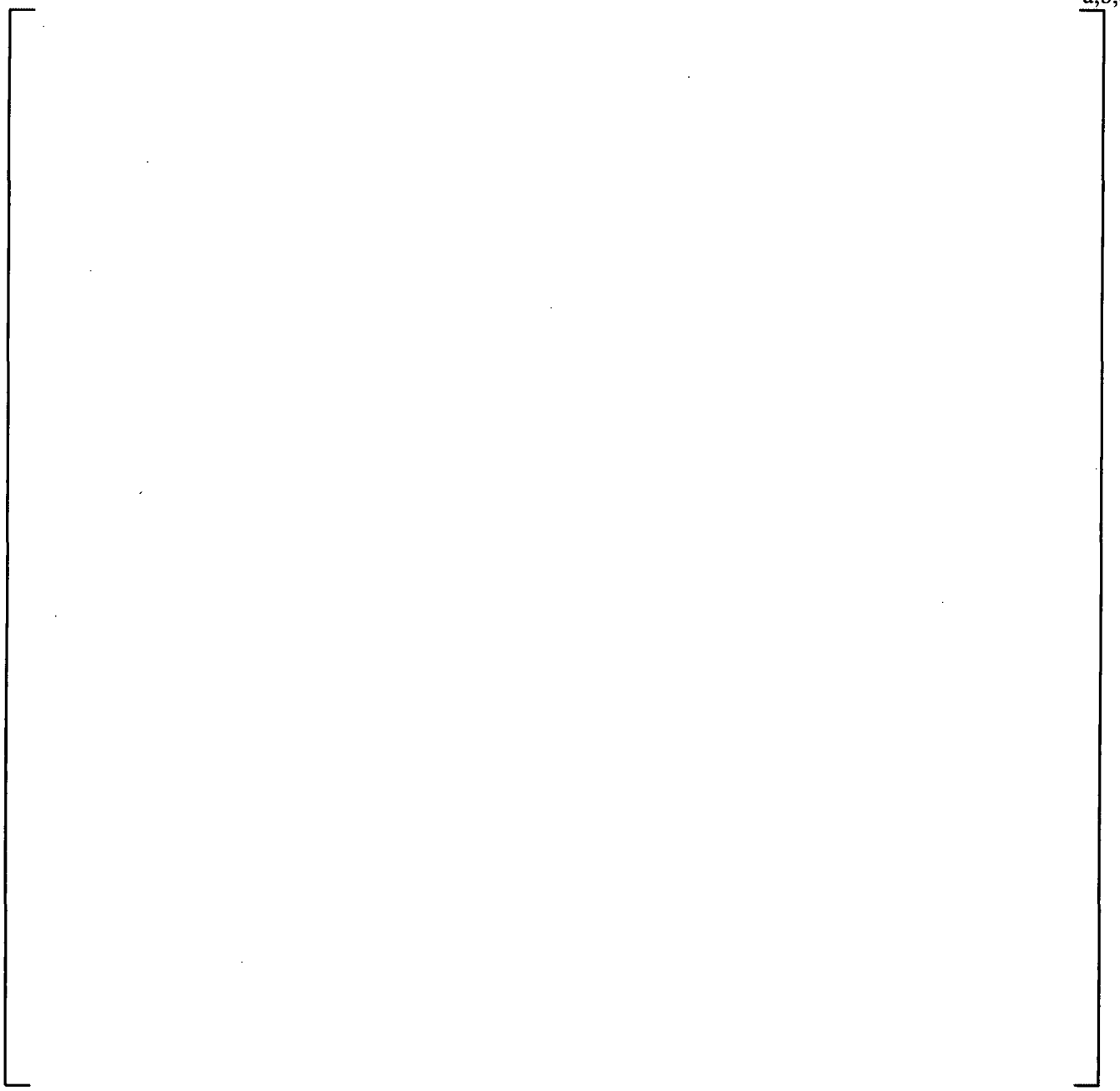

Figure 4-9 Critical Power versus Flow at 69 Bar, 10 K Subcooling, for Uniform Local Power Distribution

a,b,c

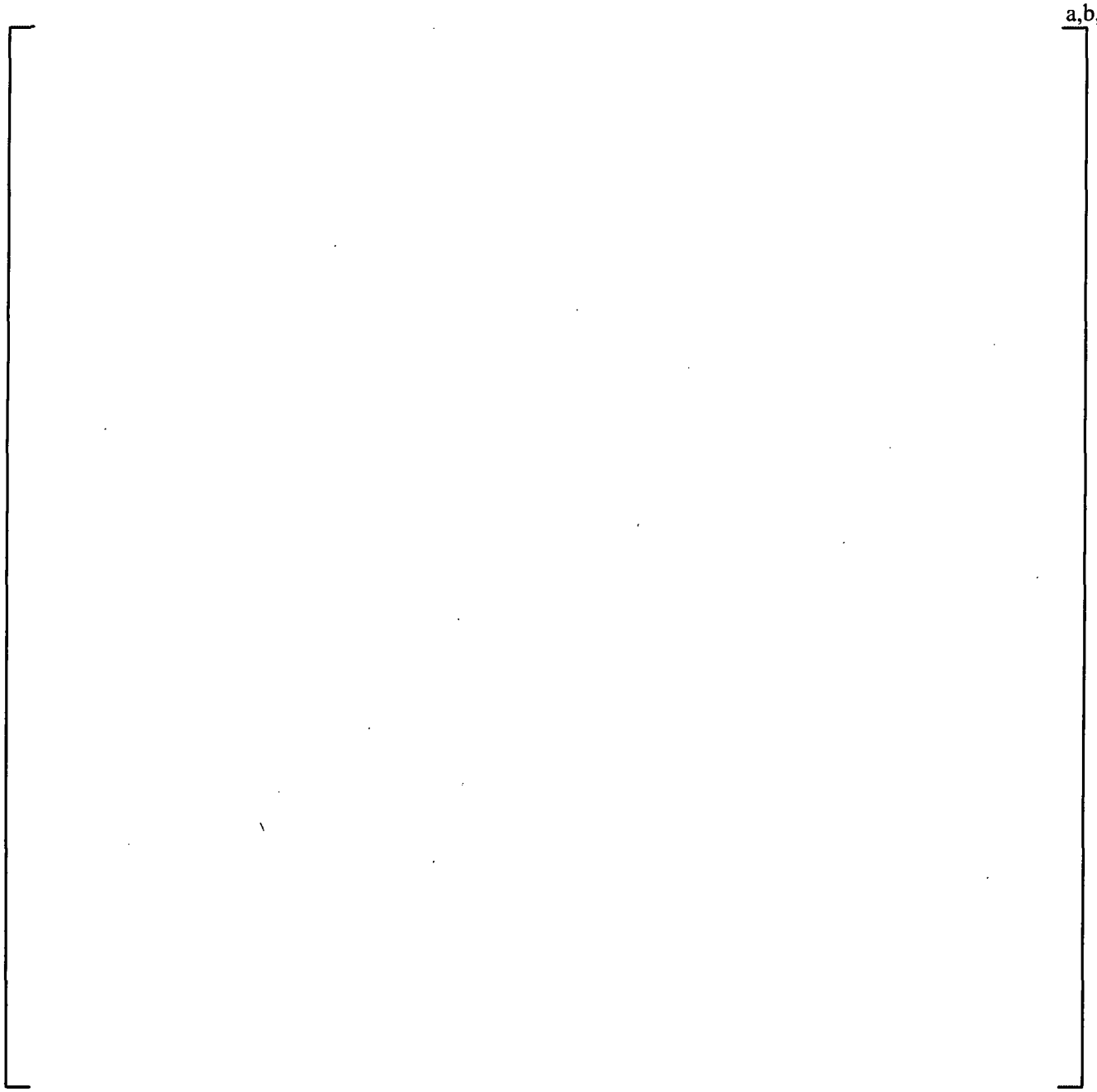

Figure 4-10 Critical Power versus Flow at 69 Bar, 10 K Subcooling, for Optimized Local Power Distribution

a,b,c

Figure 4-11 SF24XC Critical Power versus Subcooling at 69 Bar, Uniform Local Power Distribution, for Various Flows

a,b,c

Figure 4-12 SF24XC Critical Power versus Subcooling at 69 Bar, Optimized Local Power Distribution, for Various Flows

a,b,c

Figure 4-13 SF24XC Critical Power versus Pressure at 10 K Subcooling, Uniform Local Power Distribution, for Various Flows

a,b,c

Figure 4-14 SF24XC Critical Power versus Pressure at 40 K Subcooling, Uniform Local Power Distribution, for Various Flows

a,b,c

Figure 4-15 SF24XC Critical Power versus Pressure at 10 K Subcooling, Optimized Local Power Distribution, for Various Flows

a,b,c

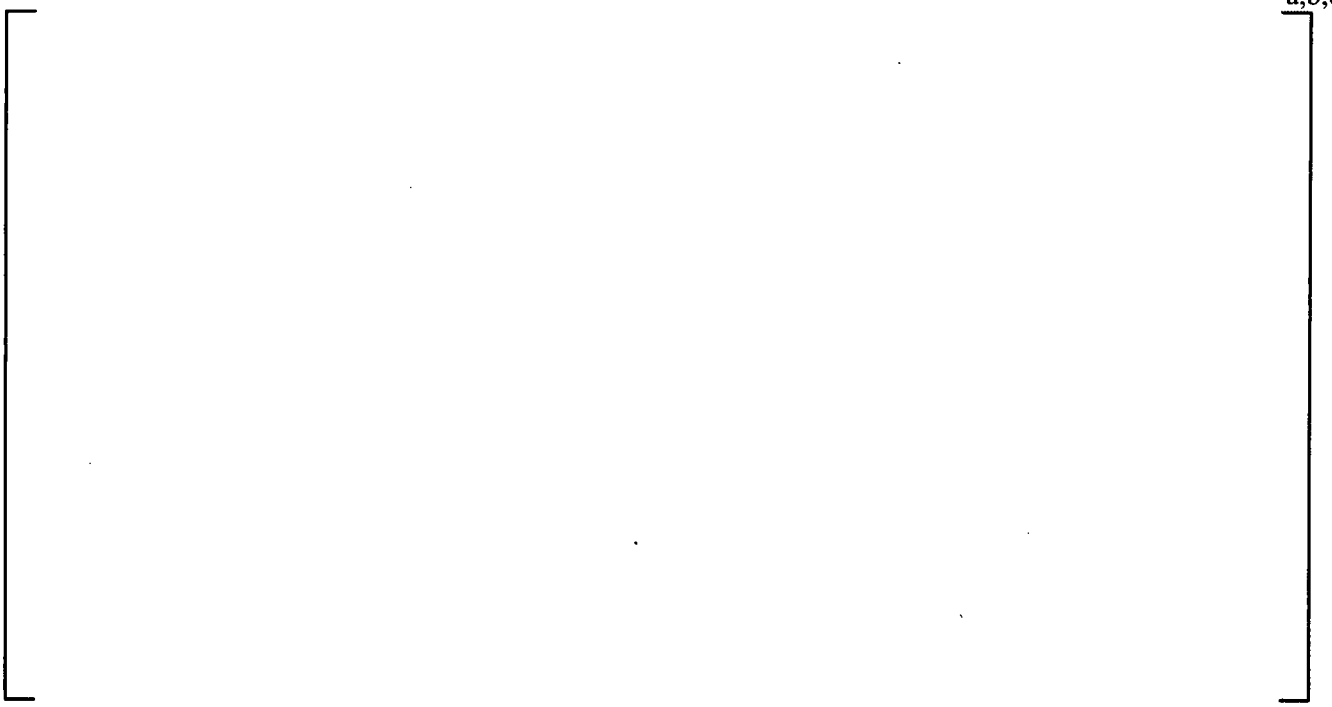

Figure 4-16 SF24XC Critical Power versus Pressure at 40 K Subcooling, Optimized Local Power Distribution, for Various Flows

a,b,c

Figure 4-17 SF24XB Critical Power versus Subcooling at 69 Bar, Uniform Local Power Distribution, for Various Flows

a,b,c

Figure 4-18 SF24XB Critical Power versus Subcooling at 69 Bar, Optimized Local Power Distribution, for Various Flows

a,b,c

Figure 4-19 SF24XB Critical Power versus Pressure at 10 K Subcooling, Uniform Local Power Distribution, for Various Flows

a,b,c

Figure 4-20 SF24XB Critical Power versus Pressure at 40 K Subcooling, Uniform Local Power Distribution, for Various Flows

a,b,c

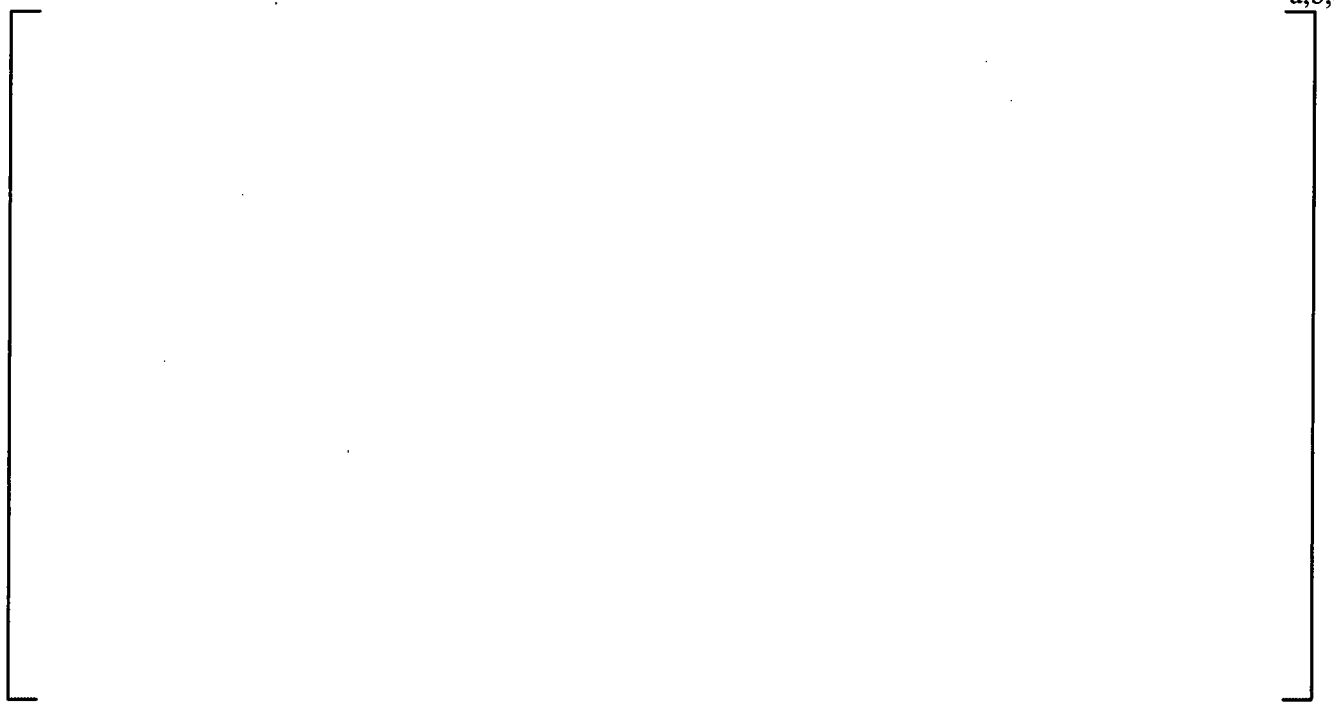

Figure 4-21 SF24XB Critical Power versus Pressure at 10 K Subcooling, Optimized Local Power Distribution, for Various Flows

a,b,c

Figure 4-22 SF24XB Critical Power versus Pressure at 40 K Subcooling, Optimized Local Power Distribution, for Various Flows

a,b,c

Figure 4-23 SF24XT Critical Power versus Subcooling at 69 Bar, Uniform Local Power Distribution, for Various Flows

a,b,c

Figure 4-24 SF24XT Critical Power versus Subcooling at 69 Bar, Optimized Local Power Distribution, for Various Flows

a,b,c

Figure 4-25 SF24XT Critical Power versus Pressure at 10 K Subcooling, Uniform Local Power Distribution, for Various Flows

a,b,c

Figure 4-26 SF24XT Critical Power versus Pressure at 40 K Subcooling, Uniform Local Power Distribution, for Various Flows

a,b,c

Figure 4-27 SF24XT Critical Power versus Pressure at 10 K Subcooling, Optimized Local Power Distribution, for Various Flows

a,b,c

Figure 4-28 SF24XT Critical Power versus Pressure at 40 K Subcooling, Optimized Local Power Distribution, for Various Flows

a,b,c

Figure 4-29 Axial Position of Dryout versus Mass Flux for Three Axial Power Shapes, All Data

a,b,c

Figure 4-30 Axial Position of Dryout versus Pressure for Three Axial Power Shapes at Mass Flux in the Range 800-1800 kg/m^2/s

a,b,c

Figure 4-31 Axial Position of Dryout versus Sub-cooling for Three Axial Power Shapes in the Mass Flux Range 800-1800 kg/m^2/s and at an Outlet Pressure of 70 Bar

5 D5 CPR CORRELATION

The D5 CPR correlation for SVEA-96 Optima3 is a sub-bundle correlation in the sense that it is based on 24-rod sub-bundle data. The mathematical expression of the D5 correlation and its application for calculating CPR at the fuel rod, sub-bundle, and full-bundle levels under steady-state and transient conditions are described in this section. A comprehensive description of the D5 CPR correlation and its use in a wide range of applications is available as a peer-reviewed conference paper, Reference 6.

[

]^{a,c}

Following physical and experimental considerations, [

]^{a,c}. The steady-state D5 correlation describes a best-fit relation, considering the test data, between [

]^{a,c} The detailed correlation expression is given in Section 5.3 and the R-factor model is described in Section 5.6.

A least squares method was used to optimize the correlation and R-factor coefficients (see Sections 5.3 and 5.6) by systematically minimizing the difference between the predicted and measured dryout power [

]^{a,c} studied in the FRIGG database.

[

]^{a,c}

All parameters discussed below are in SI units unless otherwise stated.

5.1 SELECTED CORRELATION FORM

Theoretical considerations of the dryout phenomenon were used to derive the relevant parameters in the determination of the dryout power under various conditions, in particular [

]^{a,c}. In this section, a correlation form is derived via analysis of empirical data trends and physical considerations using the SVEA-96 Optima3 FRIGG database presented in Section 4.

The experimentally determined critical steam quality was found to decrease in a non-linear manner with mass flux. Physical consideration also lead to the conclusion that the critical quality should be asymptotic with increasing mass flux, and should approach a finite value (100% or less) for mass flux approaching zero. A mathematical relationship that exhibits the desired behavior is the so-called Goempetz curve generally defined by three parameters as follows:

$$X_c = \alpha e^{\beta e^{\gamma G}}$$

The experimental critical quality was found to decrease with R-factor within the FRIGG database for constant mass flux. The following form was selected: [ ]^{a,c}

The effect of pressure was considered [ ]^{a,c}. It is also known from physical consideration that the critical quality as function of pressure would approach zero at zero pressure and critical pressure. In general, such a behavior will be exhibited by a product of at least two quantities (Z and W) that represent steam properties exhibiting opposite trends with respect to pressure raised to certain powers (ϕ and φ):

$$X_c = Z(p)^{\phi} \cdot W(p)^{\varphi}$$

A number of such products were explored, and a product of the vapor density normalized to vapor density at 70 bars, ρ_{v70}, plus a constant and latent heat, h_{fg}, raised to a power was determined to yield the best correlation results. Use of the vapor density is also supported by the fact that, according to literature, it directly affects deposition rate.

The final form of the D5 critical quality is given in Section 5.3.

5.2 EXTRAPOLATION OF FLOW RANGE

Westinghouse has found that under certain circumstances it may be necessary to evaluate Critical Power values outside of the mass flux range covered by the experimental results in FRIGG. For example, in some plant applications, critical power evaluation may be needed at very low core flows for which assemblies on the core periphery could have the potential for experiencing mass flux values less than [ ]^{a,c} kg/m^2/s. Application of the correlation to very low flows is also necessary during certain transients. Therefore, it may be necessary to conservatively estimate SVEA-96 Optima3 Critical Power values for mass fluxes outside of the range used in the development of the correlation. The critical power estimates outside of the correlation range from [ ]^{a,c} kg/m^2/s must be established conservatively since measurement data for SVEA-96 Optima3 are not available outside of this range.

Critical power tests demonstrate that critical quality increases with decreasing mass flux. Therefore, conservative Critical Powers are predicted at all mass fluxes between [ ]^{a,c}. A constant critical quality corresponds to a critical power decreasing linearly as a function of mass flux.

For all SVEA fuel designs, critical power has been found to be [

]^{a,c}. Accordingly, should it be necessary to evaluate CPR for mass flux values greater than [

]^{a,c} as input. This approach assures that CPR is not overestimated for mass flux values above [ ]^{a,c} kg/m^2/s.

The manner in which the D5 SVEA-96 Optima3 dryout correlation will be applied to licensing analyses is summarized as follows:

For all SVEA-96 Optima3 mass flux values above the correlation upper limit of [

]^{a,c}.

For all SVEA-96 Optima3 mass flux values in the range of [

]^{a,c}.

5.3 STEADY-STATE D5 CPR CORRELATION

The steady-state critical power ratio for a SVEA-96 Optima3 sub-bundle is defined in the usual manner as:

$$\left[\right]^{a,c} \qquad (5.3\text{-}1)$$

where:

Q_{actual} = Actual sub-bundle power

[ ]^{a,c}:

$$\left[\right]^{a,c} \qquad (5.3\text{-}2)$$

where:

ε = Iteration convergence limit (typically 2×10^{-4})

[

]^{a,c}

Having determined the sub-bundle critical power, Q_c, to satisfy Equation 5.3-2, an axial distribution of CPR in the SVEA-96 Optima3 sub-bundle can be considered as:

a,c

[ ] (5.3-3)

Note that $\min_z\{CPR(z)\} = CPR_{min}$ per construction.

The D5 steady-state critical quality is defined as:

a,c

[ ] (5.3-4)

where:

a,c

[ ] (5.3-5)

a,c

[ ] (5.3-6)

and

[

]a,c

[

]^{a,c}

The remaining coefficients used for the D5 R-factor are defined in Section 5.6.

[

]^{a,c}

Each of the optimized functional forms defining the D5 critical quality are plotted in Figure 5-1 through Figure 5-4 using typical operating conditions (for the fixed parameters) and over a range wider than the correlation development range defined in Table 6-6. In each case, the bounding critical quality functions (i.e., least and most limiting within the correlation development range) are also plotted. [

]^{a,c} The range over which the D5 correlation is valid is provided and

justified in Section 6. In addition, direct comparison of the D5 predicted critical power with dryout test data and trends with various parameters are provided in Figure 4-9 through Figure 4-28.

5.4 D5 DRYOUT LOCATION PREDICTOR

For certain applications, mainly under transient conditions, it may be desirable to be able to predict the axial position of dryout in addition to the minimum CPR value. For this purpose a separate correlation has been developed which is referred to as the "D5 dryout location predictor." The D5 dryout location predictor is defined in exactly the same way as the steady-state CPR correlation (Section 5.3), [

]^{a,c}

The corresponding R-factor parameters associated with the D5 dryout location predictor are defined in Section 5.6.

5.5 D5 TRANSIENT CPR CORRELATION

The transient D5 CPR correlation is a generalization of the steady-state D5 CPR correlation defined in Section 5.3. It is based on the same correlation expression with the same empirical coefficients. Under steady-state conditions, the two correlations are equivalent. The R-factor determined at the transient initial condition is kept constant throughout the transient.

Transient I_2 Integral

It is not obvious how an integrated parameter such as I_2 should be applied to a transient. [

]^{a,c}

[

]a,c

Mass Flux

The transient mass flow rate was normalized to the inlet flow area for consistency with the steady-approach. The instantaneous outlet mass flux seen by a film fluid particle at the instant when it exits the bundle was selected for the transient D5 CPR correlation.

Pressure

Consistent with the definition of the transient mass flux, the instantaneous steam properties at the outlet were selected for the dependence on pressure.

The performance of the D5 CPR correlation has been investigated for various types of transients. The behavior with time is always smooth, indicating stability as ensured by the simple form of the correlation function (everywhere differentiable). [

]a,c

5.6 SUB-BUNDLE R-FACTOR FOR SVEA-96 OPTIMA3

The R-factor accounts for the influence of the local power distribution (relative rod power distribution in the sub-bundle), cross section geometry, and the spacer grid design and configuration. The traditional R-factor concept used, e.g., in the D4.1 correlation for SVEA-96 Optima2 (Reference 8) is basically two-dimensional (2D) and assumes that the axial and radial power distributions within the (sub-) assembly are separable (i.e., all fuel rods have the same axial power distribution). To deal with, e.g., partially controlled assemblies, ad hoc weighting schemes have been developed to combine the R-factors from different axial cross sections. With the introduction of part-length rods this modeling practice has become increasingly cumbersome and tedious to handle.

A generalized, fully three-dimensional (3D) R-factor model has been developed for SVEA-96 Optima3. The basic D5 R-factor for an individual fuel rod, i, at axial position, z, takes the following form:

$$R_i(z) = (1+e_i)\left[\frac{I_2(z)}{I_{2,i}(z)}\right]^a \frac{\left(\int_{z_B}^{z} q_i(z')dz'\right)^b + c\sum_{j\in S_i}\left(\int_{z_B}^{z} q_j(z')dz'\right)^b + d\sum_{k\in D_i}\left(\int_{z_B}^{z} q_k(z')dz'\right)^b}{\left(1+cN_{S_i}+dN_{D_i}\right)\left(\int_{z_B}^{z}\bar{q}(z')dz'\right)^b}, \quad (5.6\text{-}1)$$

where:

$$I_2(z) = \frac{\int_{z_B}^{z}\int_{z_B}^{z'}\bar{q}(z'')dz''dz'}{L\int_{z_B}^{z}\bar{q}(z')dz'} \quad (5.6\text{-}2)$$

and

$$I_{2,i}(z) = \frac{\int_{z_B}^{z}\int_{z_B}^{z'} q_i(z'')dz''dz'}{L\int_{z_B}^{z} q_i(z')dz'} \quad (5.6\text{-}3)$$

The following nomenclature is used:

z	=	Axial position discretized in nodes
i	=	Index for fuel rod considered
j	=	Index for side neighboring rod
k	=	Index for diagonal neighboring rod
$q_i(z)$	=	Linear heat generation rate of rod i in node z

$\bar{q}(z)$ = Average linear heat generation rate of all rods in node z

z_B = Axial position of bulk boiling boundary (zero steam quality limit)

S_i = Set of side neighboring rods for rod i

D_i = Set of diagonal neighboring rods for rod i

N_{S_i} = Number of side neighboring rods for rod i

N_{D_i} = Number of diagonal neighboring rods for rod i

a = Exponent for rod axial power profile dependence

b = Exponent for radial power dependence

c = Weighting constant for side neighboring rods

d = Weighting constant for diagonal neighboring rods

e_i = Dryout sensitivity constant for rod i (also denoted "rod constant")

The numbering of rods in the sub-bundle is done according to Table 5-1.

The calculation of CPR for individual fuel rods is based on the above rod specific R-factors. The calculation of the sub-bundle CPR is based on the maximum of all individual rod R-factors in each axial cross section,

$$R_{sub-bundle}(z) = \max_i \{R_i(z)\} \tag{5.6-4}$$

A convenient numerical property of the sub-bundle D5 R-factor is that its theoretical lower limit is determined by the average of rod sensitivity constants, $<1+e_i>$.

The parameters b, c, d, and e_i were determined from a best fit of the entire D5 CPR correlation against the FRIGG database for SVEA-96 Optima3, [

]^{a,c}

[

]^{a,c} The optimized rod constants (e_i) used for the development of the D5 CPR correlation and the D5 dryout location predictor are given in Figure 5-6 and Figure 5-7, respectively. Note that these are not the final rod constants used for analysis. As explained in Section 6.3, due to the consideration of some outlier data points, more limiting constants for two rods are defined in Figure 6-32 and Figure 6-33.

Considering R-factor expression in Equations 5.6-1, 5.6-2 and 5.6-3, the $I_2(z)$ is equivalent to the I_2 for the entire sub-bundle as defined in Equation 5.4-1. This follows from the fact that the integral of power is proportional to increment in steam quality. [

]^{a,c}

a,c

[ ] (5.6-5)

[

]a,c

Treatment of Part-Length Rods

The R-factor for part-length rods is not considered above the end of their heated length in the calculation of CPR for the sub-bundle. In this way, the sub-bundle R-factor axial distribution (Equation 5.6-4) will experience discontinuities at the 1/3 and 2/3 length levels if a part-length rod is limiting at these levels. For the (nearly) separable power distributions typically experienced by a CPR limiting assembly, the sub-assembly R-factor will be close to constant axially, apart from the possible steps at the 1/3 and 2/3 axial levels. The resulting critical steam quality is illustrated in Figure 5-8, along with the iterated steam quality for a bottom-peaked axial power distribution. For this case, the sub-assembly minimum CPR occurs at the 2/3 axial level due to a part-length rod.

[

]a,c

Use of Pin Power Reconstruction

For the previous types of CPR correlations, the R-factors used in core design and core supervision were pre-calculated based on idealized (fixed void and reflective single-assembly boundary) conditions evaluated with a 2D lattice code (e.g., PHOENIX4). This simplified approach is no longer needed with the D5 CPR correlation. [

]a,c The power distribution is no longer required to be separable into axial and radial components. In this way, for the CPR of SVEA-96 Optima3 fuel, one can now include the local power perturbations from surrounding core components such as:

- Heterogeneities in assembly reactivity (mainly due to differences in burnup for neighboring bundles)
- Control rods inserted in neighboring cells
- Neutron leakage at the core periphery

This allows a more accurate determination of the CPR for individual assemblies as well as the limiting CPR for the core.

The effects of using pin power reconstruction for CPR evaluation are demonstrated in Reference 6.

For some applications of the D5 correlation, such as the optimization of the bundle nuclear design or the calculation of channel bow impact on CPR, the traditional approach of using idealized power distributions may still be used.

5.7 CONVERSION OF SUB-BUNDLE R-FACTORS TO FULL-BUNDLE R-FACTORS

For some applications, e.g., transient hot-channel calculations, the axial R-factor distributions for the four SVEA-96 Optima3 sub-bundles need to be converted into one axial R-factor distribution for the entire fuel bundle. [

]^{a,c} In the process of preparing input R-factors for the transient calculation, the four sub-bundle R-factor vectors are collapsed into one full-bundle R-factor vector. Knowing the conditions for the initial state, an exact conversion is made in the sense that CPR obtained with the resulting full-bundle R-factor equals the minimum of CPR obtained in the four sub-bundles, at each axial level. [

]^{a,c}

a,c

[

]

The nomenclature is explained and the constants α_1 to α_{11} are given in Section 5.3.

5.8 DETERMINATION OF D5 COEFFICIENTS

Using the critical quality function established in Section 5-3, the D5 CPR correlation coefficients (α_1 to α_{11}) together with the R-factor coefficients (b, c, d, and e_i) were optimized for the [ ]^{a,c} points 24-rod sub-bundle database summarized in Table 4-1. The optimization was performed twice, once for the D5 CPR correlation and once for the D5 dryout location predictor.

A least squares method was used to optimize the correlation and R-factor coefficients by systematically minimizing the difference between the predicted and measured dryout power. [

]^{a,c} MEFISTO is a well-established and thoroughly validated industry code. It has been presented and reviewed at numerous industry conferences and has been used previously by Westinghouse to support the licensing of the D5 CPR correlation, e.g., in Germany. The MEFISTO code is not licensed by the US-NRC.

MEFISTO has been proven to accurately predict both the dryout power and the axial and lateral location of dryout for SVEA-96 Optima3 (Reference 9). [

]^{a,c}

[

]^{a,c} .

The resulting steady-state D5 CPR correlation was validated relative to the SVEA-96 Optima3 steady-state database as described in Section 6.

The conservatism of the transient D5 CPR correlation was validated relative to the SVEA-96 Optima3 transient database as described in Section 7.

Table 5-1 Numbering of Fuel Rods in a SVEA Sub-Bundle				
1	2	3	4	5
6	7	8	9	10
11	12	13	14	15
16	17	18	19	20
21	22	23	24	X

a,c

Figure 5-1 D5 Critical Quality Dependence on Mass Flux (Typical and Bounding Functions) Within (Dashed Box) and Outside Available Database

a,c

Figure 5-2 D5 Critical Quality Dependence on Pressure (Typical and Bounding Functions) Within (Dashed Box) and Outside Available Database

a,c

Figure 5-3 D5 Critical Quality Dependence on I_2 (Typical and Bounding Functions) Within (Dashed Box) and Outside Available Database

a,c

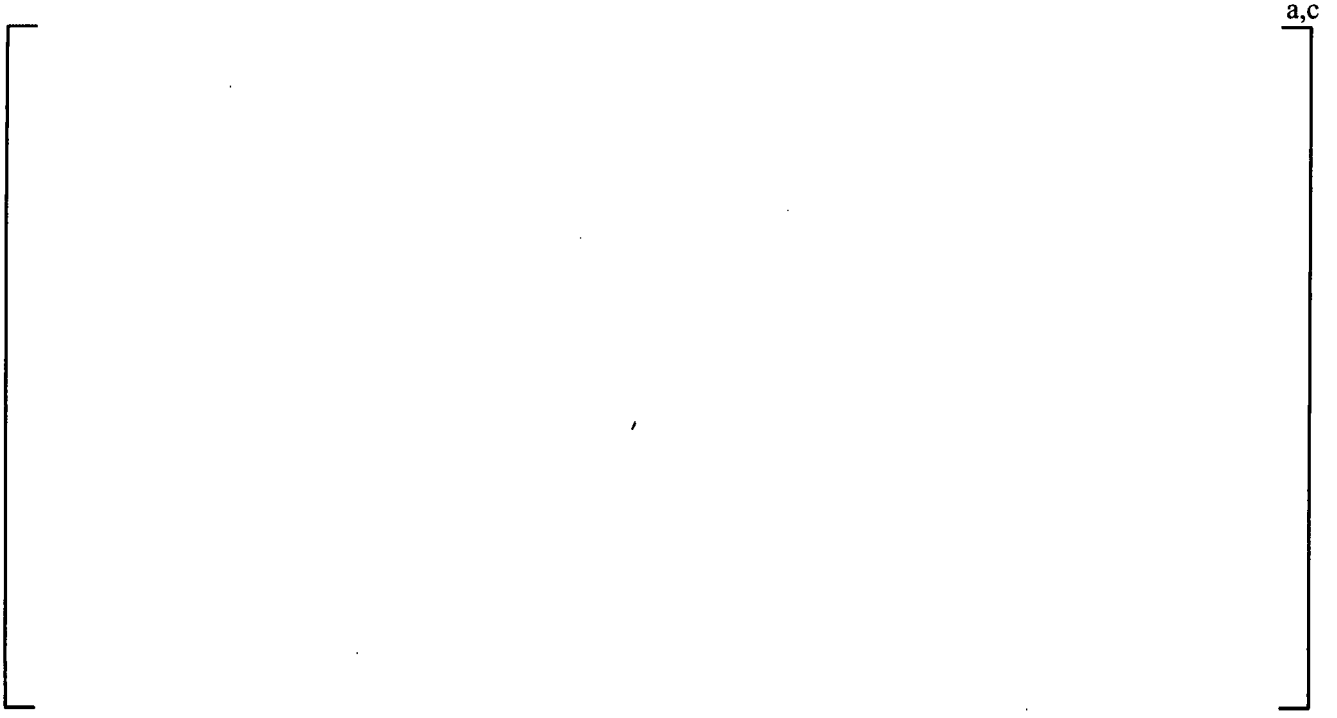

Figure 5-4 D5 Critical Quality Dependence on R-factor (Typical and Bounding Functions) Within (Dashed Box) and Outside Available Database

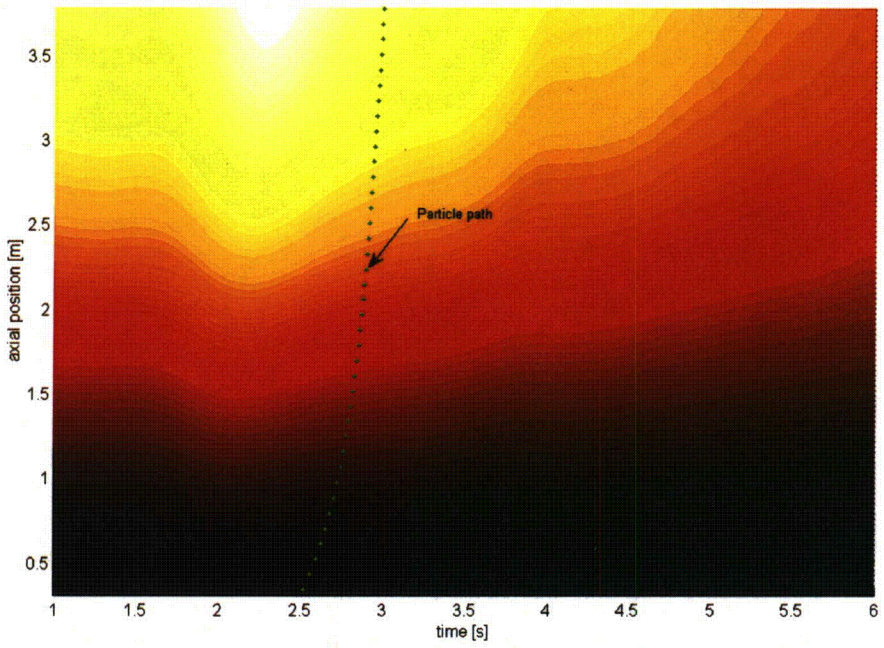

Figure 5-5 Non-equilibrium steam quality as function of time and space during a typical transient, together with the simulated trace of a fluid particle traveling at the velocity of the liquid phase. High steam quality (i.e., low dryout margin) is indicated with bright colors.

a,c

Figure 5-6 Best Fit SVEA-96 Optima3 Rod Constants for the D5 CPR Correlation Used During Development, But Not for Final Analysis

a,c

Figure 5-7 Best Fit SVEA-96 Optima3 Rod Constants for the D5 Dryout Location Predictor Used During Development, But Not for Final Analysis

a,c

Figure 5-8 Examples of axial distributions of critical (X_c) and iterated (X_{it}) steam qualities for a sub-bundle with bottom-peaked power distribution, where the sub-bundle minimum CPR occurs at the 2/3 axial level due to a part-length rod with high power.

6 STEADY-STATE CORRELATION EVALUATION

The steady-state CPR database is composed of [ ]^{a,c} points measured with a full scale 24-rod sub-bundle. All of these data points were used in the correlation derivation. The number of data points and local power distributions for each axial power distribution are summarized in Table 6-1. The 24-rod SVEA-96 Optima3 database obtained with the cosine, bottom- and top-peaked axial power distributions and test bundle local power distributions used to generate that database are given in Appendix A, B, and C, respectively.

Evaluation of the D5 CPR correlation relative to the steady-state database is contained in this section. In addition, Section 7 contains the evaluation of the D5 CPR correlation relative to transient critical power measurements.

6.1 D5 PERFORMANCE RELATIVE TO THE SVEA-96 OPTIMA3 DATABASE

Table 6-2 shows the mean prediction error, standard deviation, number of data points, and 95/95 upper tolerance limit for the D5 CPR correlation relative to the entire 24-rod SVEA-96 Optima3 database used for its development. The prediction error, ε, is given by:

$$\varepsilon = \left[\frac{\text{predicted critical power}}{\text{measured critical power}} - 1 \right] \times 100 \qquad (6\text{-}1)$$

As shown in Table 6-2, the mean prediction error and standard deviation over the entire SVEA-96 Optima3 database are [

]^{a,c}

Figure 6-1 is a comparison of the critical powers predicted with the D5 CPR correlation as a function of the measured critical powers for all [ ]^{a,c} data points used to develop the correlation. The solid lines in Figure 6-1 represent deviations from the measurement values of ± 5%. The designations "Cos," "Bot," and "Top" refer to data obtained with chopped cosine, bottom-peaked, and top-peaked axial power distributions, respectively. As shown in Figure 6-1, the D5 correlation shows good agreement with the measured data and does not show a bias as a function of critical power. Table 6-3 provides the number and percentage of predictions exceeding the 5% boundary.

A useful graphical validation technique is to study the trends of the error function (Equation 6-1) versus the measured parameters. An ideal prediction is characterized by ε = 0.0. Accordingly, the prediction error is plotted as a function of [

]^{a,c} in Figure 6-2 through Figure 6-6.

Figure 6-2 is the plot of the prediction error for the D5 CPR correlation relative to the entire [

]^{a,c}

Figure 6-3 is a plot of the prediction error for the D5 CPR correlation relative to the entire [

]^{a,c}

Figure 6-4 is a plot of the prediction error for the D5 correlation relative to the [

]^{a,c}

Figure 6-5 is a plot of the prediction error for the D5 correlation relative to the [

]^{a,c}

Figure 6-6 is a plot of the prediction error for the D5 correlation relative to the [

]^{a,c}

In Summary, Figure 6-2 through Figure 6-6 demonstrate that the D5 correlation provides a good fit to the test data with no systematic biases which would limit the validity of the correlation to predict the bundle critical power performance in design and licensing applications.

Figure 6-7 is a frequency distribution of the prediction error for the SVEA-96 Optima3 database. [

]^{a,c}

Figure 6-8 shows the critical power dependence on mass flux for the three different axial power shapes tested, as predicted by D5 with typical values assumed for the remaining correlation parameters. As shown in Figure 6-8, [

]^{a,c}

Similarly, Figure 6-9 shows the D5 critical power dependence on inlet subcooling for several different mass flux values. As shown in Figure 6-9, [

]^{a,c}

Table 6-4 shows mean value and standard deviation for the prediction error, number of data points, and 95/95 upper tolerance limit [

]^{a,c}

[

]^{a,c}

Figure 6-10 through Figure 6-12 present the same information as Figure 6-2 in which the prediction errors are plotted as a function of mass flux, but here the data were sorted for the cosine-shaped, bottom-peaked, and top-peaked axial power shapes, respectively. Table 6-5 provides the mean prediction errors, standard deviations, and numbers of data points for various mass flux ranges.

Additional plots of the prediction error as a function of mass flux, pressure, and inlet subcooling for selected subsets of the database including the fringe areas of operation are presented in Figure 6-13 through Figure 6-31. As can be seen from these figures, there are no significant trends or biases in the D5 CPR correlation predictions. These figures demonstrate that the D5 CPR correlation is applicable in the fringe areas of operation and is supported by a sufficient number of data points in these areas. The figures also illustrate the good performance of the correlation at nominal conditions.

In summary, the following conclusions can be drawn from the evaluation of the D5 CPR correlation predictions over the 24-rod SVEA-96 Optima3 database:

1. All trends in the critical power database discussed in Section 4 are adequately captured with the D5 CPR correlation. Furthermore, predicted critical power trends with [ ]^{a,c} are consistent with previous dryout testing of earlier assembly designs.

2. The quality of the D5 CPR correlation predictions does not show any evidence [ ]^{a,c}

3. Therefore, it is concluded that the D5 CPR correlation provides a satisfactory fit to the data to justify its use for design and licensing applications. A normal uncertainty distribution with a mean error of [ ]^{a,c} provides a good characterization of the steady-state prediction error distribution for the SVEA-96 Optima3 database used for development.

6.2 RANGE OF APPLICABILITY

6.2.1 Introduction

The range over which a CPR correlation is traditionally valid corresponds to the experimental range over which the correlation was developed and yields the claimed statistical performance (i.e., mean value and standard deviation). This development range is provided in Table 6-6. Correlation applicability outside this range can, however, be justified (1) by conservatively bounding the critical power based on known monotonous asymptotic behavior of the physical phenomena or (2) by comparing the correlation performance to a physical model of the dryout event in the same rod bundle geometry over the targeted application range.

The range of applicability for the mass flux has been discussed in Section 5.2 where the bounding method (1) was used at low flow (by limiting the critical quality) and high flow (by limiting the critical power) beyond the FRIGG experimental database. In this section, the D5 CPR correlation applicability to axial and radial power profiles outside the experimental database is discussed.

Method (2) requires the use of a sound physical model of the dryout event in the appropriate rod bundle geometry which is valid over the targeted range of applicability. Such models have been developed in the past and are continuously being improved by various investigators, including at Westinghouse. Based on physical consideration of two-phase annular flow in open sub-channels, the governing equations for the multi-film, drop, and steam fields are resolved in each geometric sub-channel (defined by the fuel rods), accounting for:

- The energy transfer from the heated wall to the liquid film field
- The coupled mass and energy transfer across the fields (entrainment, deposition, evaporation)
- The cross-flow between sub-channels
- The spacer grids and part-length rod effects on the field distribution

The Westinghouse MEFISTO code incorporates such mechanistic modeling of dryout under steady-state conditions (see Reference 9). When MEFISTO is adapted to a particular fuel bundle design, such as the SVEA-96 Optima3 sub-bundle, the effects of the spacer grids on downstream drop deposition are calibrated against critical power data by adjusting one single free parameter (drop deposition enhancement coefficient) per sub-channel. For SVEA-96 Optima3, this calibration was done against a small part (~20%) of the cosine data series. The capability of MEFISTO to extrapolate to other axial power profiles was then validated using the bottom- and top-peaked data series. When replacing the cosine axial power distribution with the bottom-peaked (top-peaked) distribution, the critical power increases (decreases) by approximately 10% (cf. Figure 6-8). In spite of the relatively large changes in critical power, the mean error (bias) in the predictions by MEFISTO for the bottom- and top-peaked power shapes is generally less than 1% and the standard deviation less than 4% (see Reference 9).

Using a mechanistic dryout code such as MEFISTO, the dryout power can be readily calculated corresponding to the condition where the film flow-rate (or thickness) becomes sufficiently low. Such an approach to the assessment of a CPR correlation for conditions outside the development database has been used previously for licensing of the D4 CPR correlation to support its conservative applicability to double-hump shape axial power distribution (Reference 8). In the case of the SVEA-96 Optima3 geometry, a similar approach was used to assess and qualify the D5 CPR correlation behavior over a range of applications beyond the correlation development range, in terms of axial power distribution (characterized by the transformation of axial power profile: I_2, see subsection 6.2.2) and radial power distribution (characterized by the R-factor, see subsection 6.2.3).

6.2.2 Considerations for Various Types of Axial Power Distributions

The D5 CPR correlation is based on top-peaked, bottom-peaked, and cosine-shaped axial power distributions. As shown in Section 6.1, this correlation exhibits a very good fit to the [ ]^{a,c}-point FRIGG loop database described in Section 4. The implicit assumption in basing the CPR correlation on these axial power shapes is that intermediate power shapes and combinations of these shapes will be

adequately captured by the correlation provided that the cosine, top-peaked, and bottom-peaked shapes are correctly captured.

In order to make a quantitative assessment of the performance of the I_2 concept for various double-hump power distributions, a comparison with the calculation results obtained with the MEFISTO code was done for the SVEA-96 Optima3 sub-bundle geometry. The results of the D5 CPR correlation have been shown to be in good agreement with the results from MEFISTO, that is, the deviations are within the expected range based on the CPR correlation and physical model uncertainties.

As a consequence, and [

]^{a,c}

Furthermore, the D5 CPR correlation is also expected to be applied to axial power distributions more peaked that the test in FRIGG experimental database. This happens, in particular, when applying the correlation to very bottom-peaked and very top-peaked axial power distributions. For such cases, comparison with the calculation results from MEFISTO using the SVEA-96 Optima3 fuel bundle geometry was also performed. Various realistic bottom-peaked shapes and top-peaked shapes were analyzed. Again, the results showed good agreement between the D5 CPR correlation and MEFISTO, that is, within the expected range based on the calculated CPR correlation and physical model uncertainties.

Thus, it is concluded that the D5 CPR correlation, based on the physical transformation of axial power profile (I_2), is applicable to axial power profiles other than the experimental FRIGG profiles it is based on, without change in prediction uncertainties and without any special correction.

6.2.3 Consideration for Radial Power Distribution

The D5 CPR correlation is based on a new R-factor model which was documented in Section 5.6. This new model more physically accounts for the influence of part-length rods on dryout power and is based on critical power experiments with a broader range of radial power distributions than previously tested. As a result, the D5 R-factor model is more robust to extrapolation of radial power distribution outside the measurement range. The D5 R-factor model has been developed using, among others, radial power distributions that give the optimized (highest) critical power and hence extrapolation is not relevant in the lower range of R-factors (near 1.0). However, it is expected that, in particular situations, the new R-factor model will be used beyond the upper limit of [ ]^{a,c} tested in the experiments. Relevant conditions for this to occur could be large radial power gradients experienced close to the core periphery or in the vicinity of deeply inserted control rods, possibly in combination with power suppression in rods with high residual concentrations of burnable absorber material. Although such conditions are generally not limiting for CPR it is desired to include those conditions in the range of validity for the D5 CPR correlation.

The physical model of the MEFISTO code is well-suited for extrapolation in rod power peaking. A comparison of results obtained with the D5 CPR correlation and MEFISTO was performed for the SVEA-96 Optima3 fuel bundle geometry assuming various radial power distributions yielding high R-factors [ ]^{a,c}. The results once again showed a good agreement between the D5 CPR correlation and

the MEFISTO code, that is, within the expected range based on the CPR correlation and physical model uncertainties.

6.2.4 Final Range of Applicability

Based on the previous analysis, the final range over which the D5 CPR correlation is applicable is shown in Table 6-7. This range is based on the entire [

]^{a,c}

The use of the D5 CPR correlation is intended for sub-bundles that have a reasonable possibility of being CPR limiting for the core, when considering all uncertainties affecting the calculation of CPR (including the uncertainty of the CPR correlation model itself and the uncertainties in all of its input variables). Sub-bundles that have a large margin (e.g., [ ]^{a,c}) to the core minimum CPR are therefore excluded in the validity range check.

6.3 CONSIDERATION OF EXCLUDED DATAPOINTS

Some FRIGG data points that were initially excluded in the development of the D5 CPR correlation and the D5 dryout location predictor are discussed in this section. These data points are conservatively considered in the final overall CPR correlation uncertainty to be used for design and licensing applications.

6.3.1 Excluded FRIGG Data Points

During the FRIGG campaign for SVEA-96 Optima3, the rod CPR performance of the test bundle behaved as expected, except for one rod in the bottom-peaked test series. For this particular test series, Rod 14 (see numbering in Table 5-1) showed an abnormal sensitivity to dryout resulting in a critical power of about 15% less than expected.. The symmetrical rod (Rod 18) did not show any abnormal sensitivity to dryout. In addition, no physical reason indicates that Rod 14 would be more sensitive to dryout for a bottom-peaked axial power shape as compared to cosine and top-peaked axial power distributions. The reason for this enhanced sensitivity is, therefore, likely to be specific to the FRIGG test set up. It was decided that the data points from the bottom-peaked test series where Rod 14 was the only rod registered in dryout should not be allowed to influence the optimization of the coefficients in the D5 CPR correlation and D5 dryout location predictor, except for the particular rod constant associated with the symmetry pair of Rods 14 and 18. A careful examination of Rod 14 has not revealed any obvious malfunctioning of this rod or its signal devices, and the data points have hence to be included in a conservative manner in the determination of the associated rod constant and the final evaluation of the CPR correlation uncertainty.

Also, a few data points were collected at mass flux below [ ]^{a,c}, but due to the higher uncertainties in the flow measurements these data points were removed from the database.

6.3.2 Final Correlation Adjustment

The D5 CPR correlation and D5 dryout location predictor form and empirical constants were initially developed based on [ ]^{a,c} data points in the SVEA-96 Optima3 database (see Section 4), i.e., without considering the bottom-peaked data points where only Rod 14 was registered in dryout. The latter were considered outliers that would lead to an incorrect behavior of the correlation. Instead, these data points were accounted for later in a re-adjustment of the R-factor rod constant for the symmetrical pair of Rods 14 and 18 in a best-estimate manner considering all dryout indications on these rods, while keeping all other correlation coefficients fixed. This ensures that the correlation basis is developed using only physically sound data points and therefore behaves correctly, while accounting for the larger uncertainty due to the higher dryout sensitivity of Rod 14 observed during a part of the experiment. The updated R-factor rod constant for Rods 14 and 18 used in the final adjustment of the D5 CPR correlation and the D5 dryout location predictor can be found in Figure 6-32 and Figure 6-33, respectively. These are the final rod constants that shall be used in safety analysis and licensing applications. Only the rod constant for Rods 14 and 18 has been changed, as compared to Figure 5-6 and Figure 5-7.

6.3.3 Final D5 CPR Correlation Uncertainty

The correlation statistics were re-evaluated based on the modified R-factor rod constant for the Rod 14 and 18 symmetry pair (Figure 6-32 and Figure 6-33), using the entire FRIGG database [

]^{a,c} were obtained. This standard deviation will be used for steady-state design and licensing applications. The negative bias in the mean error caused by the re-adjusted rod constant for Rods 14 and 18 will not be accounted for. Specifically, [ ]^{a,c} are appropriate to support Safety Limit Minimum Critical Power Ratio (SLMCPR) evaluations for SVEA-96 Optima3 fuel.

Table 6-1 Number of Data Points and Local Power Distributions

Axial Power Profile	Number of Data Points	Number of Radial Power Distributions

a,c

Table 6-2 Mean Prediction Errors and Standard Deviations for D5 CPR Correlation

	Mean Prediction Error [1] (%)	Standard Deviation (%)	Number of Data Points	One-Sided 95/95 Upper Tolerance Limit (%)

a,c

Note: Prediction error is defined by Equation 6-1.

Table 6-3 Number and Percent of Calculated Data Points Exceeding the 5% Boundary

Axial Power Distribution	No. Of Data Points	No. Of Data Points Exceed 5% Boundary	Percent of Data Points Exceed 5% Boundary

a,c

Table 6-4 Mean Prediction Error and Standard Deviations for D5 CPR Correlation for Data Ranges

Pressure Range (bar)	Mass Flux Range (kg/m^2/s)	Subcooling Range (C)	Mean Error (%)	Standard Deviation (%)	Number of Points	One-sided 95/95 Upper Tolerance Limit (%)

a,c

Note: Range a to b means $a \leq x < b$.

Table 6-5 Mean Values and Standard Deviations of the Prediction Error for Various Mass Flux Ranges

a,c

Note: Range is defined as Lower Bound ≤ Mass Flux < Upper Bound.

Table 6-6 Development Range for D5

a,c

Parameter	Range of development

Table 6-7 Validity Range for D5

a,c

Parameter	Range of validity

a,c

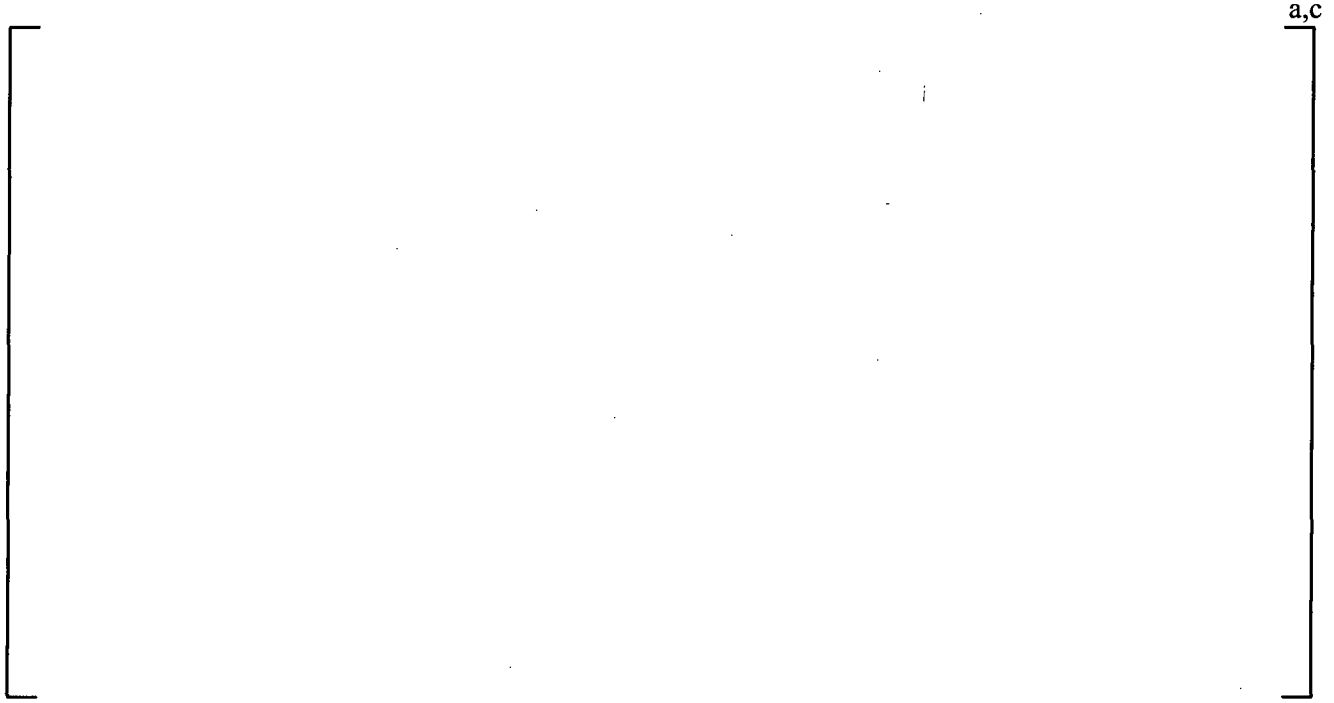

Figure 6-1 D5 Predicted Versus Measured Critical Power for all Data Points – the Lines Represent ±5% Error

a,c

Figure 6-2 D5 Prediction Error as a Function of Mass Flux for all Data Points

a,c

Figure 6-3 D5 Prediction Error as a Function of Outlet Pressure for all Data Points

a,c

Figure 6-4 D5 Prediction Error as a Function of Inlet Subcooling for all Data Points

a,c

Figure 6-5 D5 Prediction Error as a Function of Transformation of Axial Power Profile for all Data Points

a,c

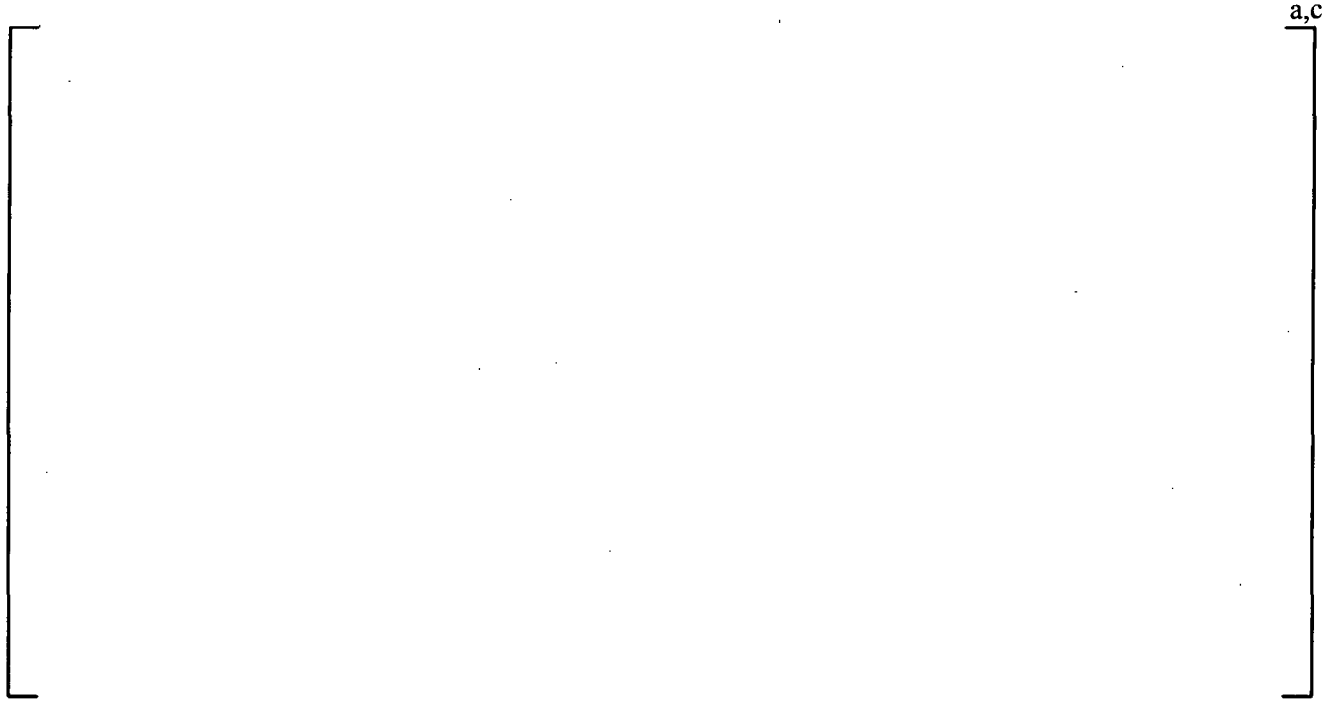

Figure 6-6 D5 Prediction Error as a Function of R-factor for all Data Points

a,c

Figure 6-7 D5 for all Test Data – Histogram of Frequency Versus CPR Error

a,c

Figure 6-8 D5 Critical Power Dependence on Flow and Axial Power Shape (Pressure = 70 bar, Subcooling = 10 K, R-factor = 1.05)

[a,c]

Figure 6-9 D5 Critical Power Dependence on Subcooling

a,c

Figure 6-10 D5 Prediction Error as a Function of Mass Flux for Cosine Axial Power Profile

a,c

Figure 6-11 D5 Prediction Error as a Function of Mass Flux for Bottom-Peaked Axial Power Profile

a,c

Figure 6-12 D5 Prediction Error as a Function of Mass Flux for Top-Peaked Axial Power Profile

a,c

Figure 6-13 Prediction Error versus Mass Flux at 29 Bar

Figure 6-14 Prediction Error versus Mass Flux at 69 Bar

a,c

Figure 6-15 Prediction Error versus Mass Flux at 84 Bar

a,c

Figure 6-16 Prediction Error versus Subcooling at 29 Bar

a,c

Figure 6-17 Prediction Error versus Subcooling at 69 Bar

a,c

Figure 6-18 Prediction Error versus Subcooling at 84 Bar

a,c

Figure 6-19 Prediction Error versus Mass Flux at 5 Degree C Subcooling

a.c

Figure 6-20 Prediction Error versus Mass Flux at 10 Degree C Subcooling

a,c

Figure 6-21 Prediction Error versus Mass Flux at 25 Degree C Subcooling

a,c

Figure 6-22 Prediction Error versus Mass Flux at 40 Degree C Subcooling

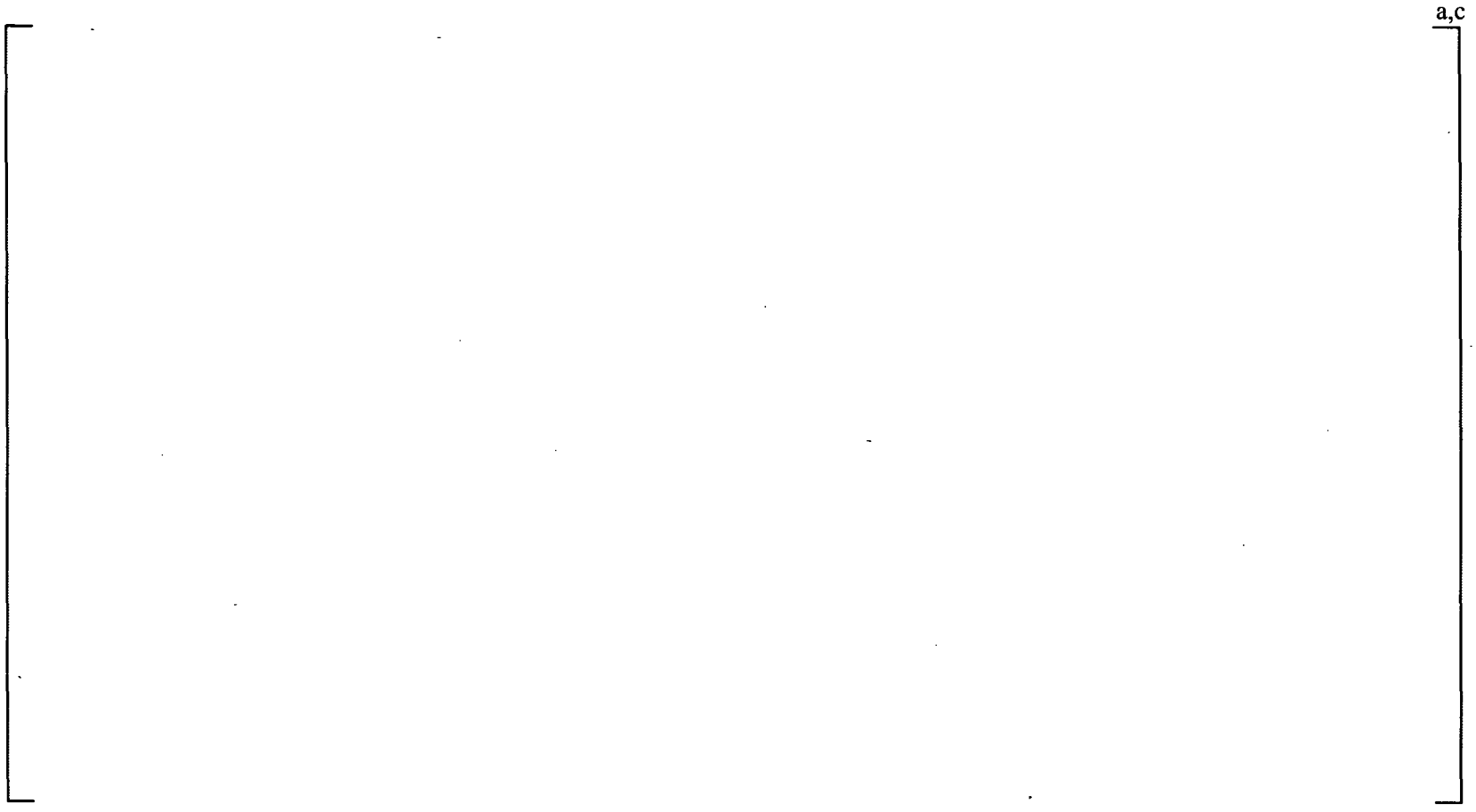

Figure 6-23 Prediction Error versus Mass Flux for an R-factor of 1.04

a,c

Figure 6-24 Prediction Error versus Mass Flux for an R-factor of 1.06

a,c

Figure 6-25 Prediction Error versus Mass Flux for an R-factor of 1.08

a,c

Figure 6-26 Prediction Error versus Pressure for an R-factor of 1.04

a.c

Figure 6-27 Prediction Error versus Pressure for an R-factor of 1.06

a,c

Figure 6-28 Prediction Error versus Pressure for an R-factor of 1.08

a.c

Figure 6-29 Prediction Error versus Subcooling for an R-factor of 1.04

a,c

Figure 6-30 Prediction Error versus Subcooling for an R-factor of 1.06

a,c

Figure 6-31 Prediction Error versus Subcooling for an R-factor of 1.08

a,c

Figure 6-32 Final Rod Constants (D5 CPR Correlation)

a,c

Figure 6-33 Final Rod Constants (D5 Dryout Location Predictor)

7 CONFIRMATION FOR TRANSIENT APPLICATION

7.1 INTRODUCTION

One specified acceptable fuel design limit (SAFDL) is that no more than 0.1% of the fuel rods in the core experience boiling transition during an AOO and during normal operation. This requirement is typically satisfied by evaluating the change in CPR (ΔCPR) during licensing basis AOOs and establishing a CPR operating limit such that the SLMCPR will not be violated during limiting transient events.

Transient CPR predictions involve evaluation of the flow, enthalpy, and pressure in the fuel assembly at each axial node as a function of time during the transient. A transient systems analysis code is used to calculate the transient fluid parameters. These parameters are then used with the CPR correlation for an assembly to evaluate transient CPR. One transient systems analysis code used by Westinghouse for CPR predictions is the BISON-SLAVE channel model of the BISON transient analysis code documented in References 3 and 4.

The methodology for demonstrating that the application of the D5 correlation in transient calculations will provide conservative predictions of ΔCPR is described in this section. Specifically, the process for qualifying implementation of the D5 correlation in transient codes is described. Then, the transient experiments performed in the FRIGG test loop to qualify the transient code implementation for SVEA-96 Optima3 are described. Finally, the D5 correlation validation in the BISON-SLAVE transient code is presented. This methodology is also be used to confirm that CPR changes during transient events are conservatively treated in other licensed transient codes.

7.2 TRANSIENT IMPLEMENTATION VALIDATION METHODOLOGY

The three objectives of the transient systems analysis code implementation validation are to:

1. Confirm proper implementation of the transient CPR correlation in the transient code.

2. Confirm the capability of the transient CPR correlation implemented in the transient code to calculate dryout during transients with adequate accuracy.

3. Confirm the capability of the transient CPR correlation in combination with the rod model implemented in the transient code to provide predictions of the rod cladding temperature with adequate accuracy.

Transient code implementation of the D5 CPR correlation is validated for each code application by
[

]^{a,c}

7.3 TRANSIENT DRYOUT EXPERIMENTS

The transient tests used to validate the D5 transient CPR correlation resulted in a transient validation database for the Westinghouse SVEA-96 Optima3 fuel design. The transient CPR data were taken in controlled transient experiments performed in the FRIGG test loop. The measurements were performed for three different axial power profiles and included numerous different initial parameter variations as well as transient event simulations. The application of these tests to validate the D5 transient CPR correlation for transient applications is described in this section.

7.3.1 FRIGG Loop

The transient tests for SVEA-96 Optima3 were carried out with the test bundles described in Section 3 incorporating the three axial power profiles:

- Bottom-peaked using Test Bundle SF24XB
- Cosine-shaped using Test Bundle SF24XC
- Top-peaked using Test Bundle SF24XT

Therefore, the transient tests were performed with the same test sections and test facility used in the steady-state experiments described in Section3, and the three axial power distributions used in the transient tests are shown in Figure 3-5 through Figure 3-7. Power increase transients, flow reduction transients, and combination of power increase and flow reduction transients are simulated in the FRIGG loop transient tests. [

]^{a,c}

A power supply controller capable of producing power pulses providing heat flux variations which simulate BWR fast pressurization events was used for the transient test simulations. Rapid test loop flow decreases, which are needed to simulate the very fast flow reductions in BWRs with internal pumps, were accomplished by rapid closure of a valve between the recirculation pump and the test section inlet.

Dynamic heater rod thermocouple responses are recorded as a function of time during the transient tests. In addition, transient test system response data are recorded in order to provide time-dependent boundary conditions for the transient system code simulations. The test section [

]^{a,c}.

7.3.2 Test Section

The same SF24XC, SF24XB, and SF24XT test sections used for the steady-state testing described in Section 3 were used for the transient tests.

7.3.3 Transient Tests Description

The SVEA-96 Optima3 transient tests can be categorized as power increase, flow reduction, or combination transients for various axial power shapes, transient power and flow histories, and test section flow rates. All tests were performed for [

]^{a,c}.

Each of the tests was performed with one of the axial power shapes shown in Table 3-1 through Table 3-3. [

]^{a,c}

Power and flow transient events were simulated in the FRIGG Loop transient tests using [

]^{a,c}.

The power and flow transient profiles shown in Figure 7-1 and Figure 7-2, as well as [

]^{a,c}

The scope of the tests can be further clarified by grouping them according to axial power shape and categorization as power increase, flow reduction, or combination tests. Table 7-1 to Table 7-3, Table 7-4 to Table 7-5, and Table 7-6 to Table 7-8 summarize the tests performed with the bottom-peaked, cosine-shape, and top-peaked axial power shapes, respectively. [

]^{a,c}

7.3.4 Dryout Threshold Temperature

The dryout threshold temperature is the temperature increase during the transient which is assumed to indicate dryout (e.g., calculated CPR equals 1.0). The dryout threshold temperature in the transient tests was an increase of [

]^{a,c}

[

]a,c

7.3.5 Transient Data

Sample test boundary conditions for a power increase test (Test Number 1304, cosine test), a flow reduction test (Test Number 1290, top-peaked test), and a combination test (Test Number 1226, top-peaked test) are shown in Figure 7-3, Figure 7-5, and Figure 7-7, respectively. The corresponding limiting rod temperature responses are shown in Figure 7-4, Figure 7-6, and Figure 7-8, respectively. The power increase test was performed with a cosine axial power shape using Test Section SF24XC while the flow reduction and the combination test were performed with a top-peaked axial power distribution using Test Section SF24XT. These figures show the test section power and coolant inlet flow as functions of time. The inlet coolant flow measurement is used as a boundary condition in the transient code simulations. [

]a,c

For the [

]a,c

Test Number 1290 is an example of a [

]a,c

It should be noted that the entire signal recording time range is not shown in Figure 7-3 through Figure 7-8. Only 10 seconds of the transients in Test Number 1304 are shown, of which about 2 seconds is initial steady-state operation. Thirty seconds of the transient for Test Numbers 1290 and 1226 are shown, of which more than 10 seconds is initial steady-state operation.

The raw temperature signals leading to the type of traces in Figure 7-4, Figure 7-6, and Figure 7-8 [

]a,c.

The traces in Figure 7-3 through Figure 7-8 are provided to illustrate the type of responses for typical test power and flow histories used in the SVEA-96 Optima3 tests. Plots such as those shown in Figure 7-3 through Figure 7-8 provide physical insight into the transient response to the test boundary conditions and assure that any anomalies are detected.

Table 7-9 through Table 7-11 summarize the measured results from all of the transient tests.

7.4 IMPLEMENTATION VALIDATION FOR BISON CODE

The BISON-SLAVE channel model in the time domain reactor dynamics code BISON (References 3and 4) will be used in conjunction with the D5 CPR correlation to predict transient CPR behavior for reload fuel licensing analysis applications. The BISON-SLAVE simulations presented in this section are an illustration of the methodology described in Section 7.2 for confirming that the D5 transient CPR correlation is acceptable for transient application.

An overview of the BISON code and test section model is described below. The transient test simulation results are compared with the measurements.

7.4.1 BISON Code

BISON is a time domain BWR dynamics code used for analyzing operational and safety-related transients. The code simulates the hydraulics of the entire primary core coolant loop including the recirculation pumps. A two-group diffusion theory model describes the axial distributions of neutron flux and power in the reactor core. Heat conduction in the fuel is solved in the radial direction at each axial segment. The influence from external systems such as the turbine, control systems, scram signals, and relief valves can also be simulated in BISON.

The BISON-SLAVE module of the code is used for the simulation of a single bundle in the core by utilizing boundary conditions from a BISON systems calculation for the entire reactor. It can also be used in a stand-alone mode to study heated bundles in loop experiments. External boundary conditions in the form of inlet mass flow and temperature, inlet pressure, and assembly power are supplied as input to the code. This option was used in the present evaluation to calculate the transient CPR for the experiments performed.

The D5 transient CPR correlation is incorporated in the BISON-SLAVE code. Fluid properties (e.g., [ ]^{a,c}) as defined in Section 5.5 are used in evaluating the CPR correlation under transient conditions.

The initial solution of D5 in BISON-SLAVE is performed in the same manner as described in Section 5.3 using equilibrium conditions. The time dependent evaluation of D5 is performed using non-equilibrium conditions and a scaling is applied to account for the differences between the initial equilibrium evaluation and the transient non-equilibrium evaluation.

7.4.2 BISON Model

The [ ]^{a,c} are modeled in the BISON simulations of the tests. The heated part of the test section is simulated with the BISON-SLAVE channel model. The heater rod is modeled with the same radial nodal divisions typically used in plant calculations. The radial representation and material compositions of the heater rod are shown in Figure 7-9.

In addition, a second hot rod is simulated and used to calculate the rod temperature also after dryout occurs.

The experimental conditions described in the previous sections were used as input to the BISON-SLAVE model. [

]^{a,c}

The CPR during the transient is calculated using the transient D5 CPR correlation (see Section 5.5) implemented in the BISON code.

7.4.3 BISON Test Simulation Results

All [ ]^{a,c} tests were simulated with the BISON-SLAVE code. The initial and boundary conditions input to each BISON-SLAVE test point simulation, the predicted and measured times to dryout, the experimental temperature change indicating whether or not dryout occurred, and the predicted minimum CPR for each test are listed in Table 7-9 to Table 7-11 for the bottom-peaked, cosine-shaped, and top-peaked axial power distributions, respectively. Figure 7-10 through Figure 7-12 show the [

]^{a,c}. As discussed in subsection 7.3.4, dryout is indicated in the test results by the criterion of a maximum temperature change greater than or equal to [ ]^{a,c}. Dryout is indicated in the BISON-SLAVE simulation by a CPR prediction less than 1.0. A non-conservative BISON-SLAVE prediction occurs when the dryout is indicated by the test but not by the simulation (MCPR > 1.0). Therefore, a non-conservative BISON-SLAVE prediction is indicated [

]^{a,c}.

As shown in Table 7-9 through Table 7-11 and Figure 7-10 through Figure 7-12, [

]^{a,c}

Finally, a comparison between measured and BISON-SLAVE predicted maximum cladding temperature change during all FRIGG transients was performed for bottom-peaked (Figure 7-13), cosine (Figure 7-14), and top-peaked (Figure 7-15) axial power distribution. Cladding temperature is calculated with [

]^{a,c}. The results show very good agreement with the experimental observations,

supporting the dryout prediction capability of BISON-SLAVEin combination with the D5 correlation to predict the cladding temperature increase during a transient event.

7.5 SUMMARY

The systematic Westinghouse methodology used to confirm the conservative application of a CPR correlation for transient CPR code applications is illustrated in this section for the D5 transient CPR correlation and BISON-SLAVE channel model. Comparisons of BISON-SLAVE code predictions with SVEA-96 Optima3 sub-bundle test results in this section demonstrate that the D5 transient CPR correlation is capable of providing conservative estimates of the onset of dryout during transients. It is concluded that the D5 transient CPR correlation used in the BISON-SLAVE channel model provides sufficiently conservative predictions of the transient dryout test data to demonstrate that the D5/BISON-SLAVE combination will not underestimate the CPR response of the operational transients to which it will be applied and will support conservative CPR operating limits.

Table 7-1 SF24XB – Test Matrix for Power Increase Transients with Bottom-Peaked Axial Power Shape				
Power Profile	Flow Profile	Initial Flow Level (kg/s)	Sub-Cooling (K)	Test Number

a,c

Table 7-2 SF24XB – Test Matrix for Flow Decrease Transients with Bottom-Peaked Axial Power Shape				
Power Profile	Flow Profile	Initial Flow Level (kg/s)	Sub-Cooling (K)	Test Number

a,c

Table 7-3 SF24XB – Test Matrix for Combination Transients with Bottom-Peaked Axial Power Shape				
Power Profile	Flow Profile	Initial Flow Level (kg/s)	Sub-Cooling (K)	Test Number

a,c

Table 7-4 SF24XC – Test Matrix for Power Increase Transients with Cosine Axial Power Shape

Power Profile	Flow Profile	Initial Flow Level (kg/s)	Sub-Cooling (K)	Test Number

a,c

Table 7-5 SF24XC – Test Matrix for Flow Decrease Transients with Cosine Axial Power Shape

Power Profile	Flow Profile	Initial Flow Level (kg/s)	Sub-Cooling (K)	Test Number

a,c

Table 7-6 SF24XT – Test Matrix for Power Increase Transients with Top-Peaked Axial Power Shape

Power Profile	Flow Profile	Initial Flow Level (kg/s)	Sub-Cooling (K)	Test Number

a,c

Table 7-7 SF24XT – Test Matrix for Flow Decrease Transients with Top-Peaked Axial Power Shape

Power Profile	Flow Profile	Initial Flow Level (kg/s)	Sub-Cooling (K)	Test Number

a,c

Table 7-8 SF24XT – Test Matrix for Combination Transients with Top-Peaked Axial Power Shape

Power Profile	Flow Profile	Initial Flow Level (kg/s)	Sub-Cooling (K)	Test Number

a,c

Table 7-9 SF24XB – Bottom-Peaked Test Results and BISON/SLAVE Predictions a,b,c

Table 7-9 SF24XB – Bottom-Peaked Test Results and BISON/SLAVE Predictions (cont.)

a,b,c

[

]

Table 7-9 SF24XB – Bottom-Peaked Test Results and BISON/SLAVE Predictions (cont.)

a,b,c

Table 7-10 SF24XC – Cosine Test Results and BISON/SLAVE Predictions

a,b,c

Table 7-10 SF24XC – Cosine Test Results and BISON/SLAVE Predictions (cont.)

a,b,c

Table 7-11 SF24XT – Top-Peaked Test Results and BISON/SLAVE Predictions a,b,c

Table 7-11 SF24XT – Top-Peaked Test Results and BISON/SLAVE Predictions (cont.)

a,b,c

Table 7-11 SF24XT – Top-Peaked Test Results and BISON/SLAVE Predictions (cont.)

a,b,c

a.c

Figure 7-1 Power-Time Profiles

a.c

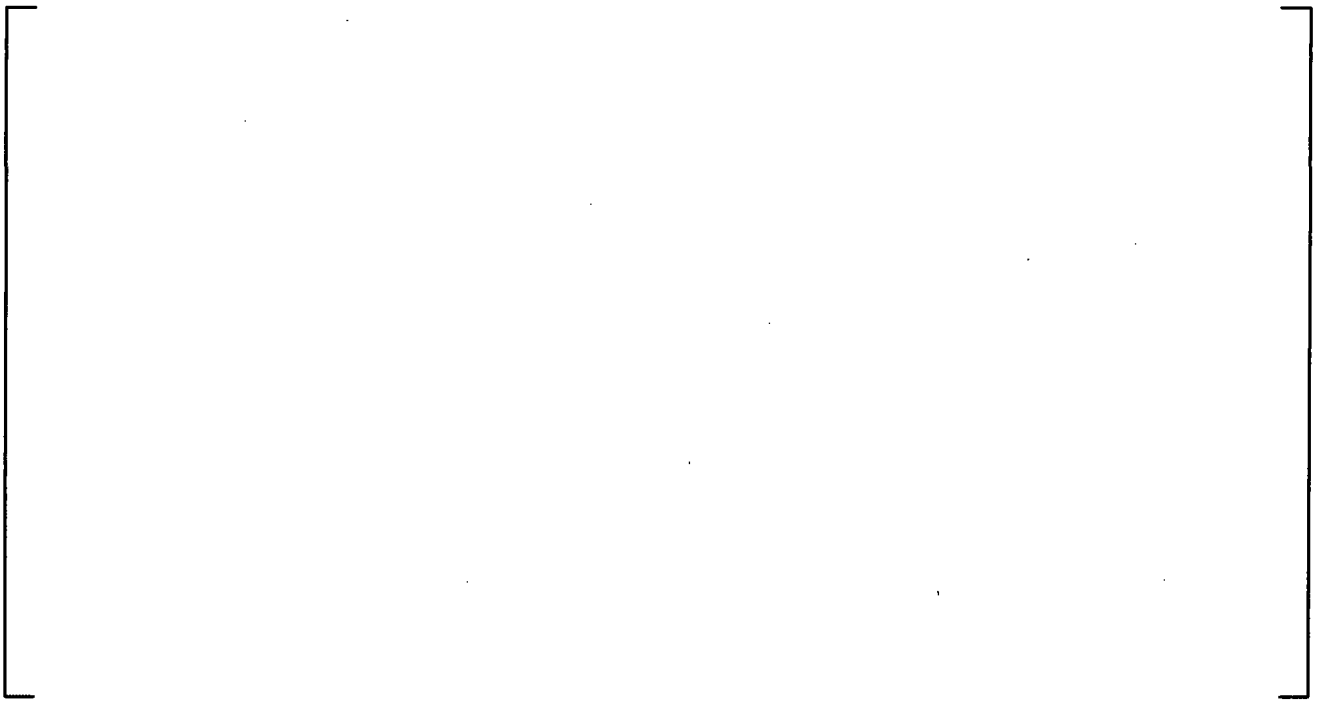

Figure 7-2 Flow-Time Profiles

a,b,c

Figure 7-3 Power Increase Transient – Power and Mass Flux as Function of Time – Experiment Number 1304 (Cosine Shape)

a,b,c

Figure 7-4 Power Increase Transient – Measured Temperature as Function of Time – Experiment Number 1304 (Cosine Shape)

a,b,c

Figure 7-5 Flow Reduction Transient – Power and Mass Flux as Function of Time – Experiment Number 1290 (Top-Peaked Shape)

a,b,c

Figure 7-6 Flow Reduction Transient (Slow) – Measured Temperature as Function of Time – Experiment Number 1290 (Top-Peaked Shape)

a,b,c

Figure 7-7 Combination Transient – Power and Mass Flux as Function of Time – Experiment Number 1226 (Top-Peaked Shape)

a,b,c

Figure 7-8 Combination Transient – Measured Temperature as Function of Time – Experiment Number 1226 (Top-Peaked Shape)

a,c

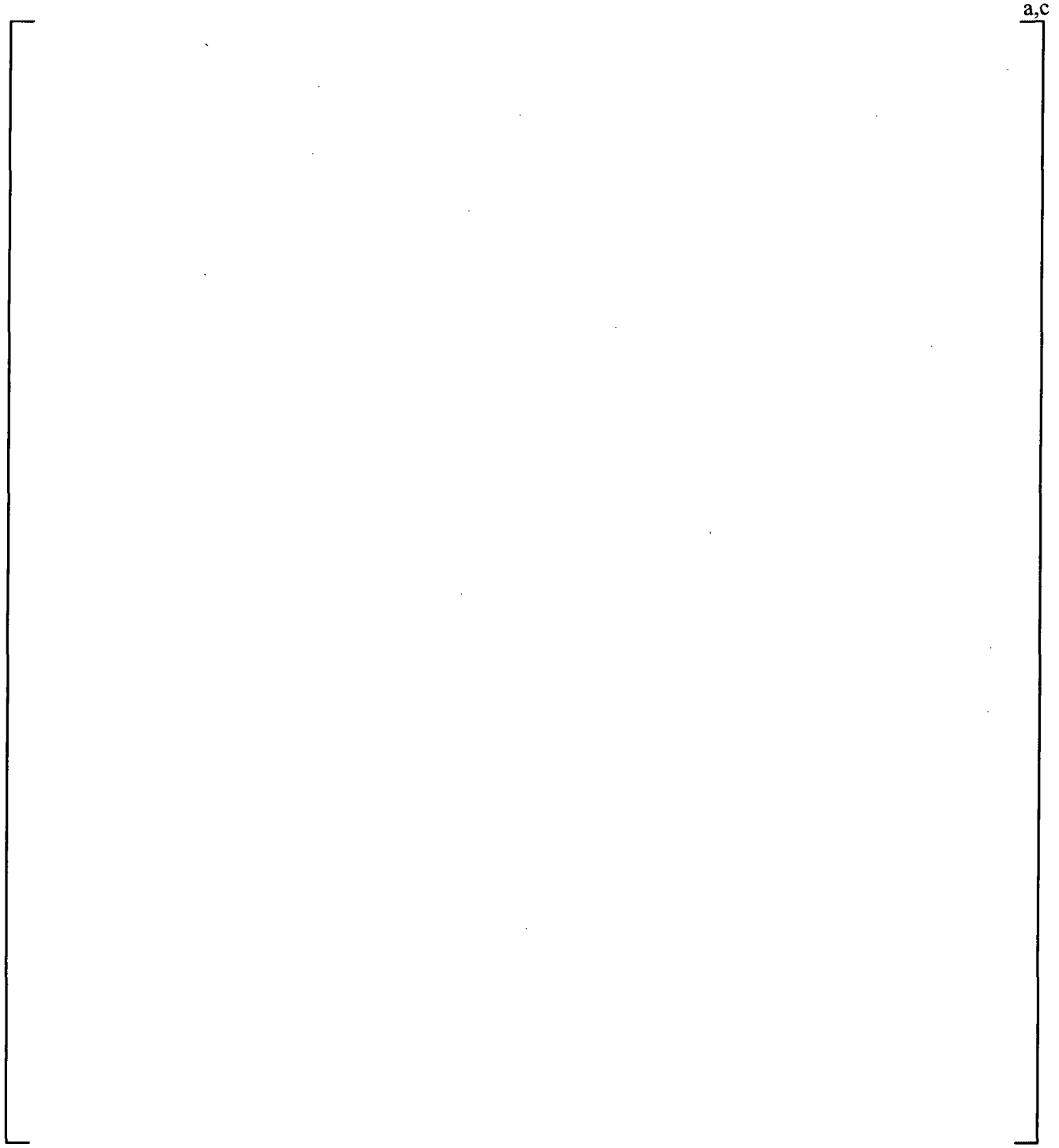

Figure 7-9 BISON-SLAVE Model for Test Heater Rod

a,b,c

Figure 7-10 Transient Validation for SF24XB – Bottom-Peaked Axial Power Shape

a,b,c

Figure 7-11 Transient Validation for SF24XC – Cosine Axial Power Shape

a,b,c

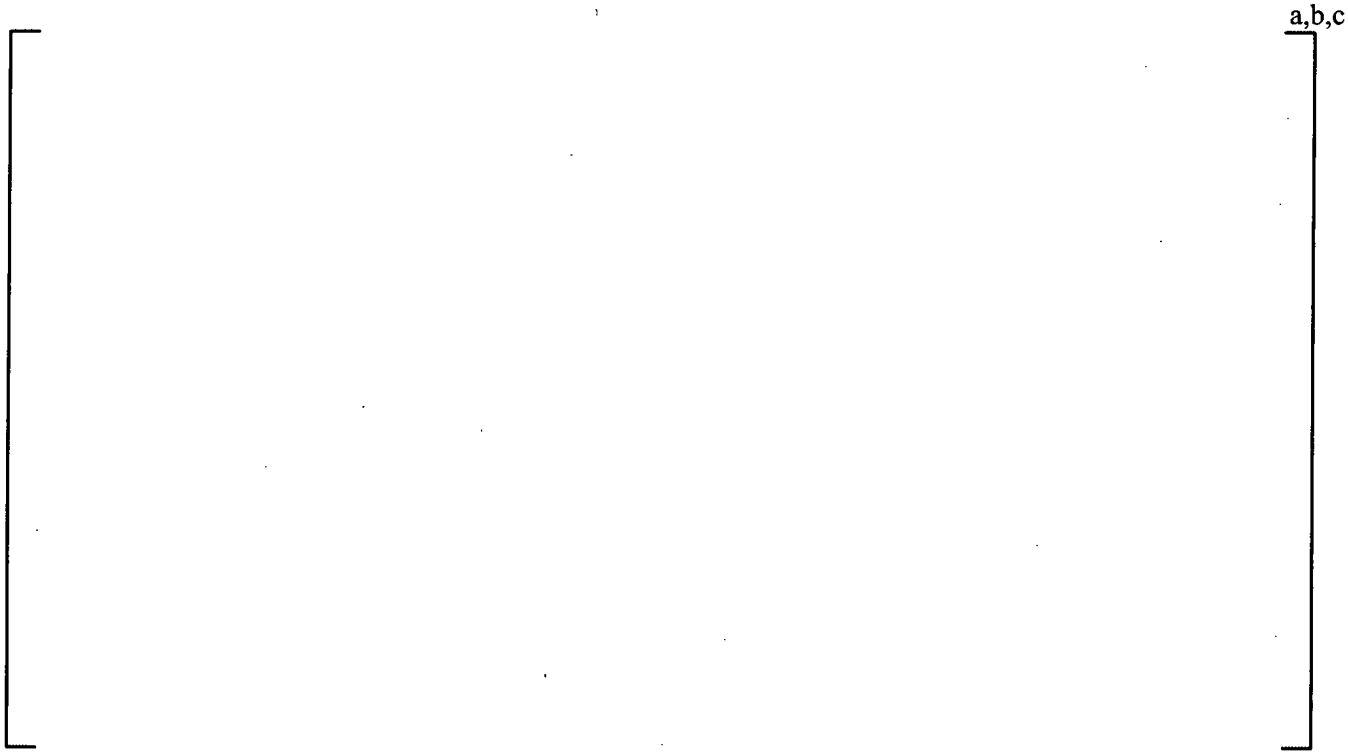

Figure 7-12 Transient Validation for SF24XT – Top-Peaked Axial Power Shape

a,b,c

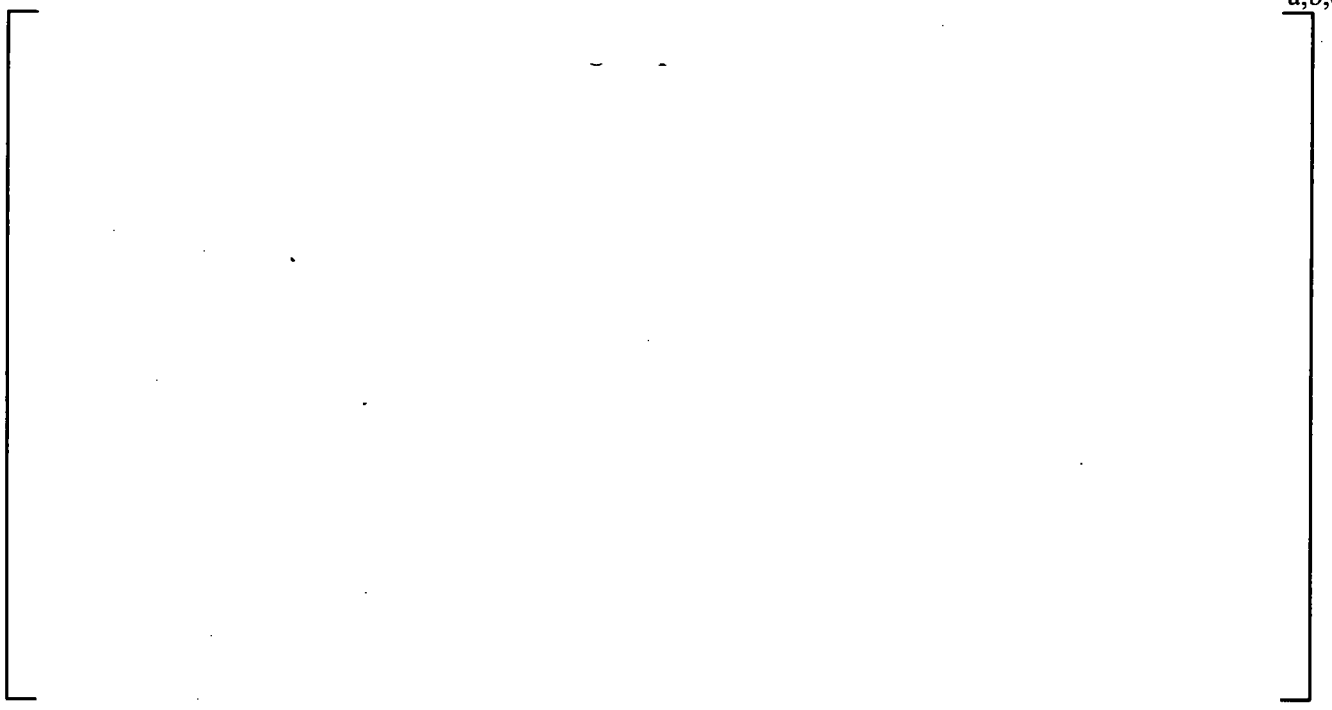

Figure 7-13 Predicted ΔT vs. Measured ΔT for SF24XB – Bottom-Peaked Axial Power Shape

a,b,c

Figure 7-14 Predicted ΔT vs. Measured ΔT for SF24XC – Cosine Axial Power Shape

a,b,c

Figure 7-15 Predicted ΔT vs. Measured ΔT for SF24XT – Top-Peaked Axial Power Shape

8 CONCLUSIONS

The critical power measurements described in this report provide an accurate simulation of the dryout performance of the SVEA-96 Optima3 fuel assembly. A total of [ ]^{a,c} 24-rod sub-bundle steady-state data points covering the entire range of expected reactor operating conditions were obtained. In addition, a total of [ ]^{a,c} 24-rod sub-bundle transient data points representative of BWR transients were obtained. The D5 critical power ratio correlation was developed based on [ ]^{a,c} of the 24-rod sub-bundle steady-state data points to correlate these critical power data. The correlation was developed to provide best-estimate predictions of steady-state and conservative predictions of transient critical power for a SVEA-96 Optima3 fuel assembly. The steady-state mean prediction error and standard deviation over the entire range of validity are [

]^{a,c}

Based on the critical power data for SVEA-96 Optima3 and the evaluations of the data presented in this report, the following conclusions can be drawn:

1. Sufficient data have been obtained and sufficient analysis has been performed to justify the use of the D5 CPR correlation and D5 dryout location predictor for design and licensing applications over the following input parameter ranges:

Parameter	Range of Validity

a,c

These ranges cover the operating conditions expected during typical BWR steady-state, transient, or accident conditions for which CPR calculations are required.

2. The D5 CPR correlation provides best-estimate prediction of the steady-state CPR for a single fuel rod or an entire sub-bundle of 24 fuel rods.

3. The D5 CPR correlation provides conservative prediction of CPR during transient conditions for the full 96-rod bundle.

4. Due to an elevated sensitivity observed for one of the 24 test rods during one of three test series (bottom-peaked power profile), the mean prediction error and standard deviation are [ ]^{a,c}, respectively, over the entire range of validity of the D5 CPR correlation. The negative bias in the mean prediction error will not be credited. Specifically, [ ]^{a,c} are appropriate to support the SLMCPR evaluations for SVEA-96 Optima3.

5. The correlation has been demonstrated to be capable of providing a conservative estimate of the onset of dryout during fast transients. The capability of the correlation to provide conservative estimates of the onset of dryout during fast transients is demonstrated for each transient system code application. An illustration of the Westinghouse methodology for confirming the capability of the correlation to conservatively treat transient applications is provided for the BISON-SLAVE code documented in References 3 and 4. It is demonstrated in this illustration that the correlation, in conjunction with the BISON-SLAVE code, is acceptable for the calculation of changes in CPR during transient events for design and licensing applications.

9 REFERENCES

1. Westinghouse Report CENPD-392-P-A (Proprietary), CENPD-392-A (Non-Proprietary), "10x10 SVEA Fuel Critical Power Experiments and CPR Correlations: SVEA-96," September 2000.

2. Westinghouse Report CENPD-389-P-A (Proprietary), CENPD-389-NP-A (Non-Proprietary), "10x10 SVEA Fuel Critical Power Experiments and CPR Correlations: SVEA-96+," September 1999.

3. Westinghouse Report RPA 90-90-P-A (Proprietary), RPA 90-90-NP-A (Non-Proprietary), "BISON – A One Dimensional Dynamic Analysis Code for Boiling Water Reactors," December 1991.

4. Westinghouse CENPD-292-P-A (Proprietary), CENPD-292-NP-A (Non-Proprietary), "BISON – One Dimensional Dynamic Analysis Code for Boiling Water Reactors: Supplement 1 to Code Description and Qualification," July 1996.

5. General Electric Report NEDO-10958, "General Electric BWR Thermal Analysis Basis (GETAB): Data, Correlation and Design Application," November 1973.

6. In Proceedings from Advances in Nuclear Fuel Management IV (ANFM 2009), Hilton Head Island, SC, USA, U.C. Bergmann, C. Adamsson and G. Norbäck, "Advanced dryout correlation and CPR methodology for Westinghouse SVEA-96 Optima3 fuel," April 12-15, 2009.

7. Westinghouse Report CENPD-390-P-A Rev. 0 (Proprietary), CENPD-390-A Rev. 0 (Non-Proprietary), "The Advanced PHOENIX and POLCA Codes for Nuclear Design of Boiling Water Reactors," December 2000.

8. Westinghouse Report WCAP-16081-P-A (Proprietary), WCAP-16081-NP-A (Non-Proprietary), "10x10 SVEA Fuel Critical Power Experiments and CPR Correlation: SVEA-96 Optima2," March 2005.

9. Nuclear Engineering and Design, 241, pp. 2843-2858, C. Adamsson and J.-M. Le Corre, "Modeling and validation of a mechanistic tool (MEFISTO) for the prediction of critical power in BWR fuel assemblies," 2011.

APPENDIX A
SVEA-96 OPTIMA3 STEADY STATE CRITCAL POWER TEST DATA
COSINE-PEAKED AXIAL POWER SHAPE

a,b,c

a,b,c

[

]

a,b,c

a,b,c

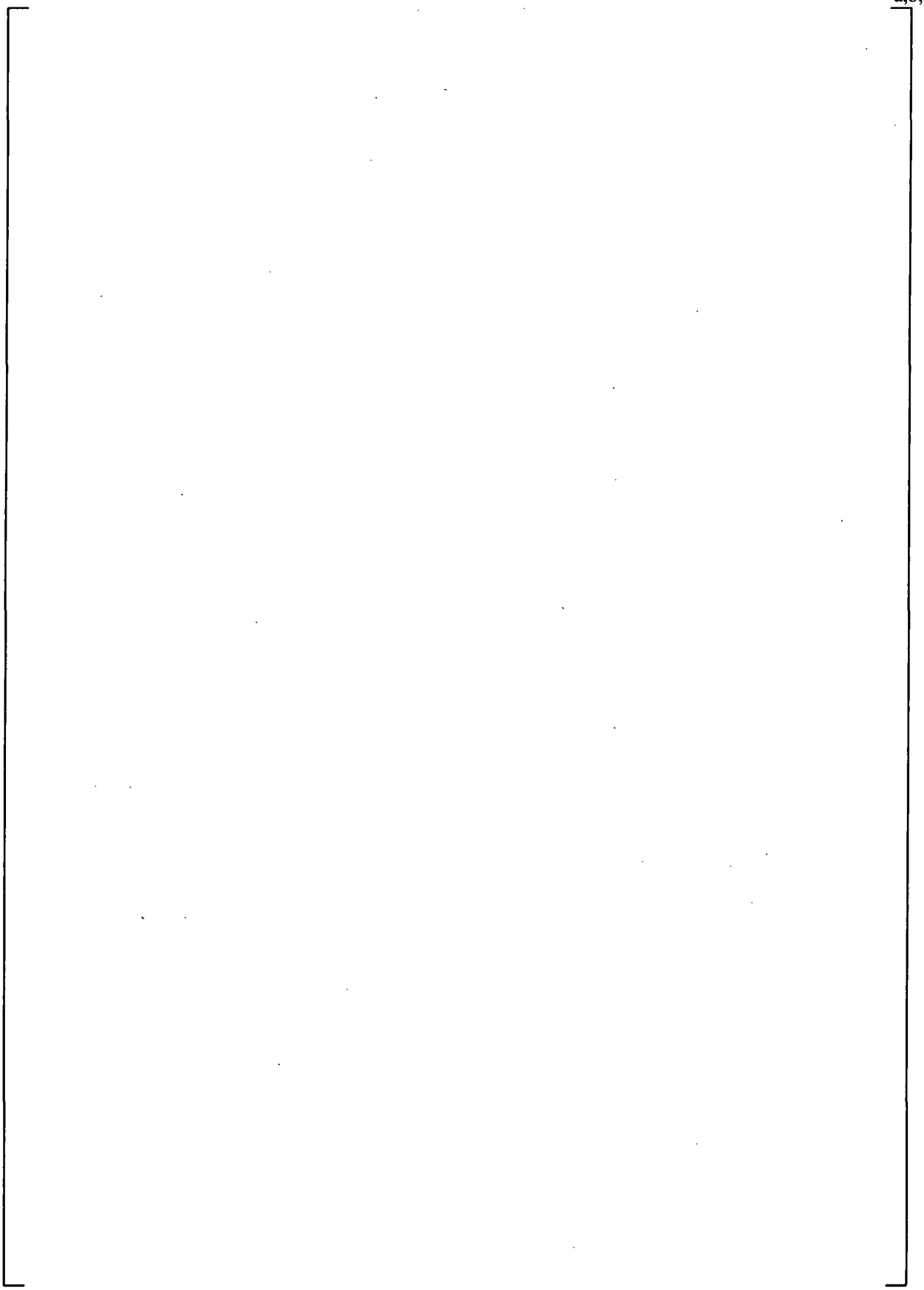

a,b,c

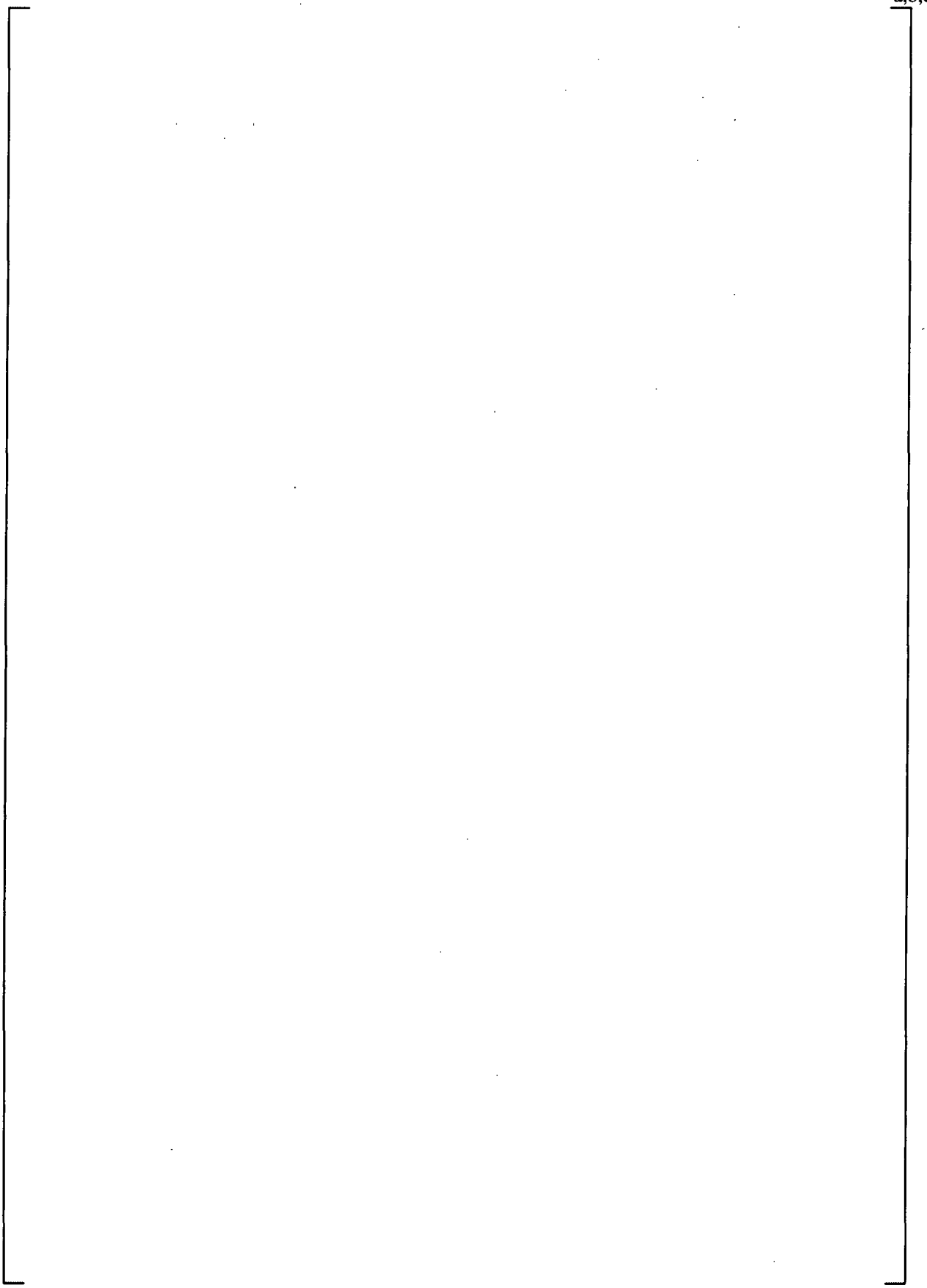

a,b,c

a,b,c

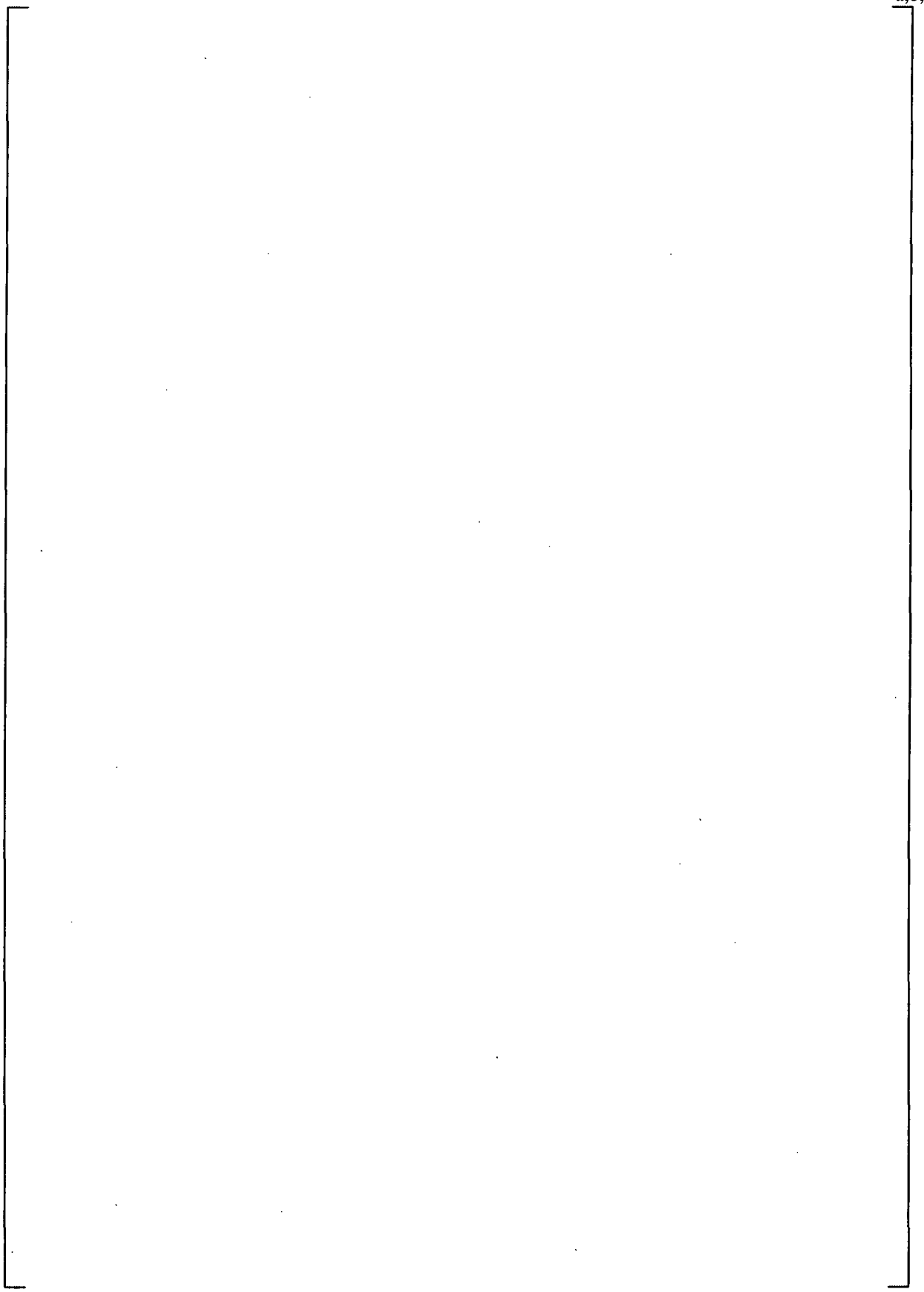

a,b,c

a,b,c

[

]

a,b,c

a,b,c

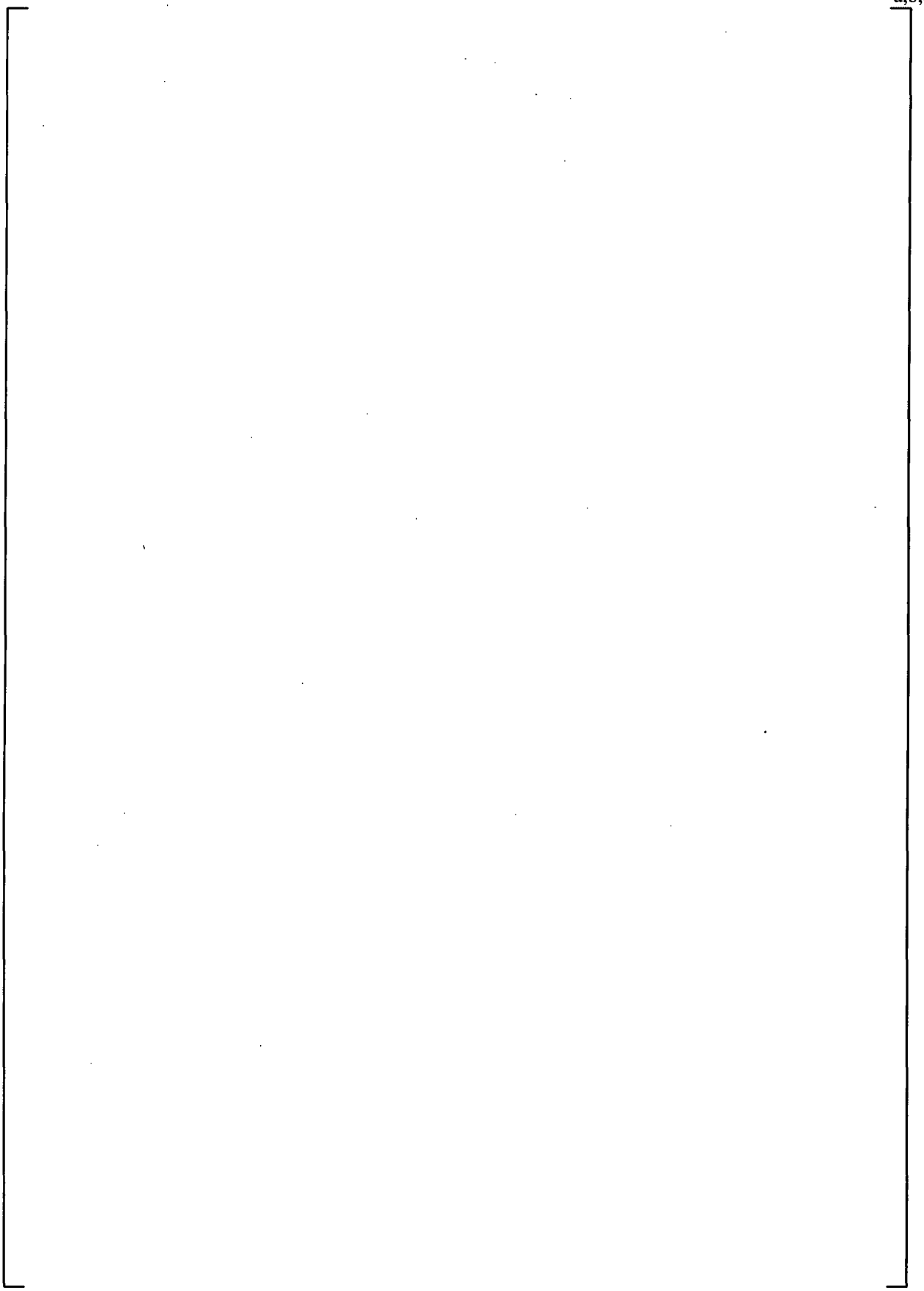

a,b,c

[

]

a,b,c

[

]

a,b,c

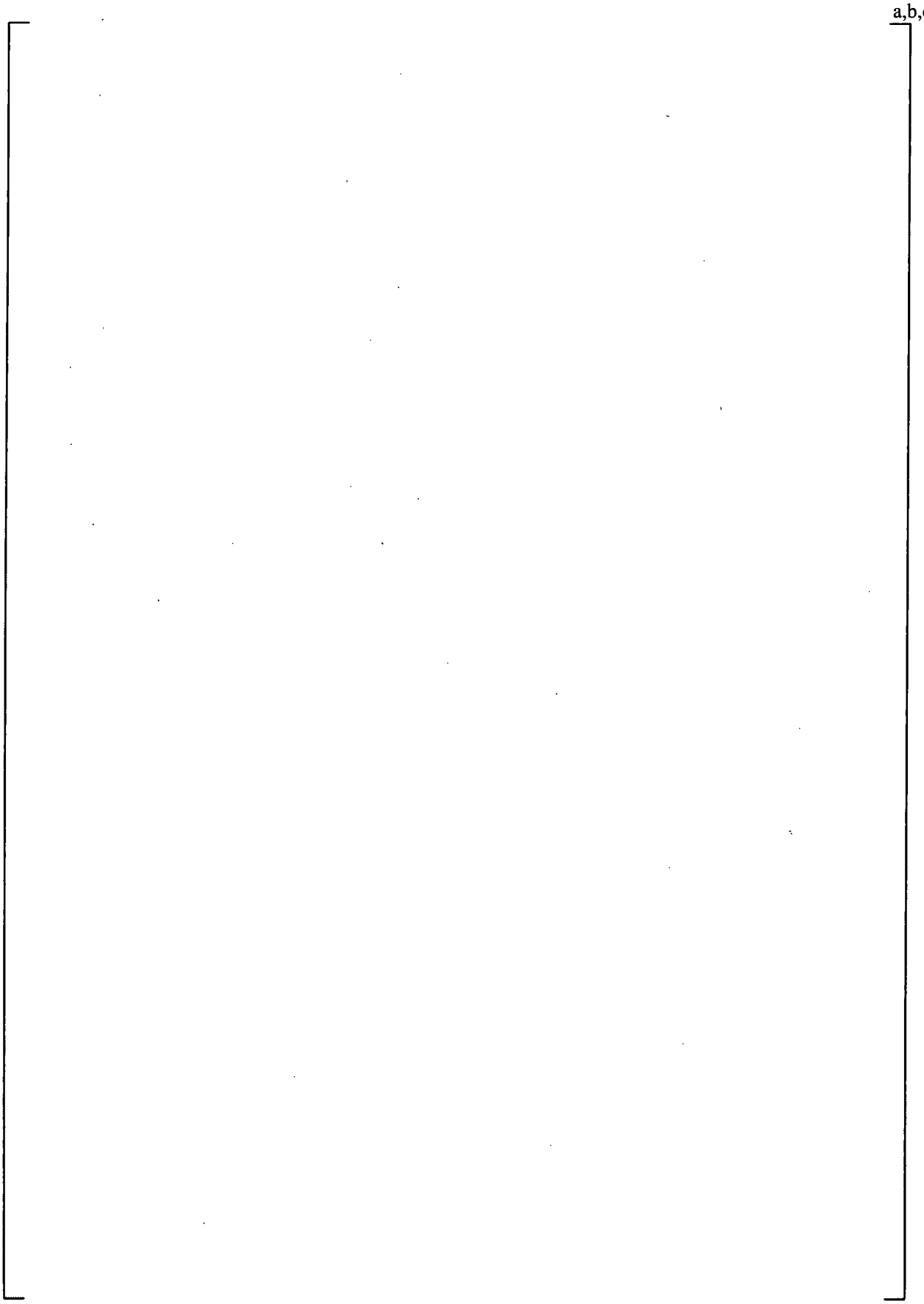

a,b,c

a,b,c

[

]

a,b,c

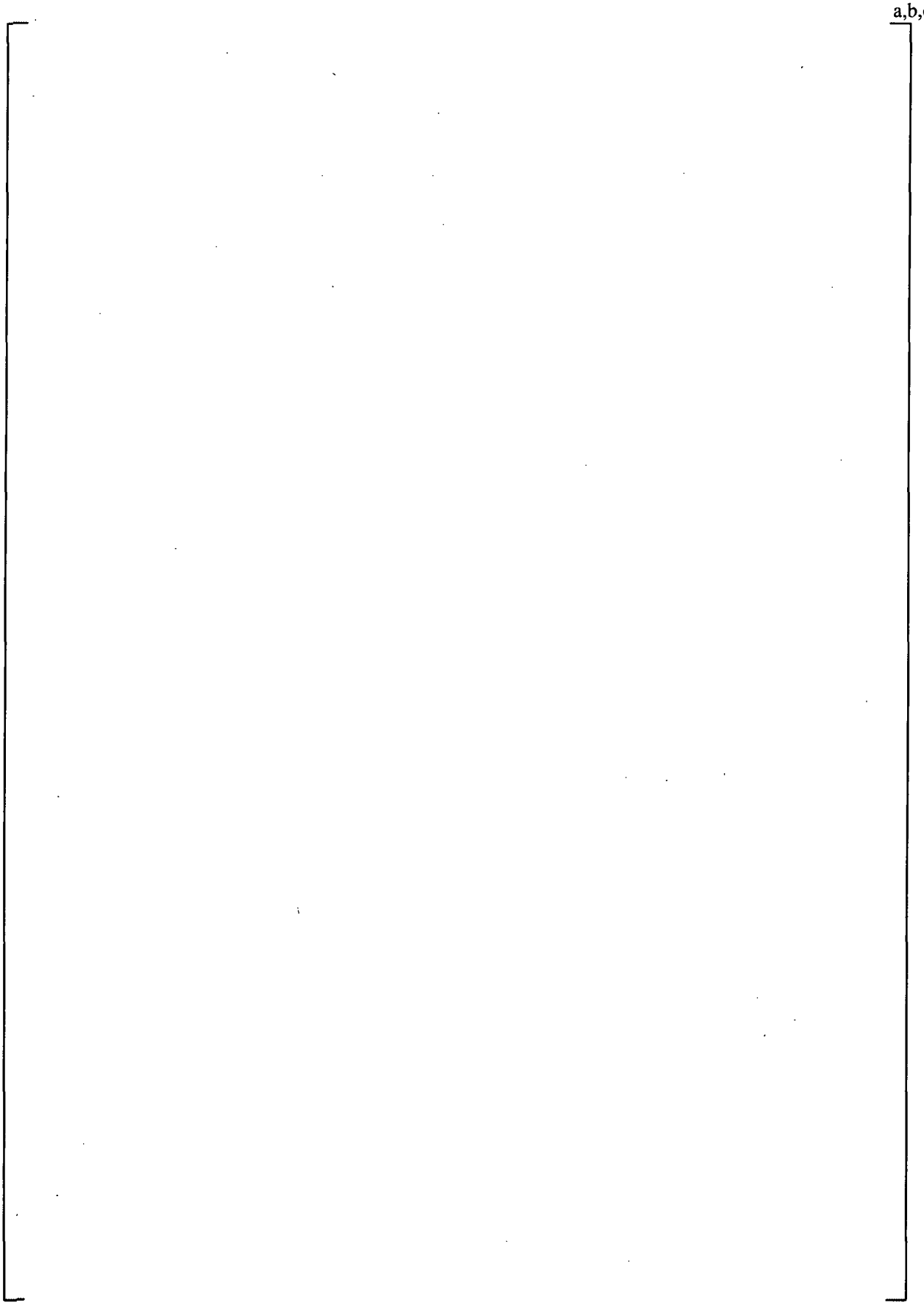

a,b,c

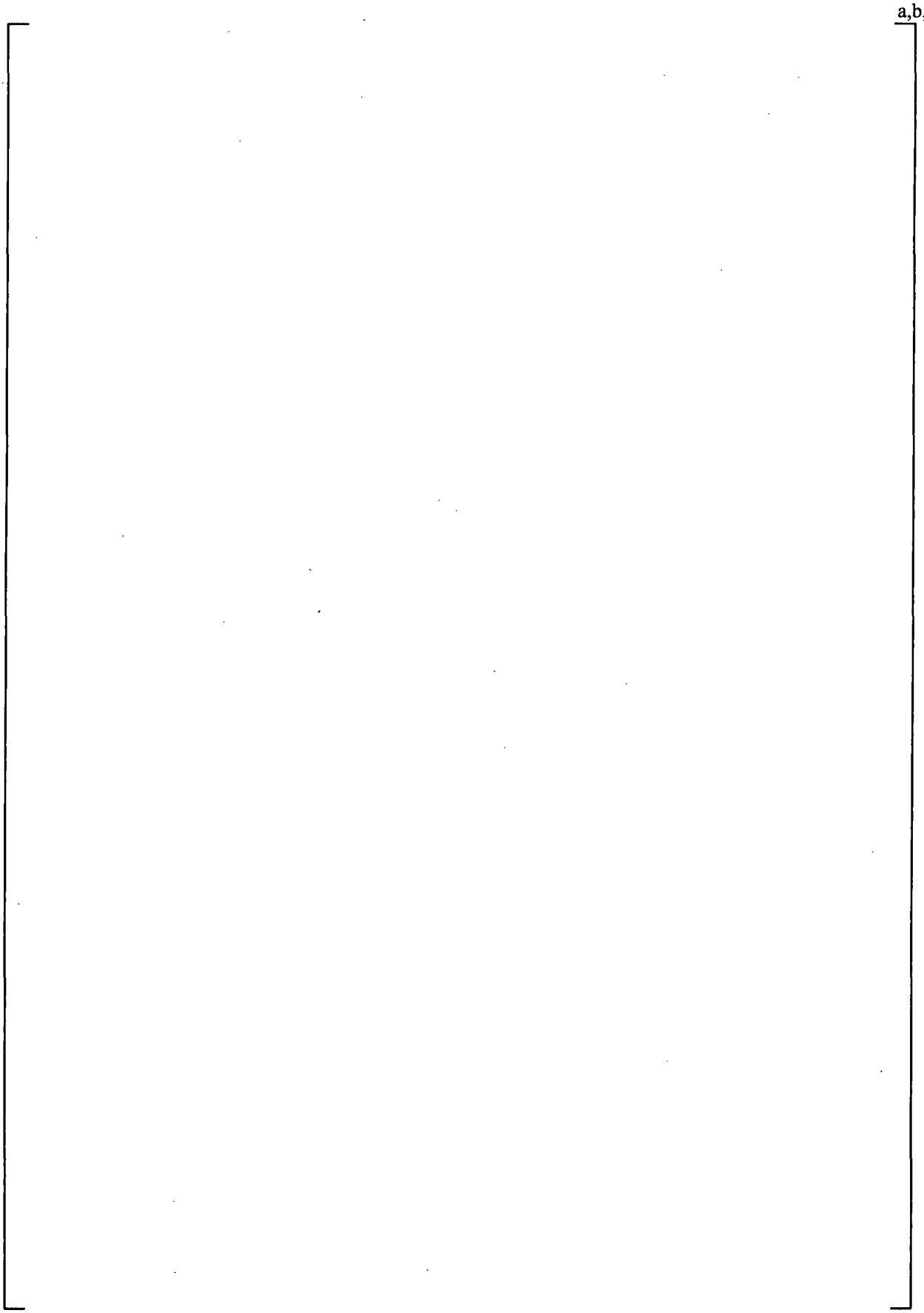

a,b,c

a,b,c

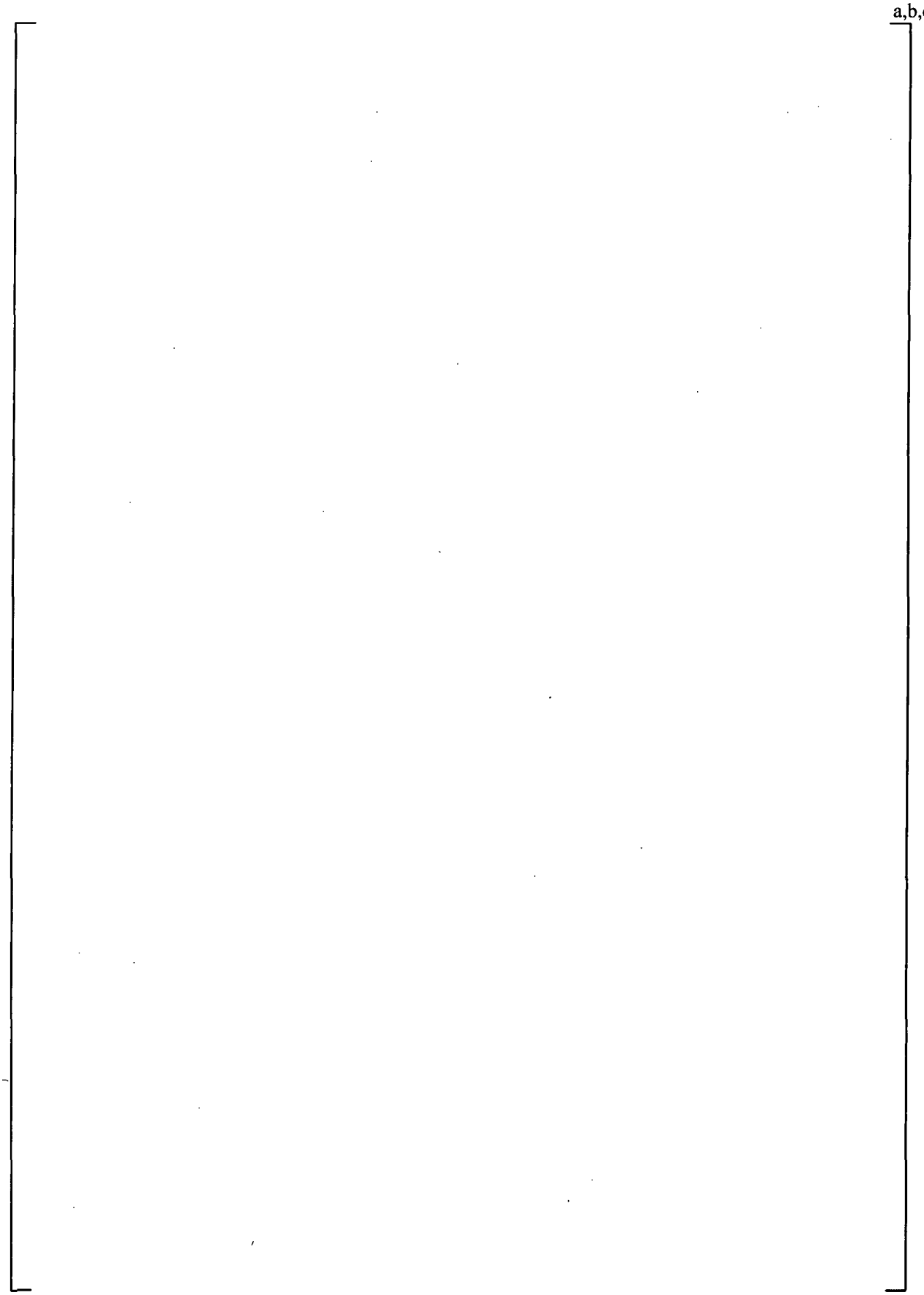

a,b,c

a,b,c

[

]

a,b,c

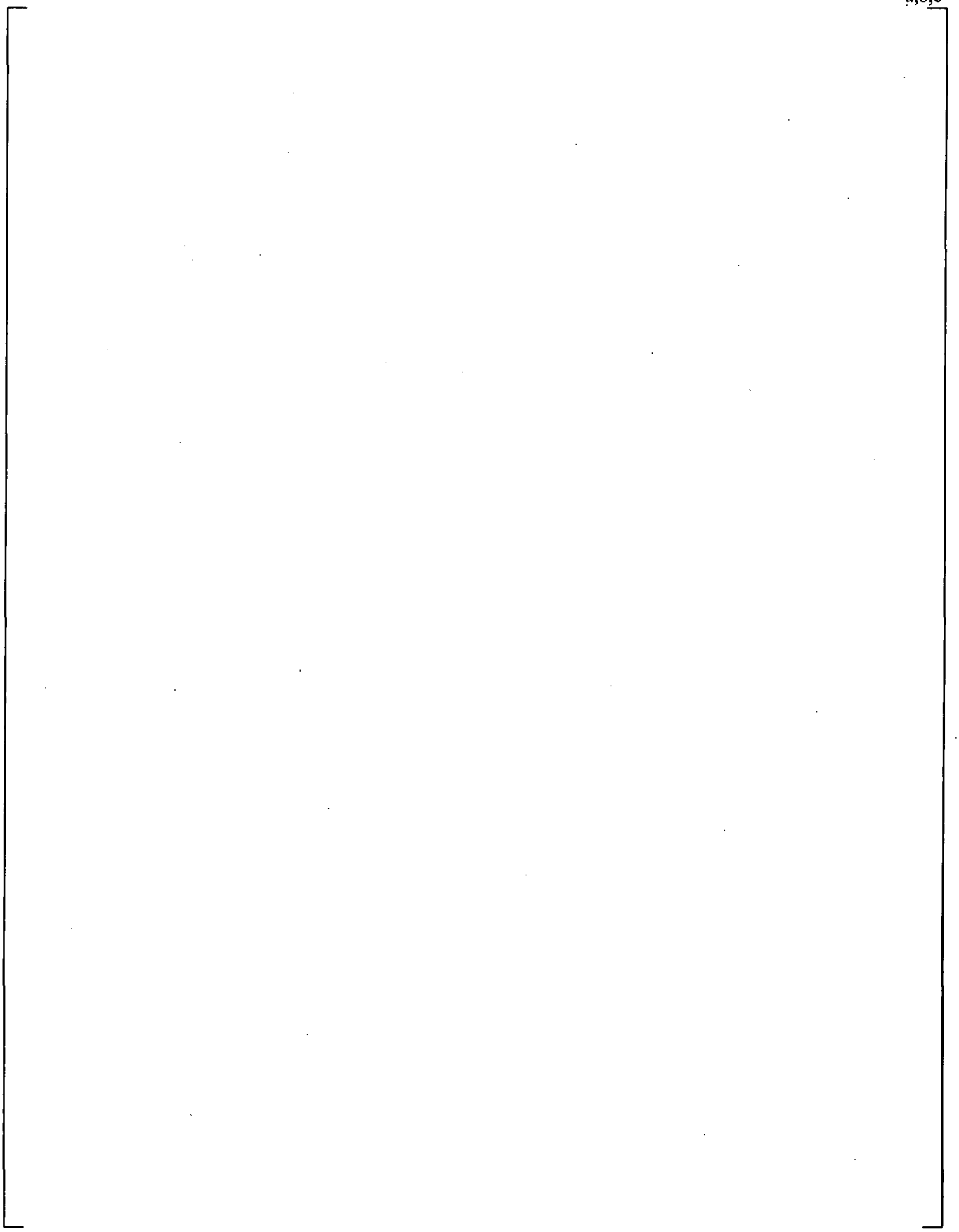

a,b,c

[

]

a,b,c

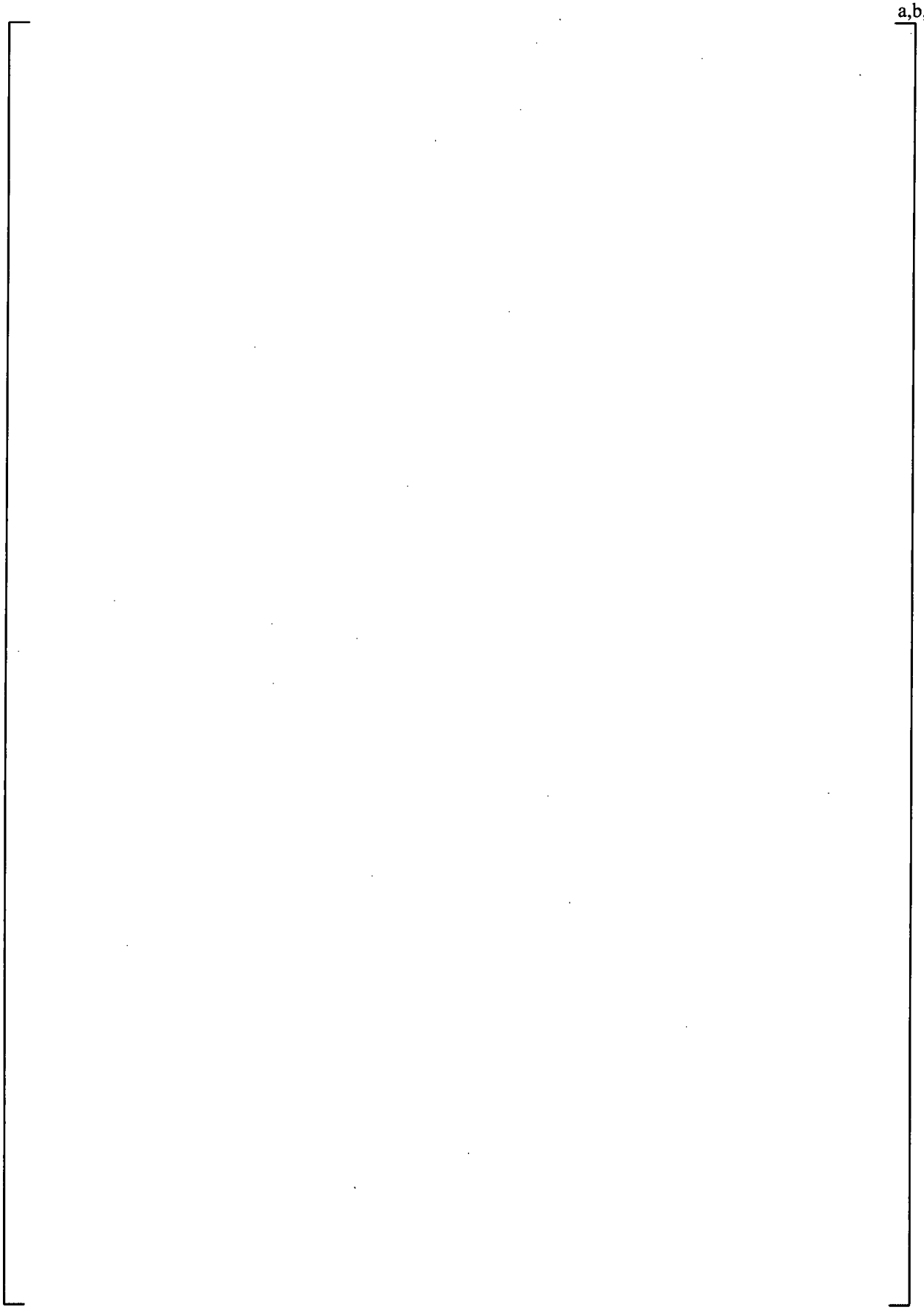

a,b,c

a,b,c

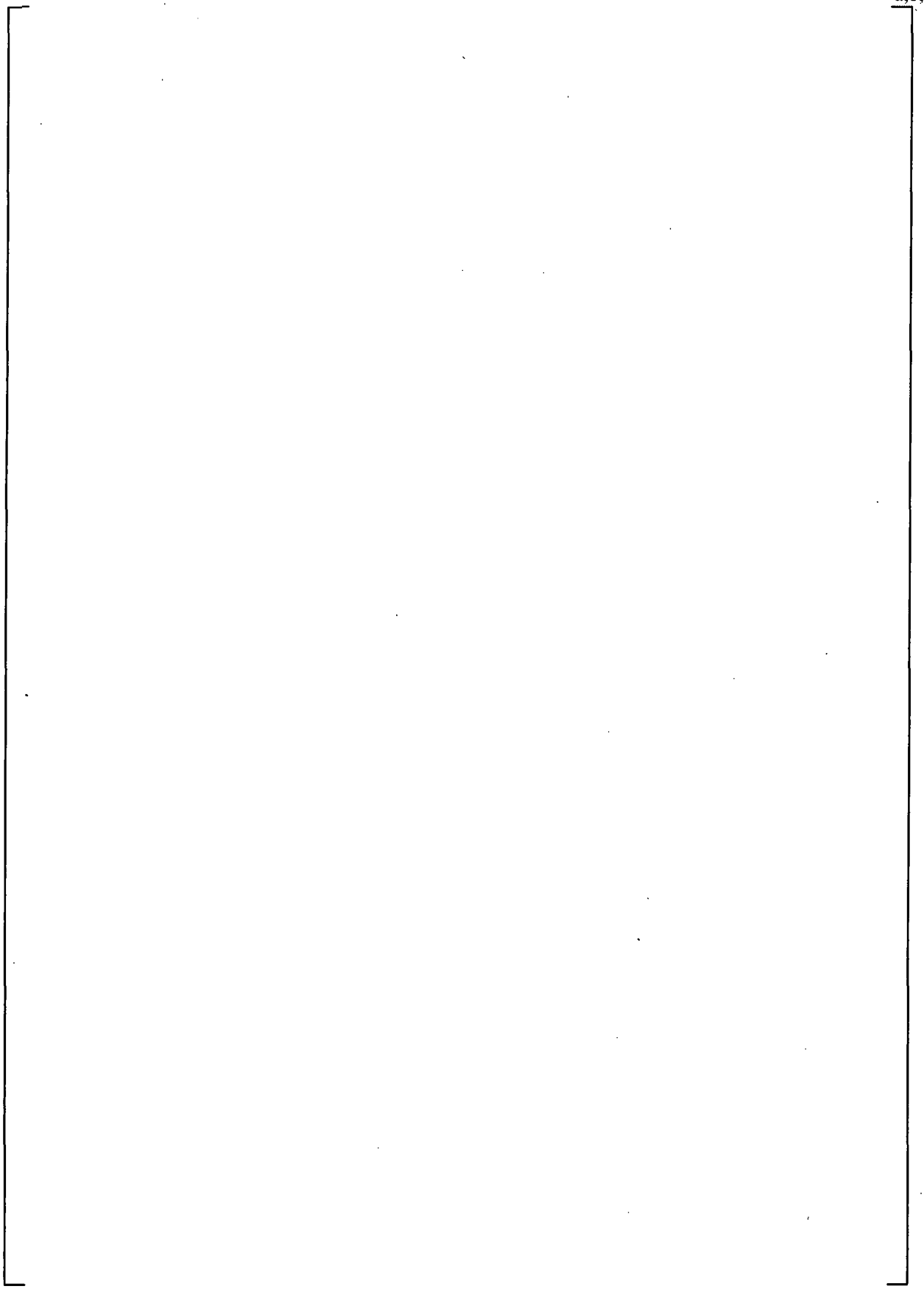

a,b,c

a,b,c

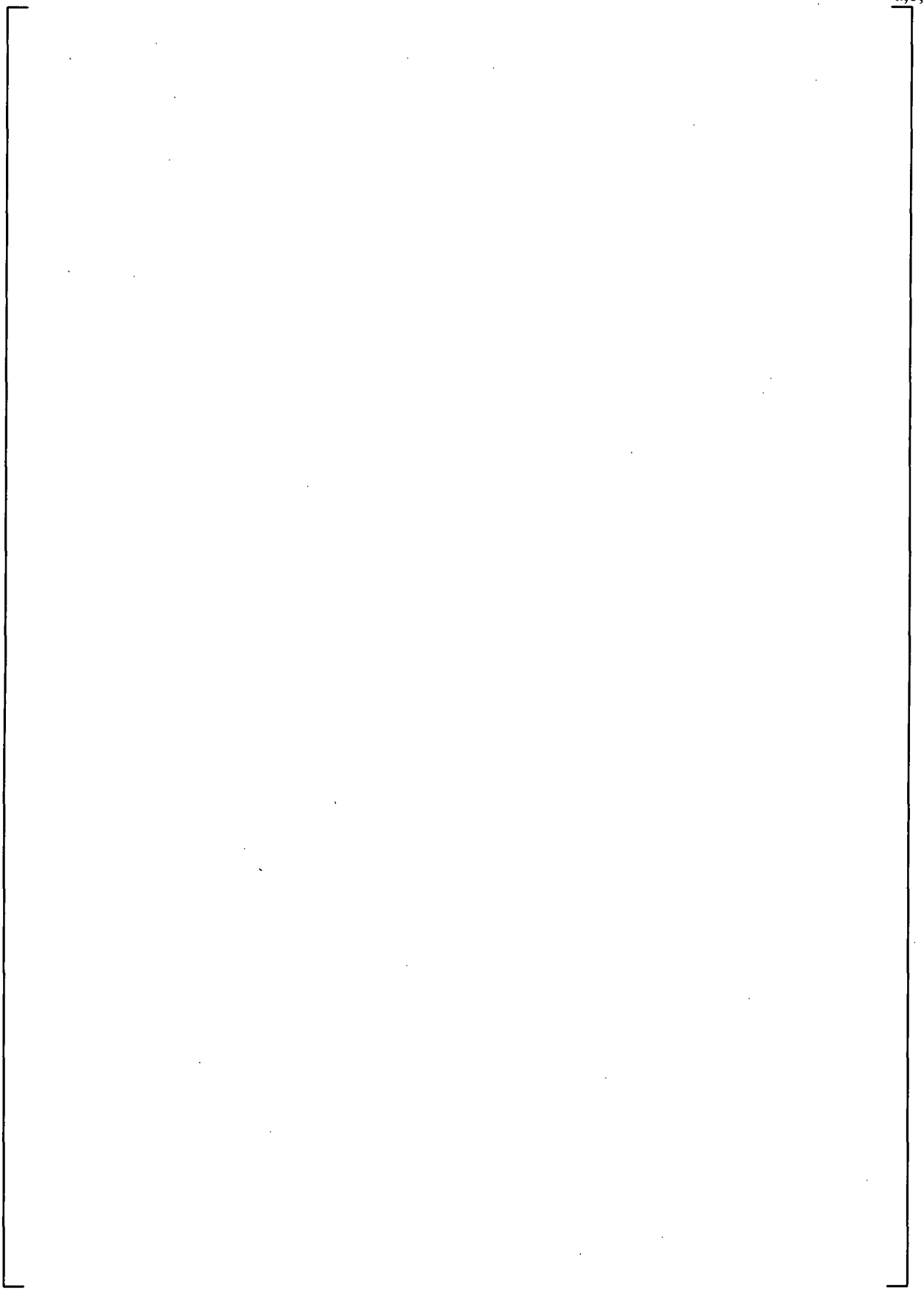

a,b,c

a,b,c

[

]

a,b,c

[

]

a,b,c

a,b,c

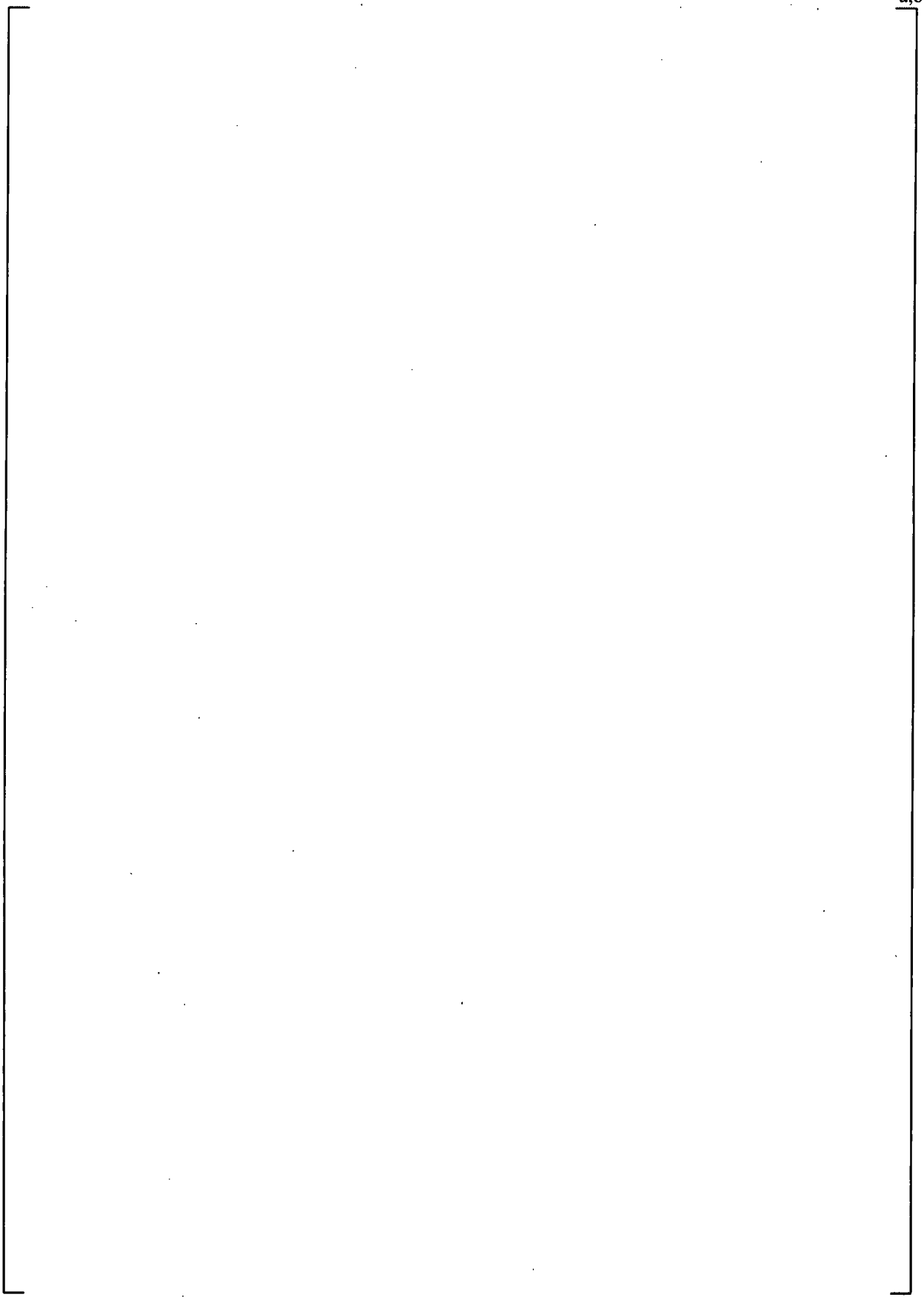

a,b,c

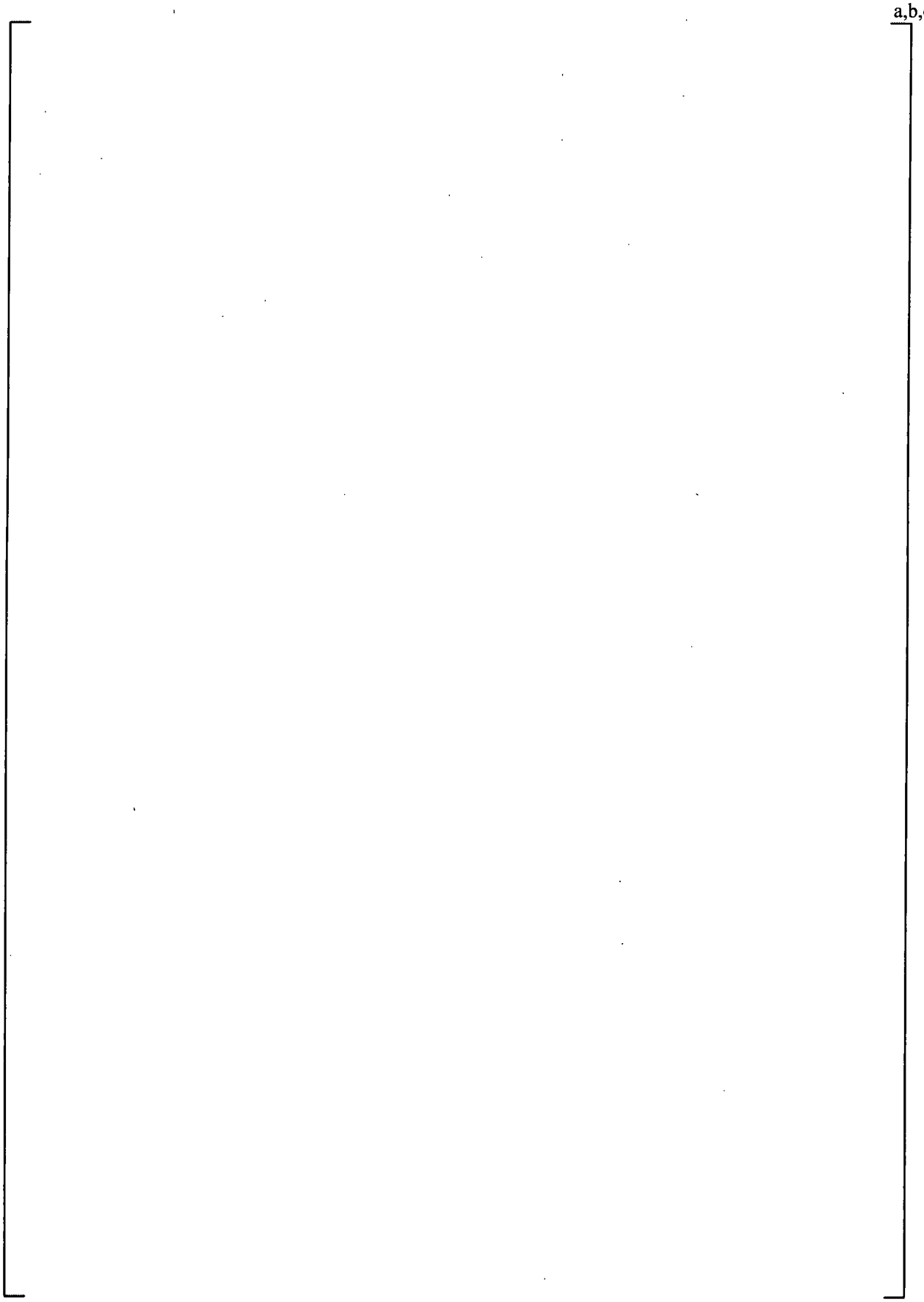

a,b,c

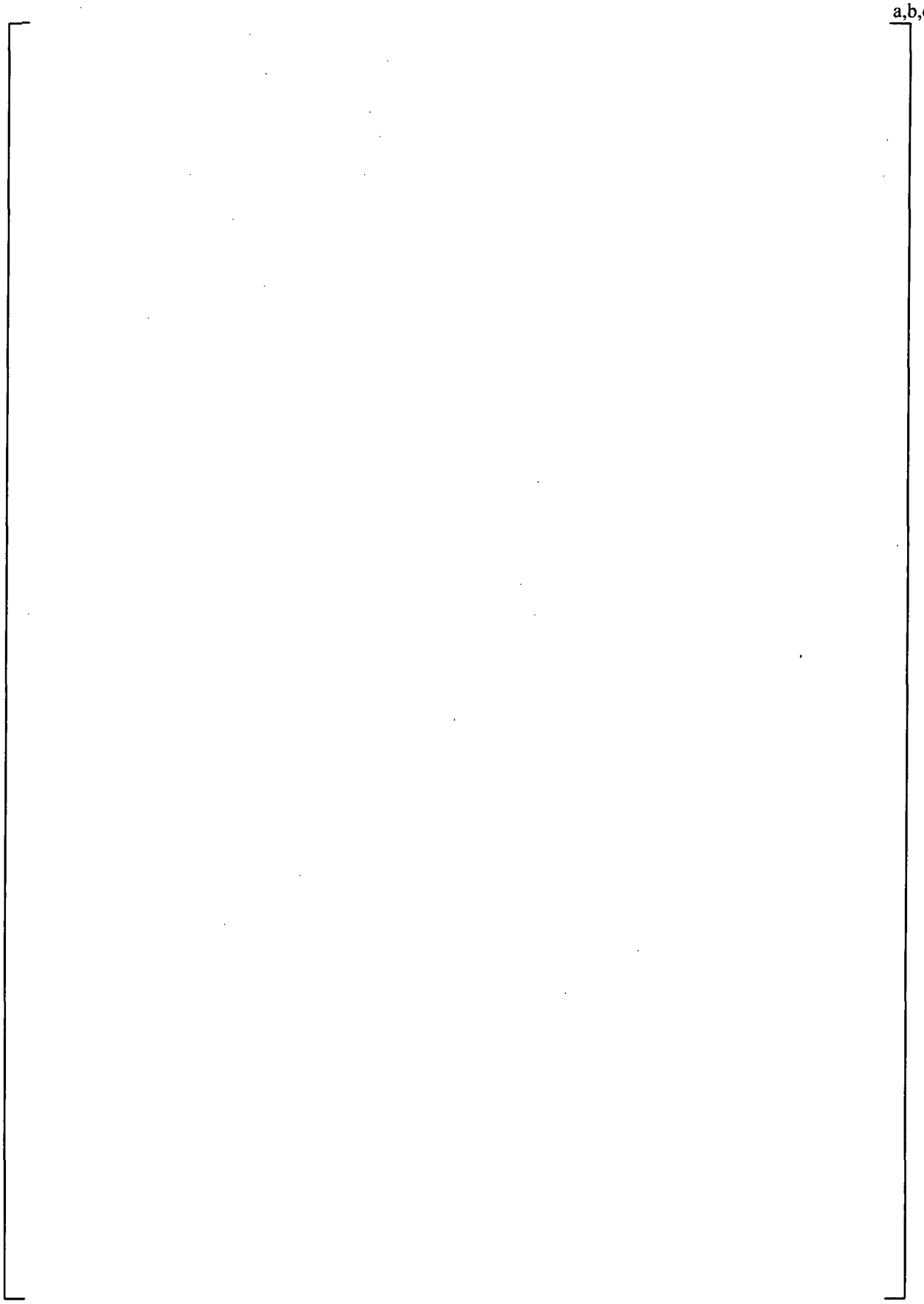

a,b,c

[

]

a,b,c

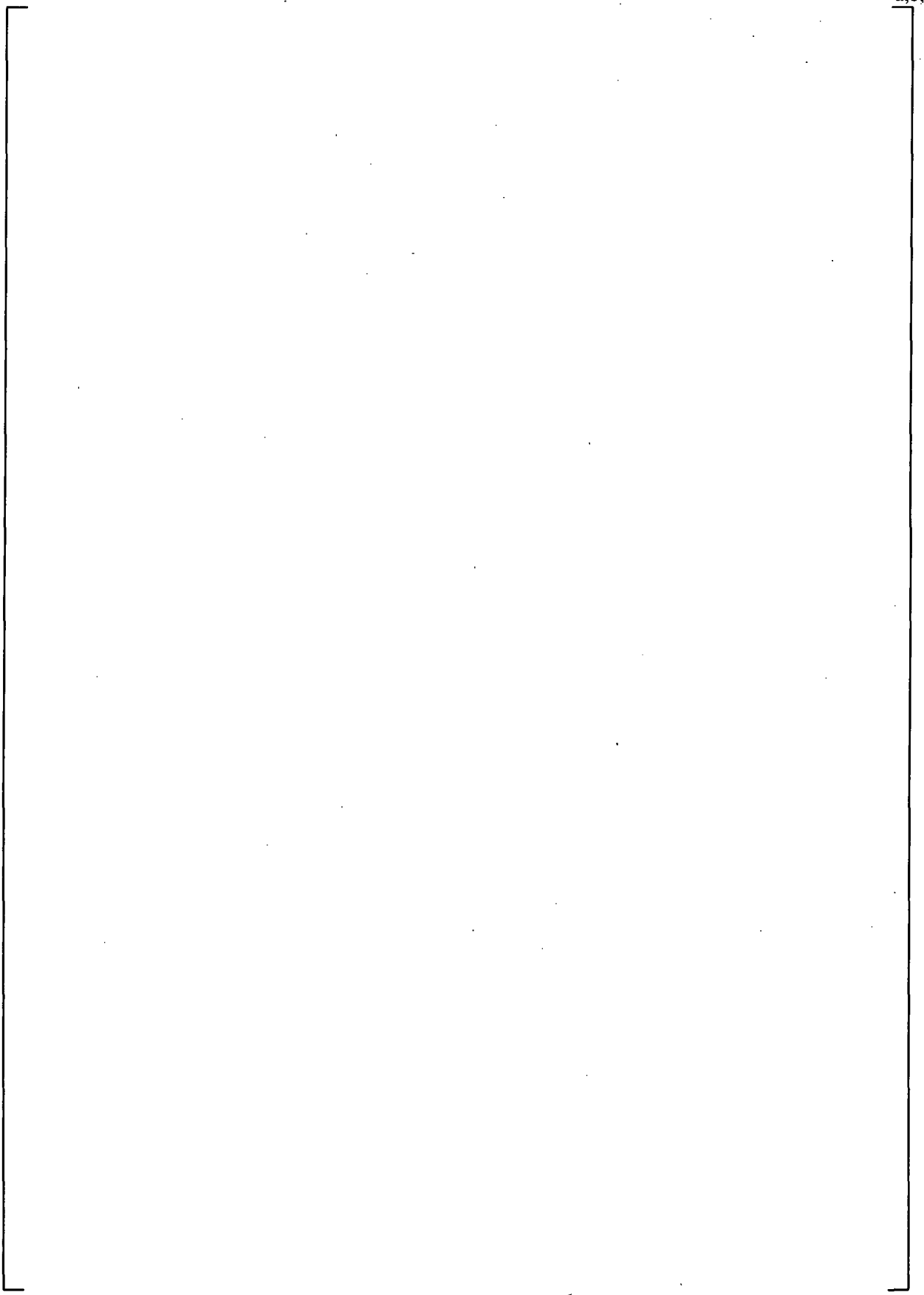

a,b,c

a,b,c

a,b,c

[

]

a,b,c

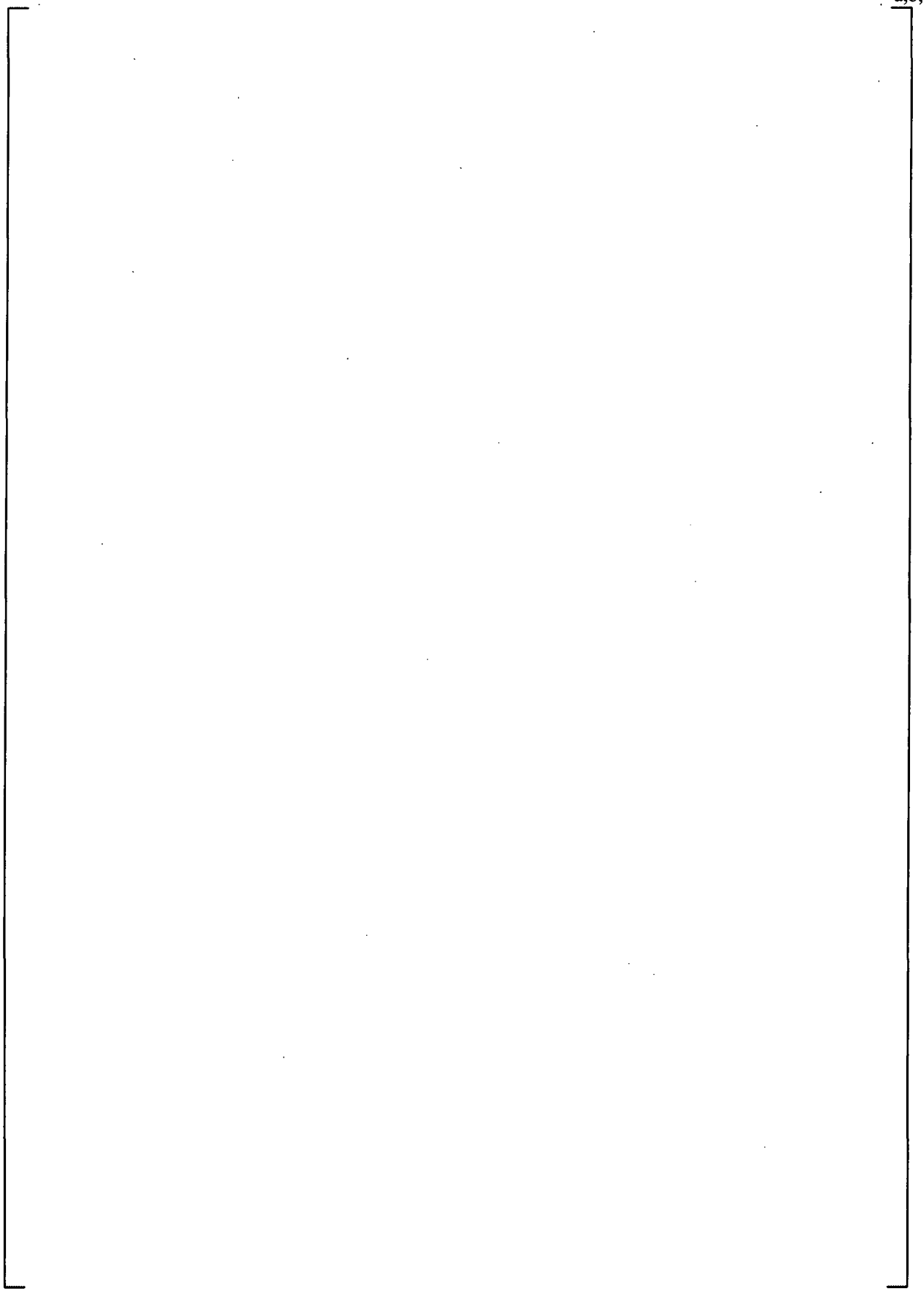

a,b,c

[

]

a,b,c

a,b,c

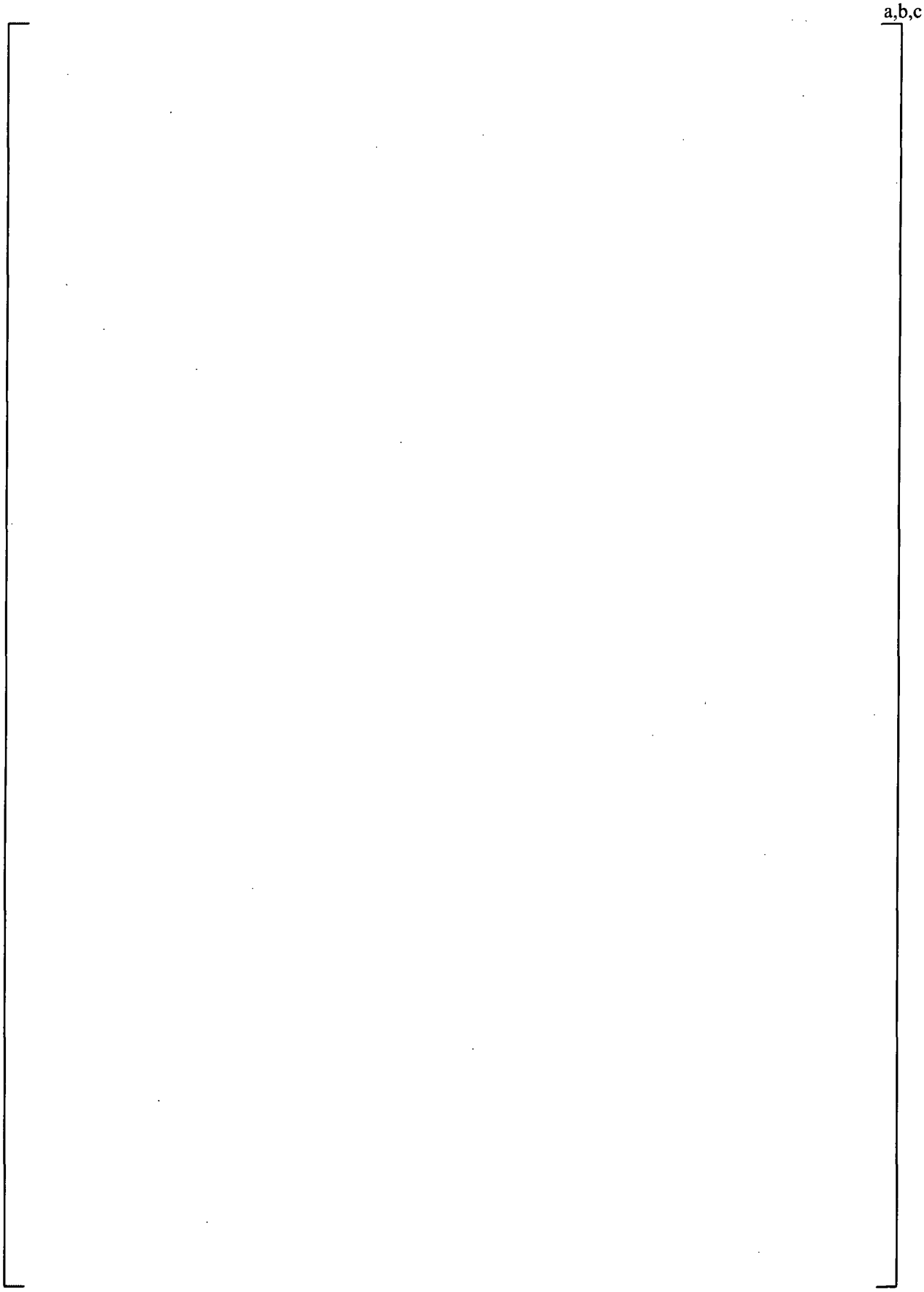

a,b,c

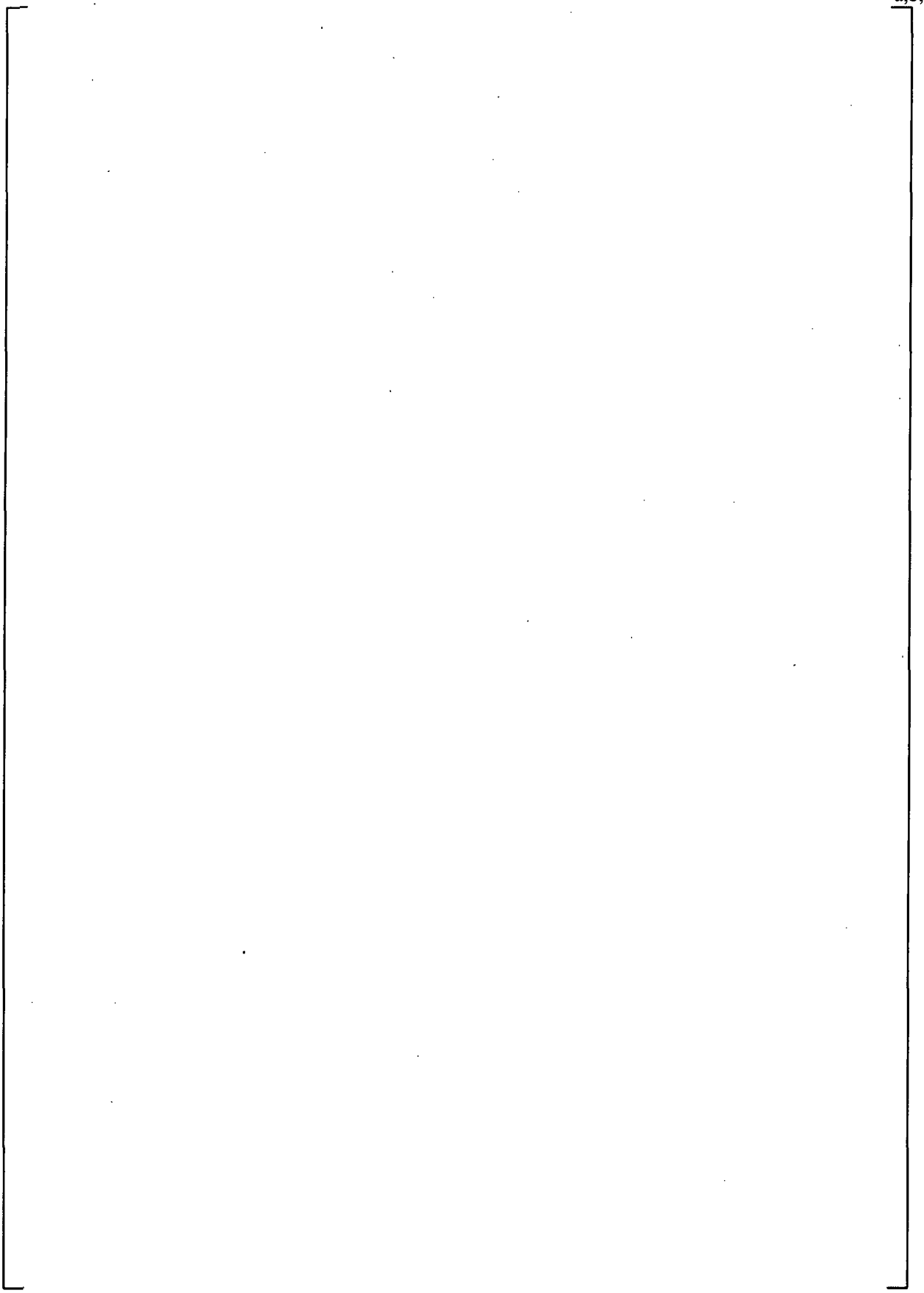

a,b,c

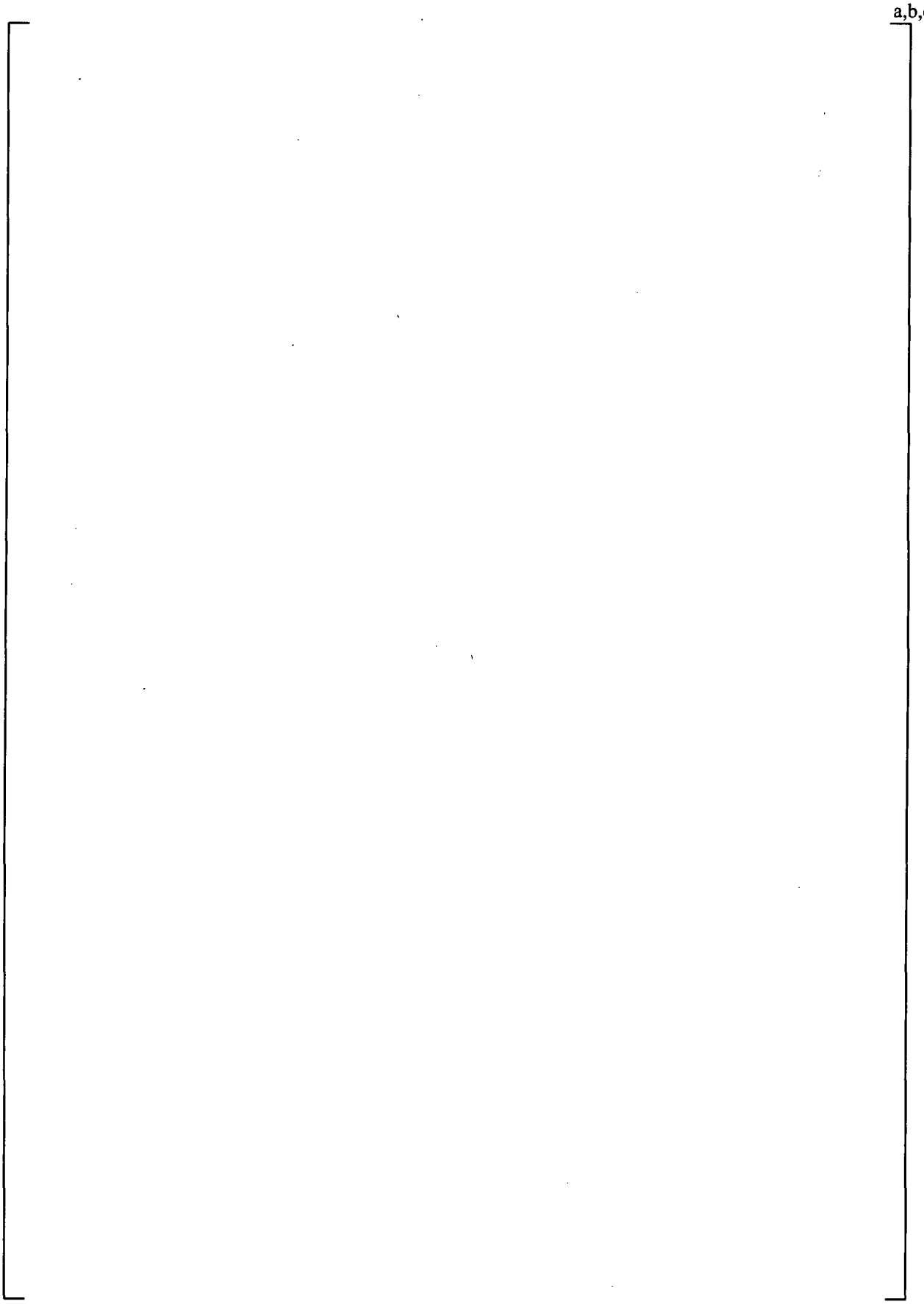

a,b,c

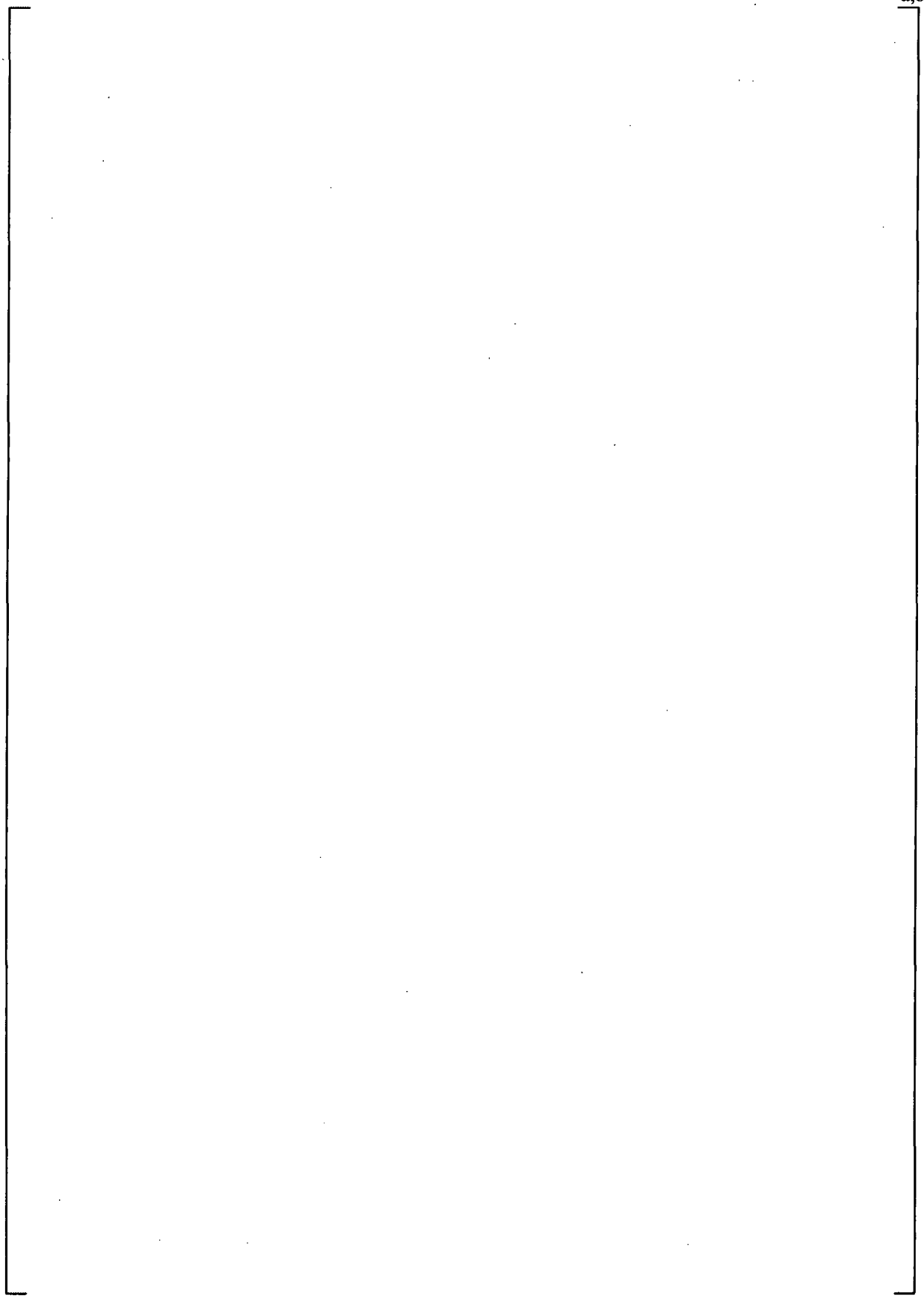

a,b,c

[

]

a,b,c

[

]

a,b,c

[

]

a,b,c

[

]

a,b,c

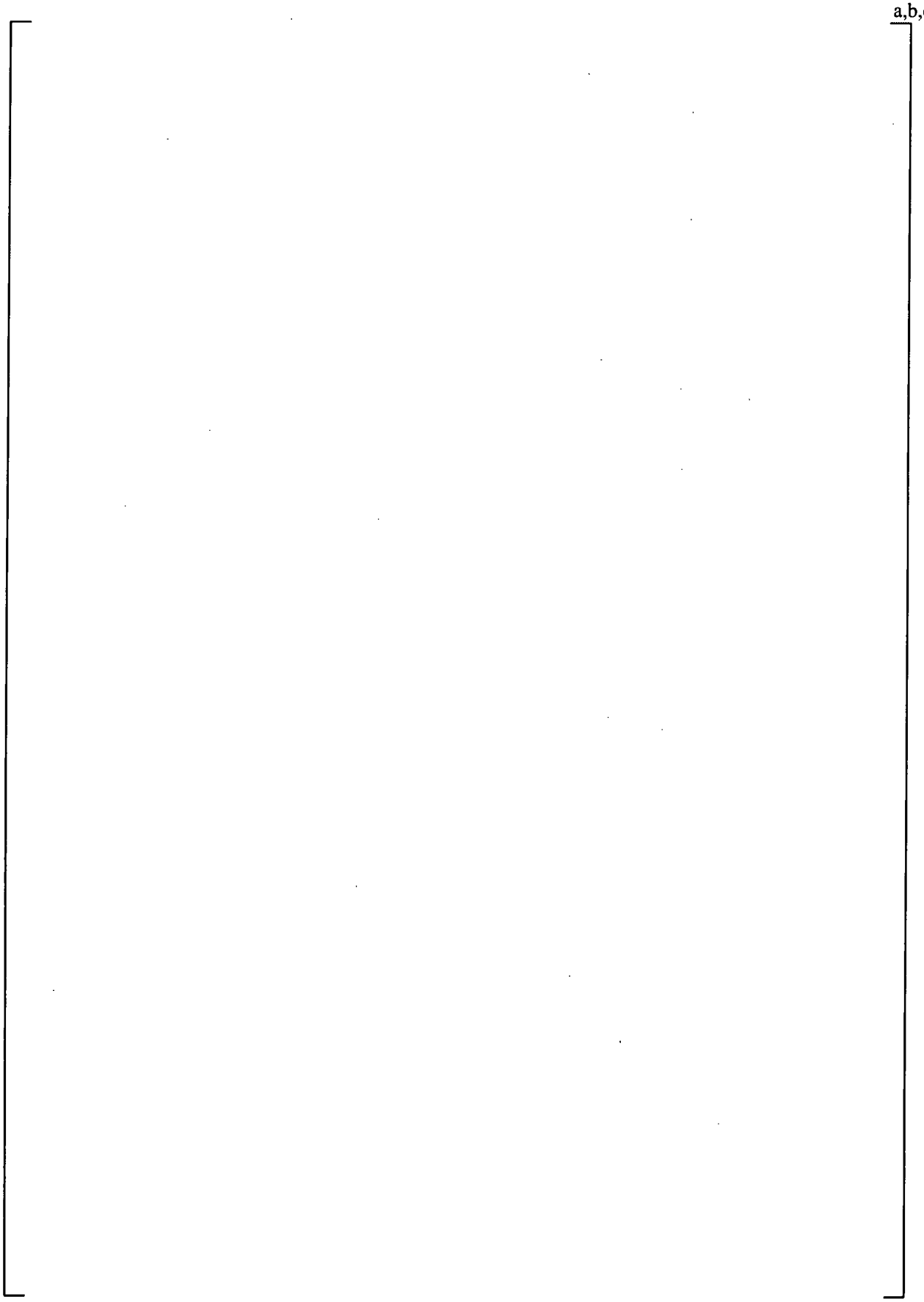

a,b,c

[

]

a,b,c

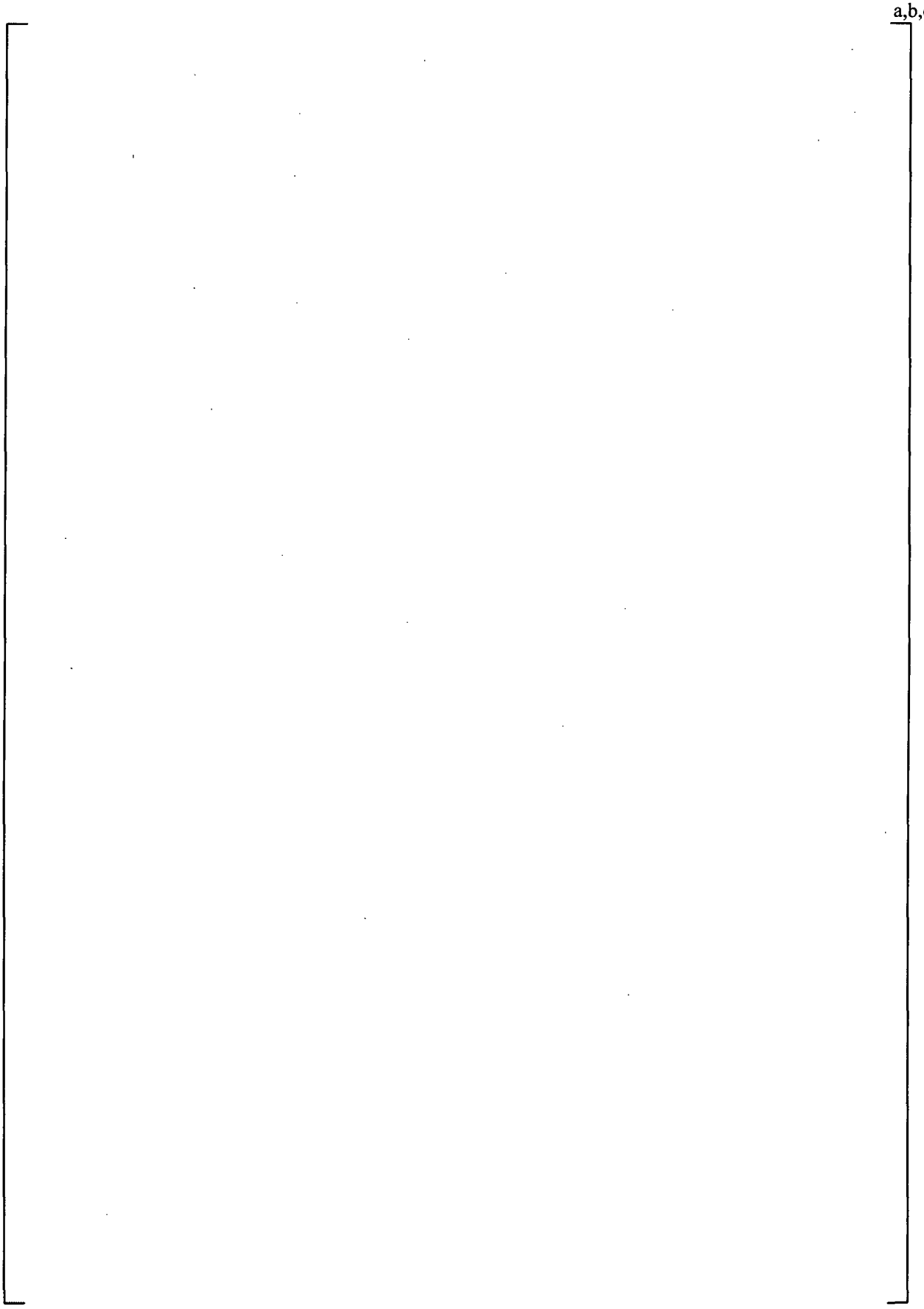

a,b,c

APPENDIX B
SVEA-96 OPTIMA3 STEADY STATE CRITICAL POWER TEST DATA BOTTOM-PEAKED AXIAL POWER SHAPE

a,b,c

a,b,c

a,b,c

[

]

a,b,c

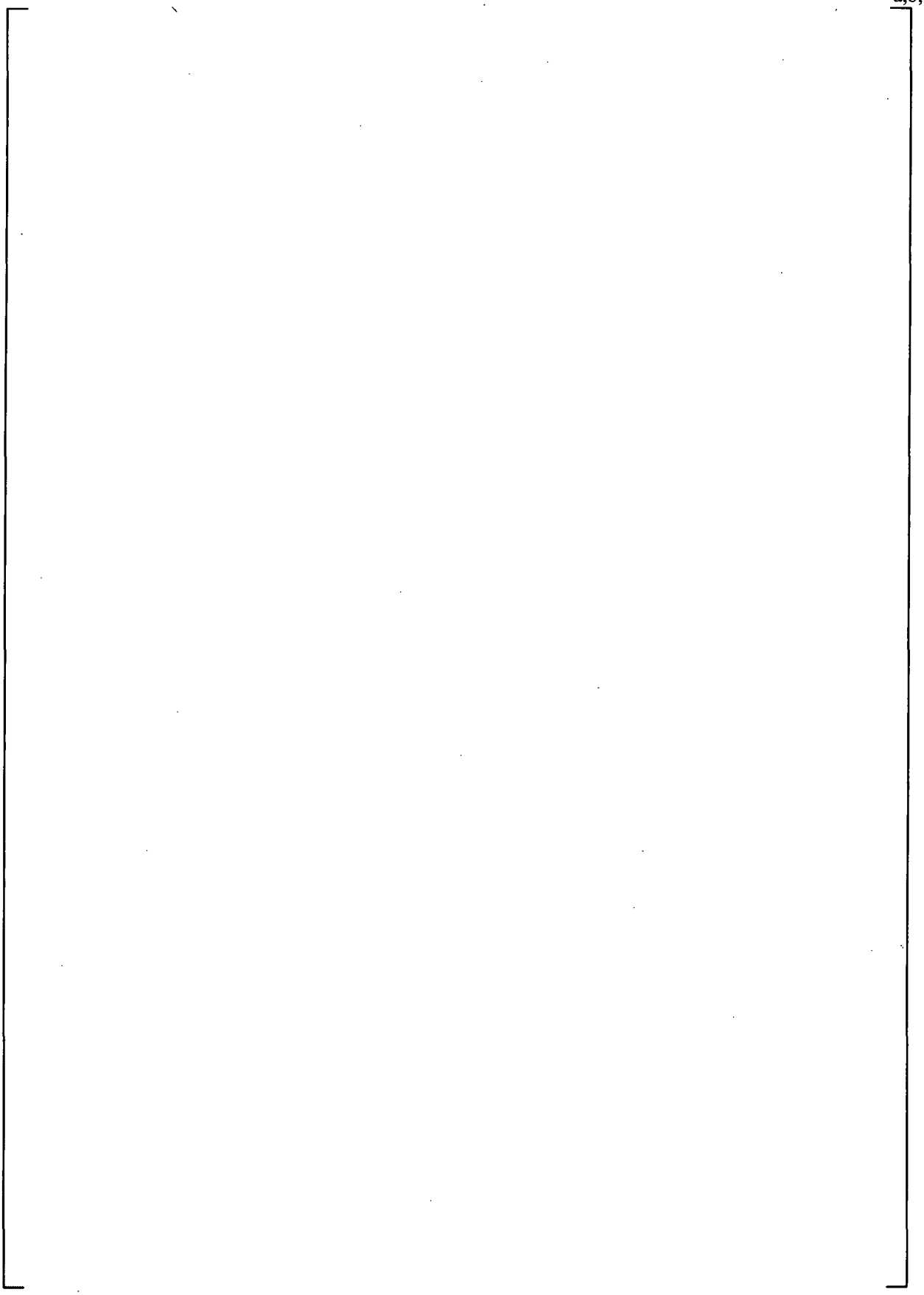

a,b,c

[

]

a,b,c

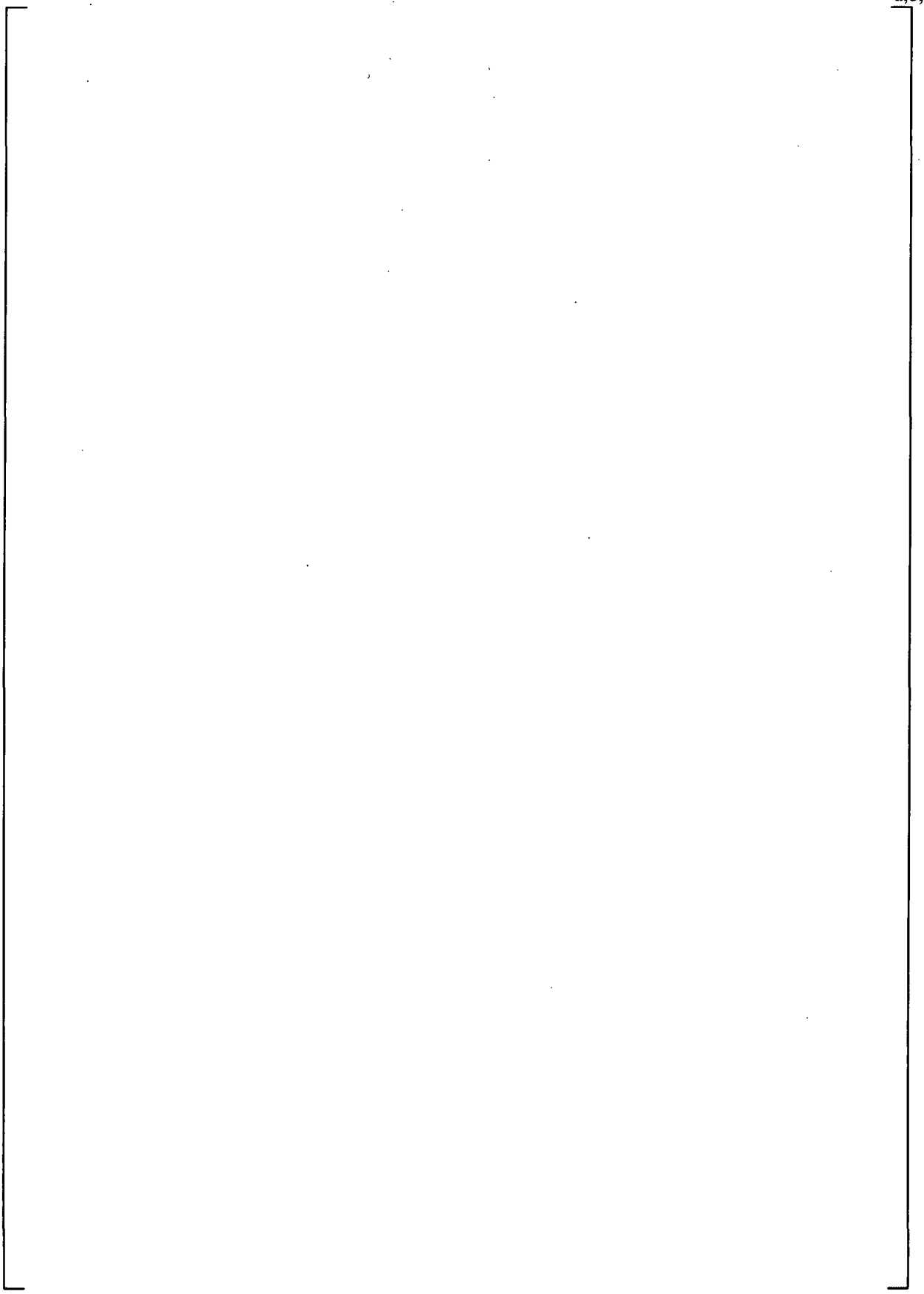

a,b,c

a,b,c

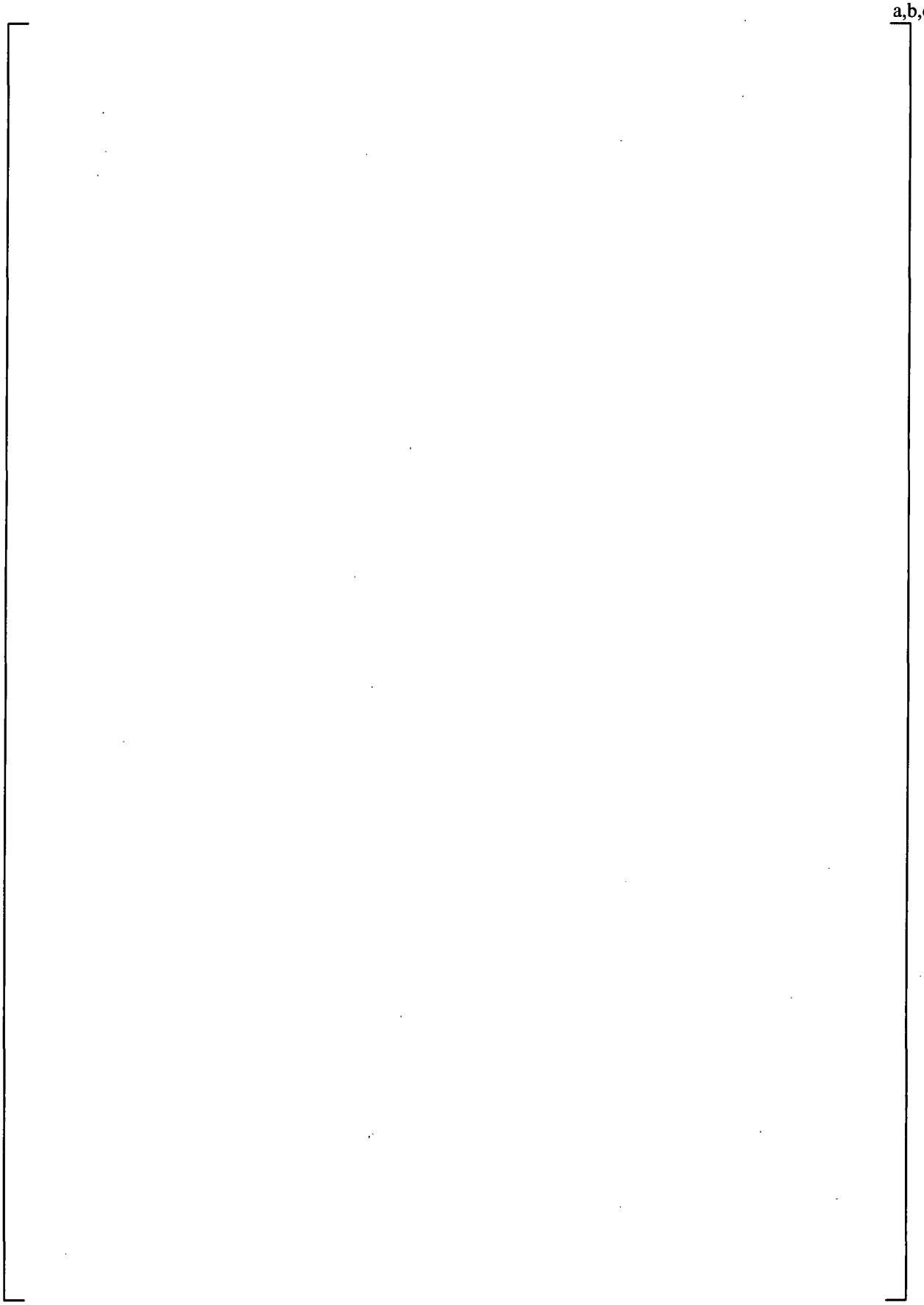

a,b,c

a,b,c

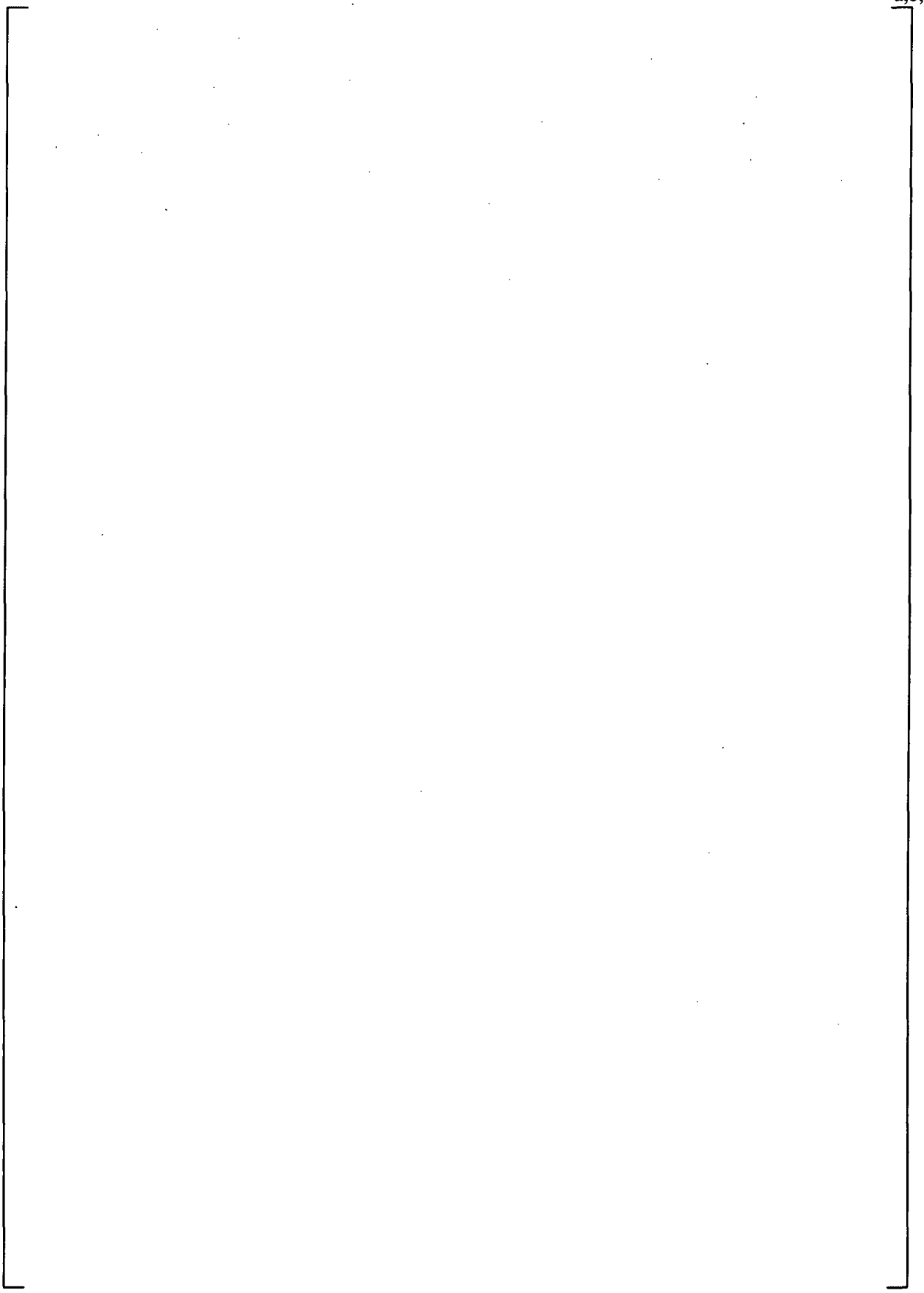

a,b,c

a,b,c

[

]

a,b,c

a,b,c

a,b,c

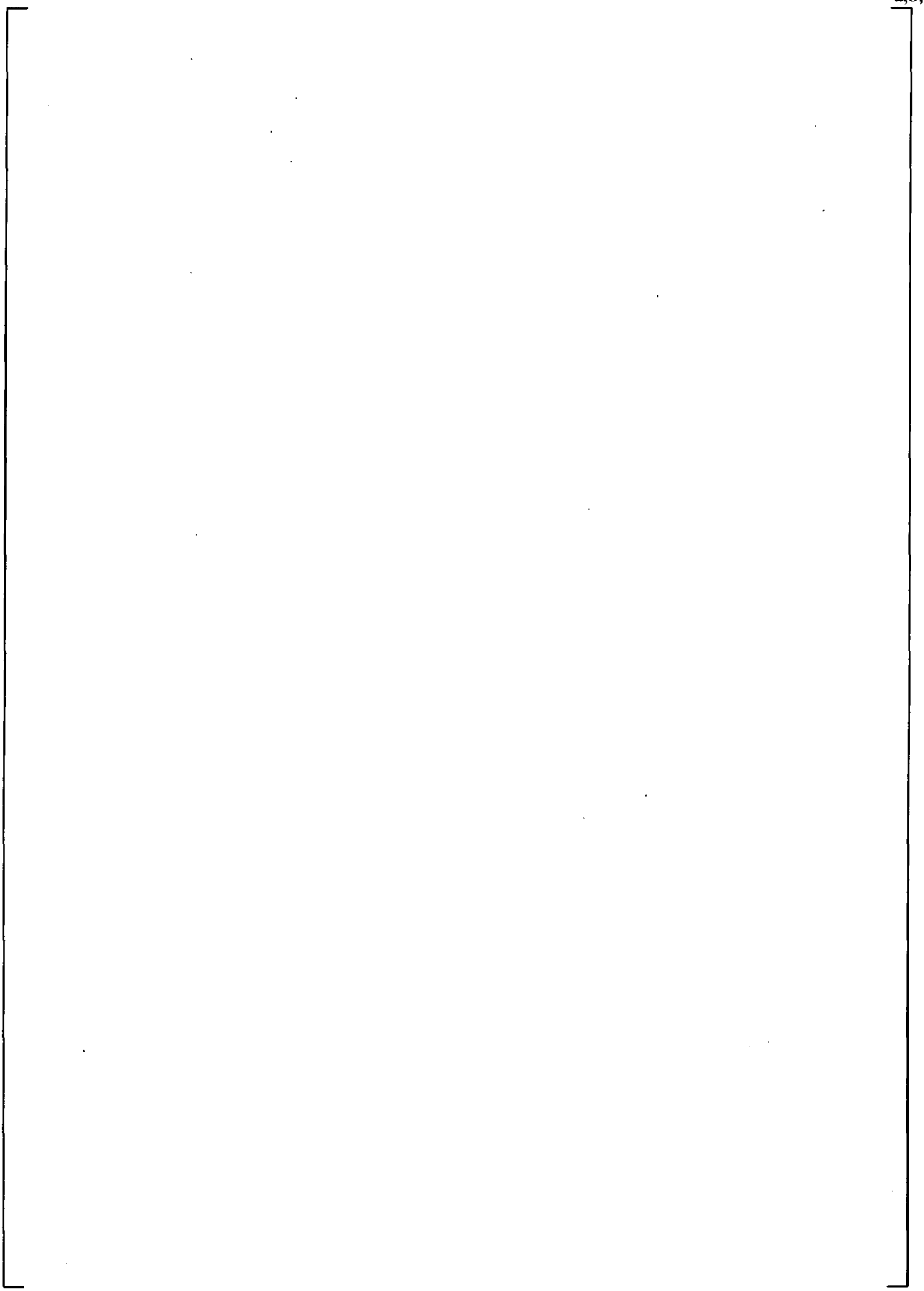

a,b,c

[

]

a,b,c

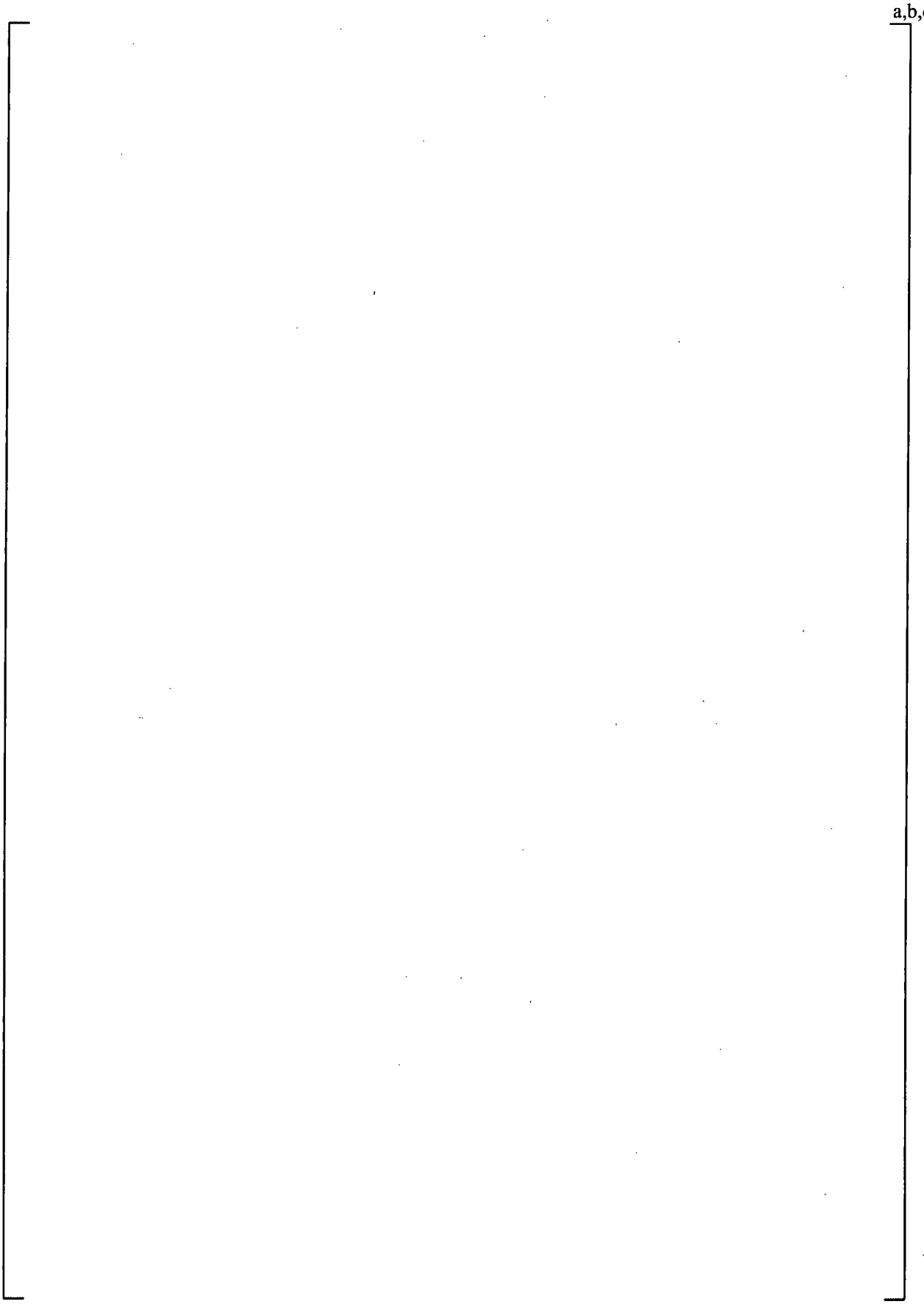

a,b,c

a,b,c

[

]

a,b,c

[

]

a,b,c

[

]

a,b,c

[

]

a,b,c

a,b,c

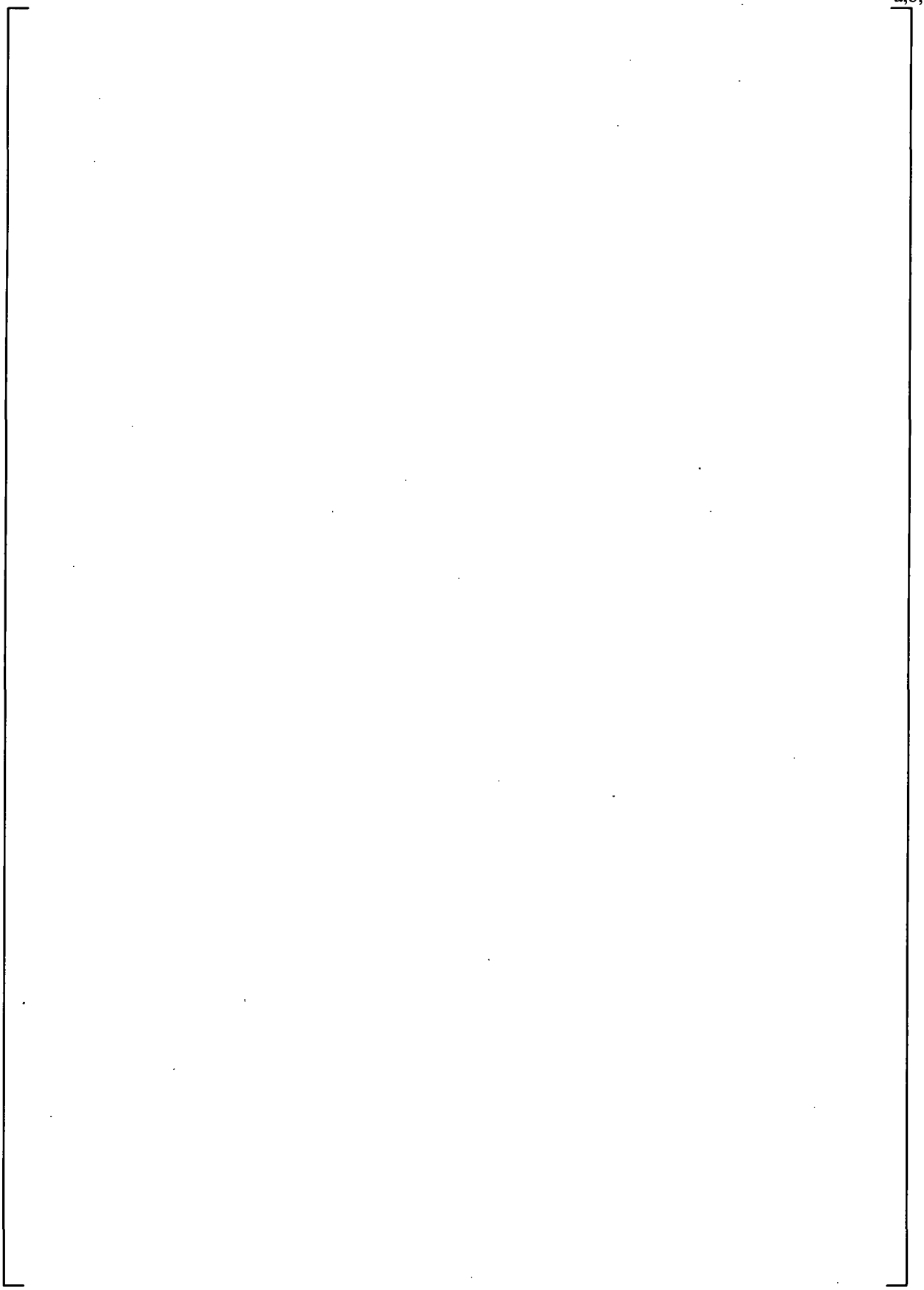

a,b,c

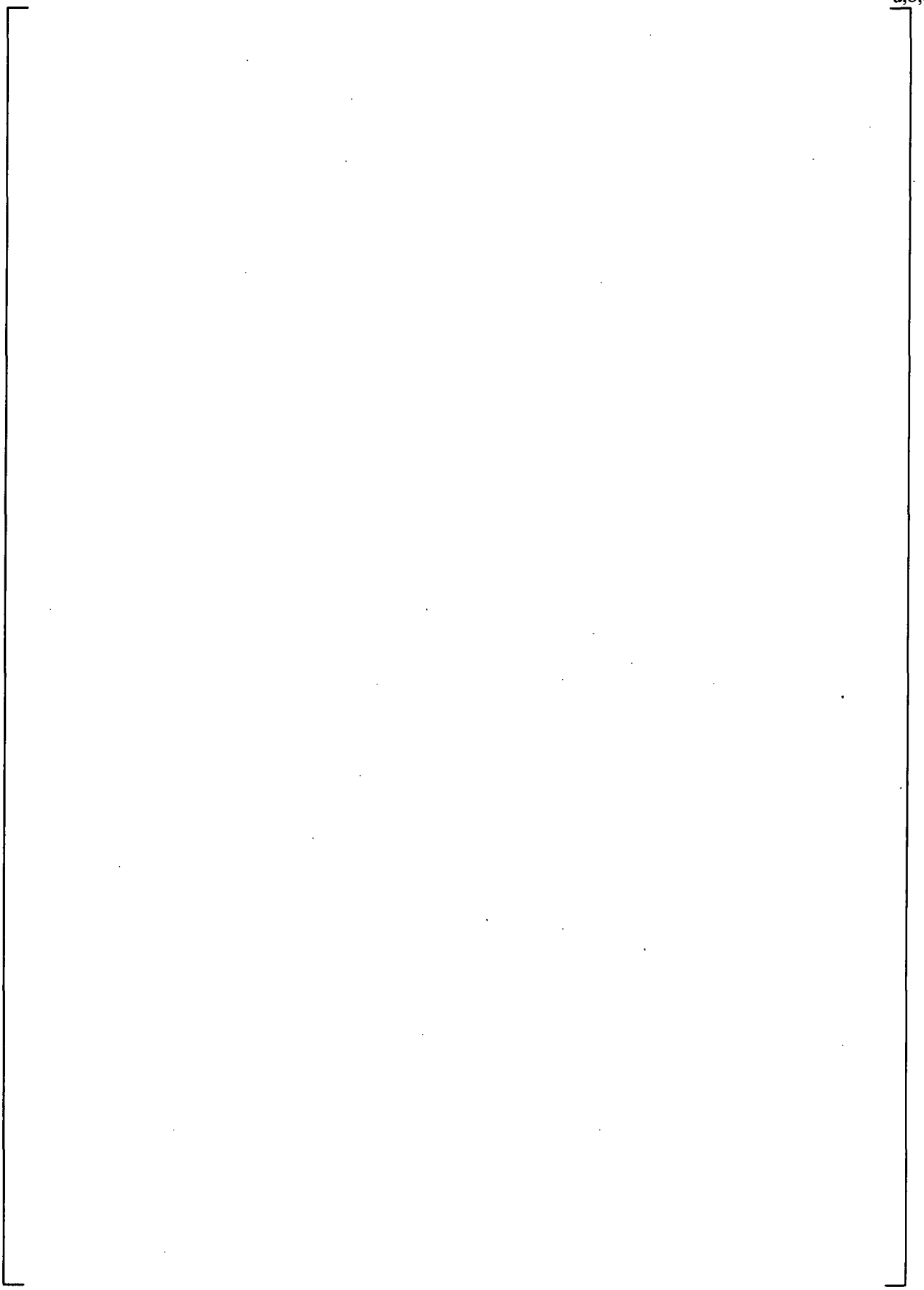

a,b,c

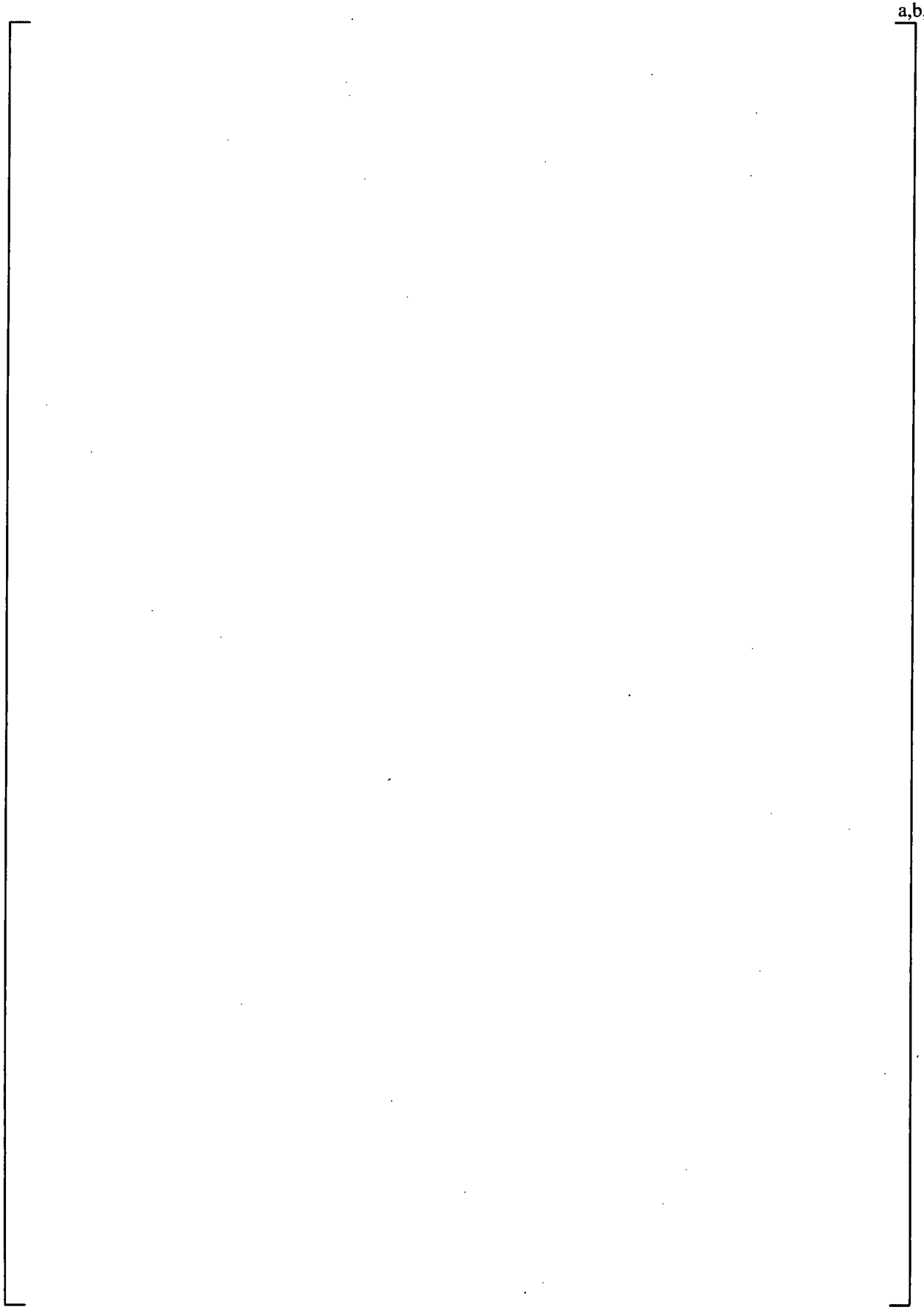

a,b,c

a,b,c

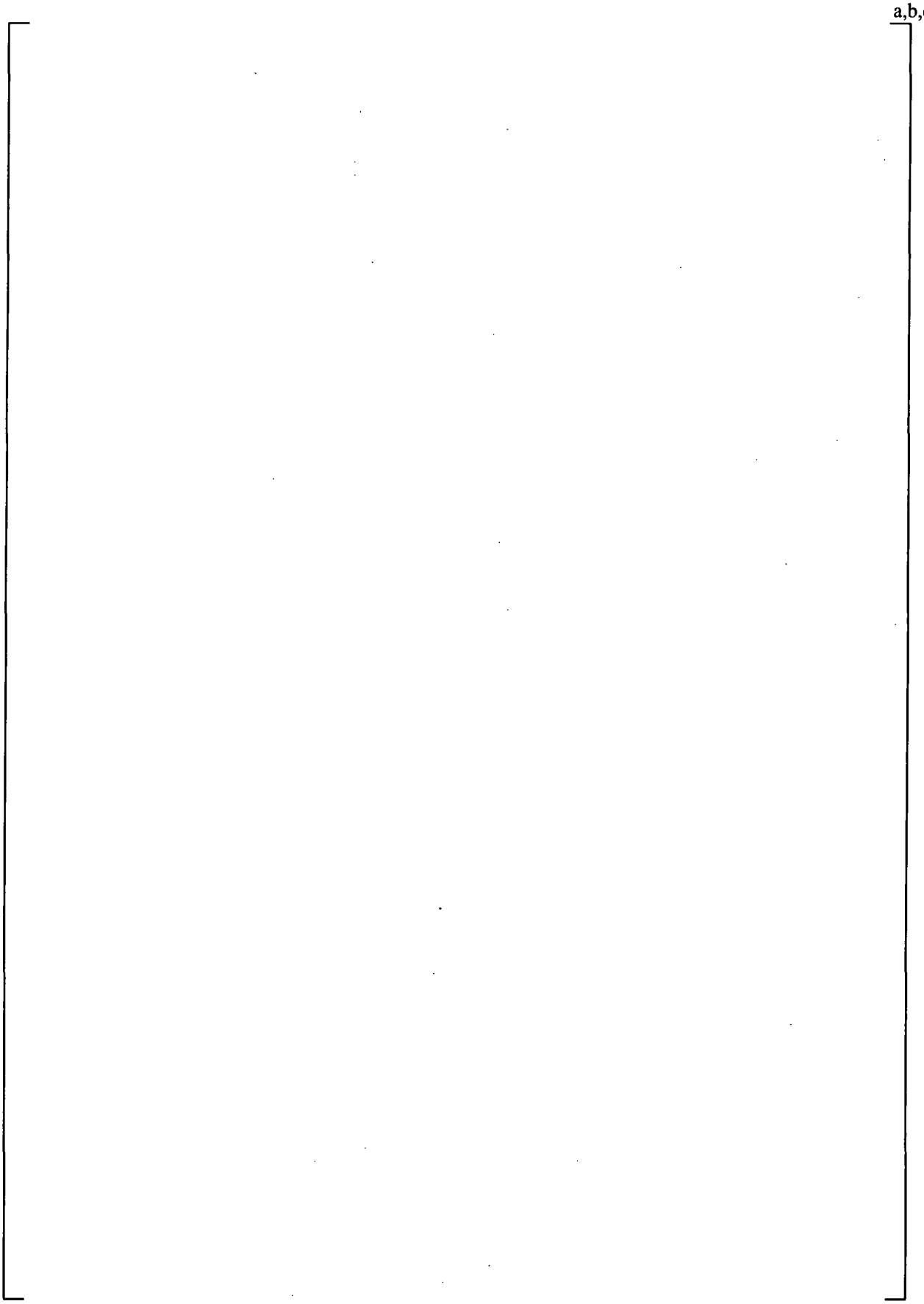

a,b,c

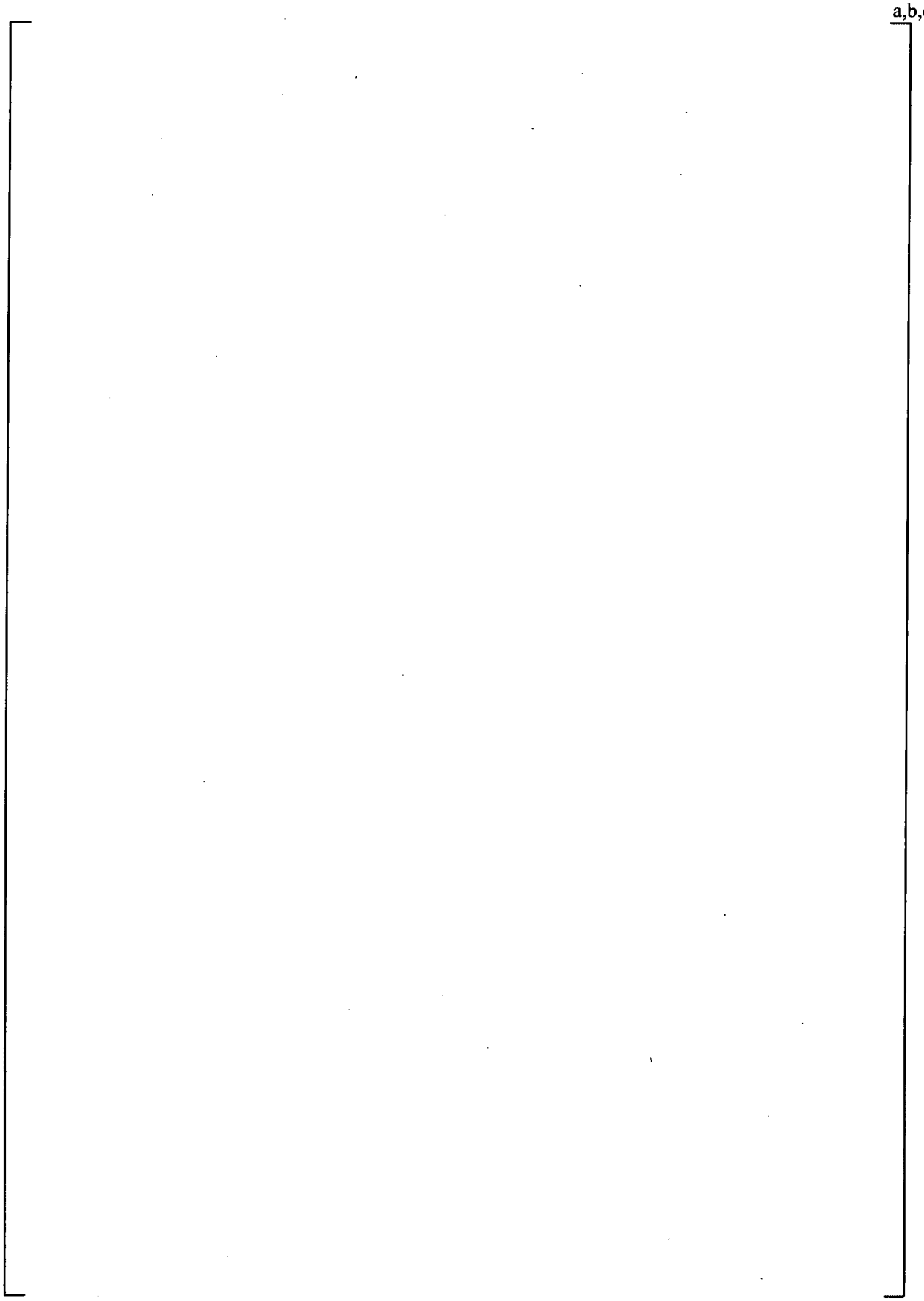

a,b,c

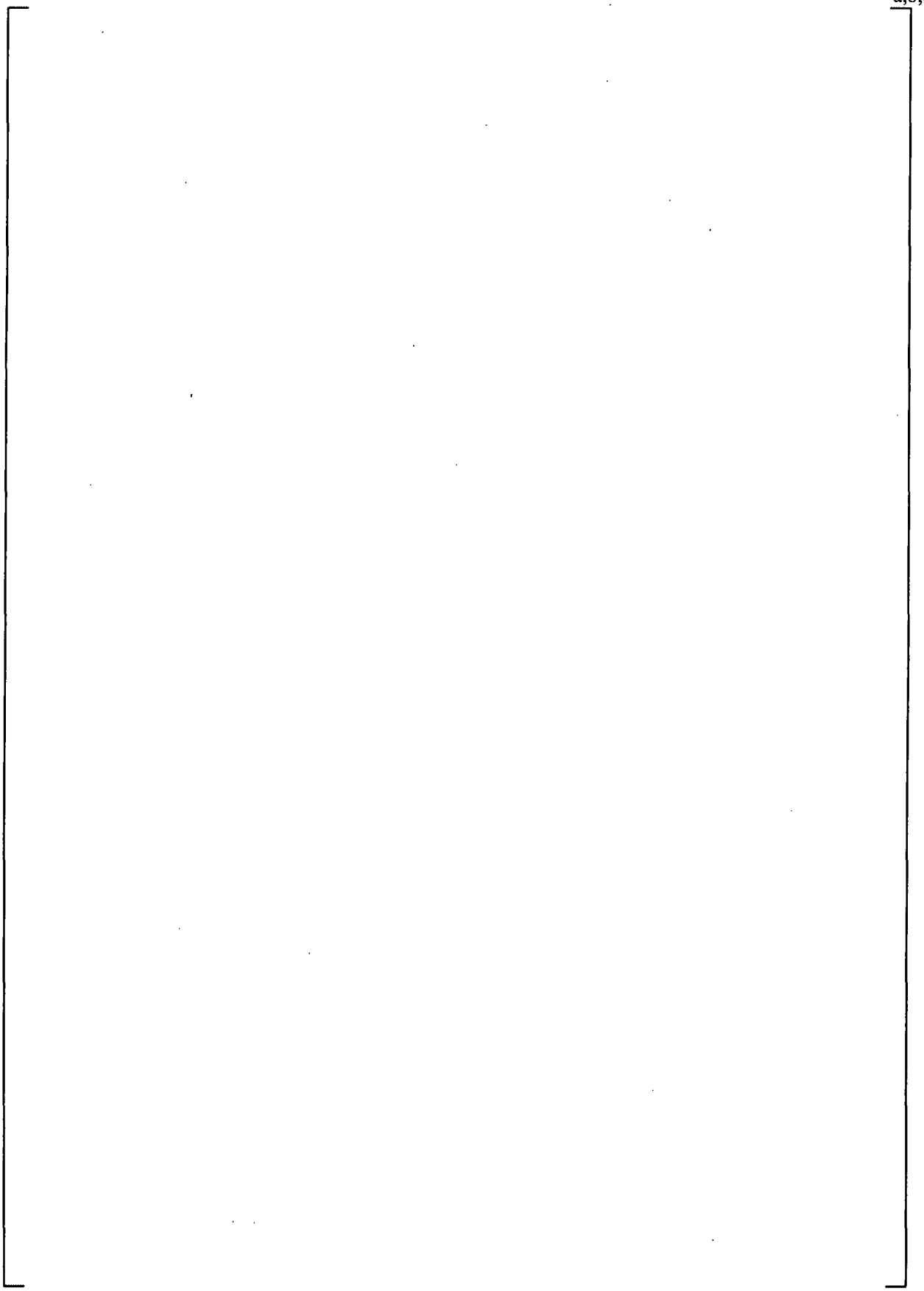

a,b,c

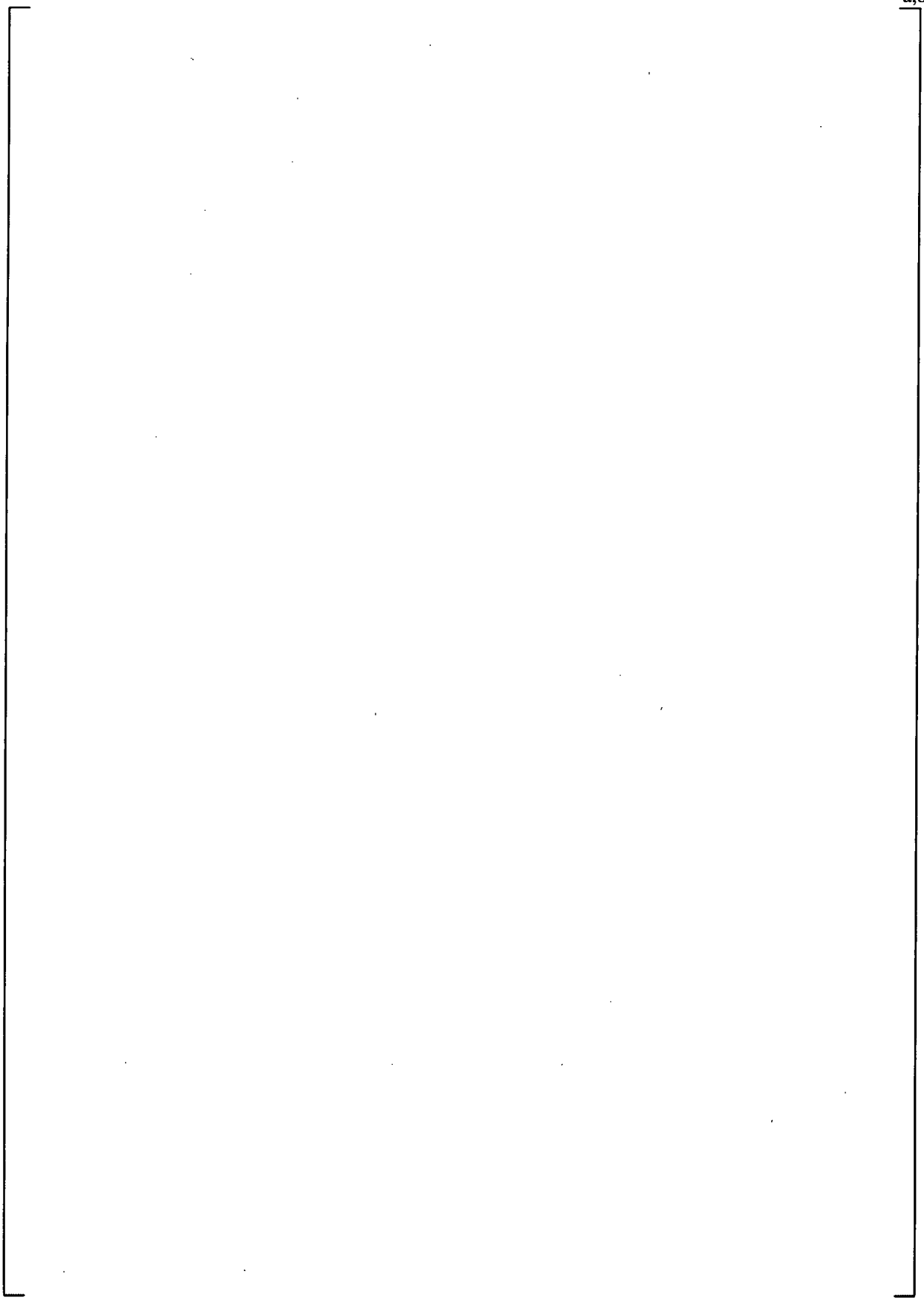

a,b,c

a,b,c

[

]

a,b,c

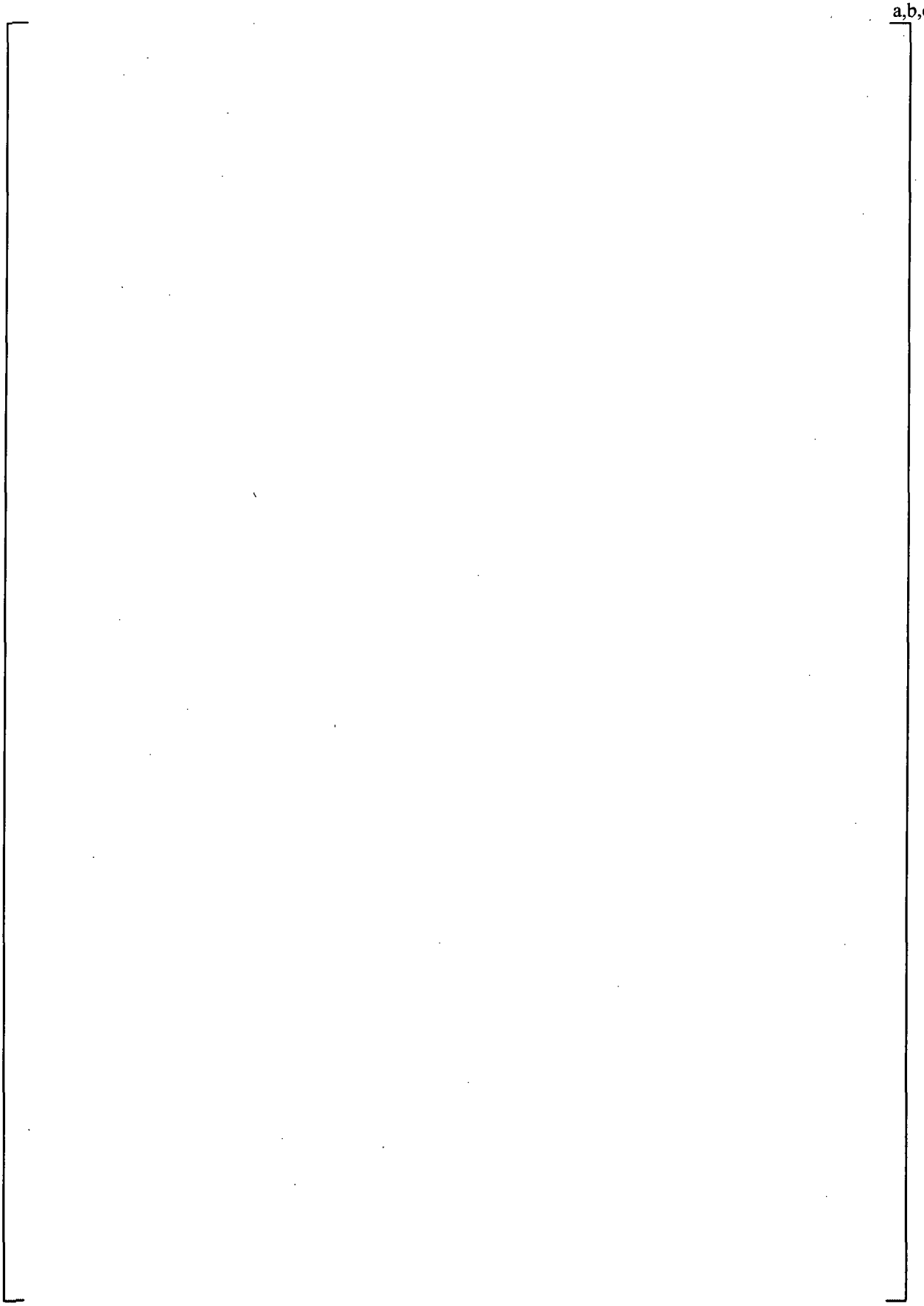

a,b,c

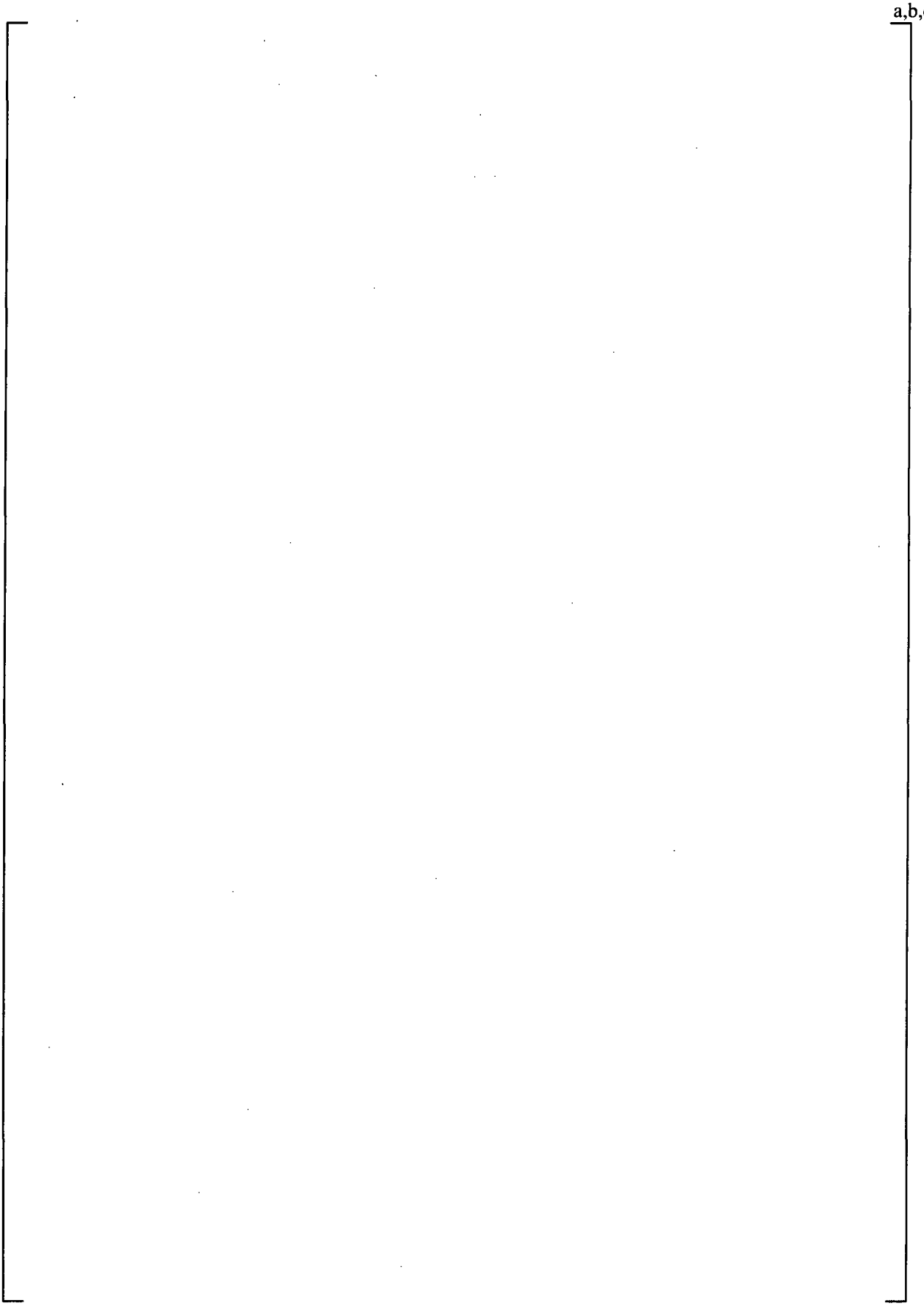

a,b,c

[

]

a,b,c

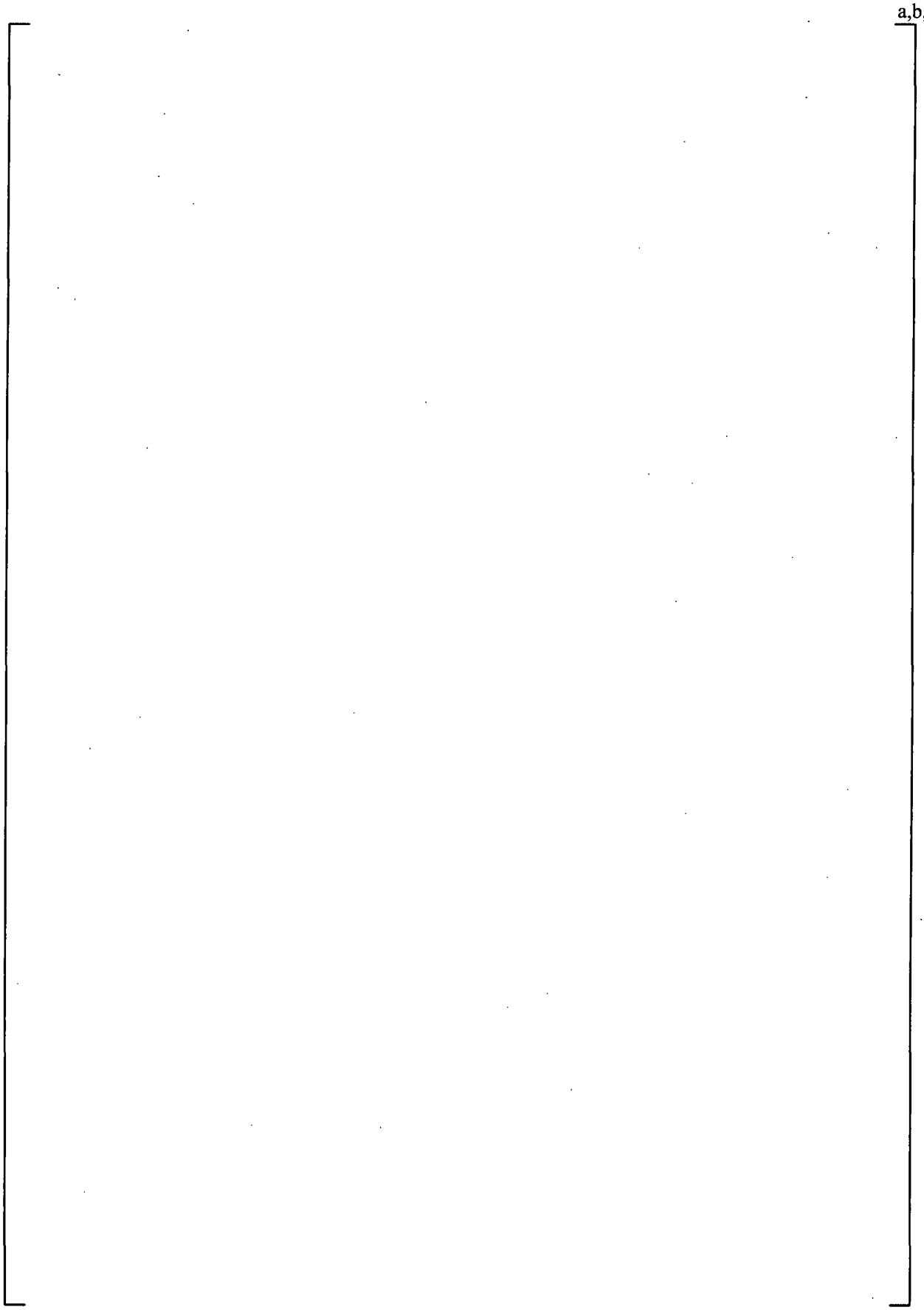

a,b,c

[

]

a,b,c

[

]

a,b,c

[

]

a,b,c

[

]

a,b,c

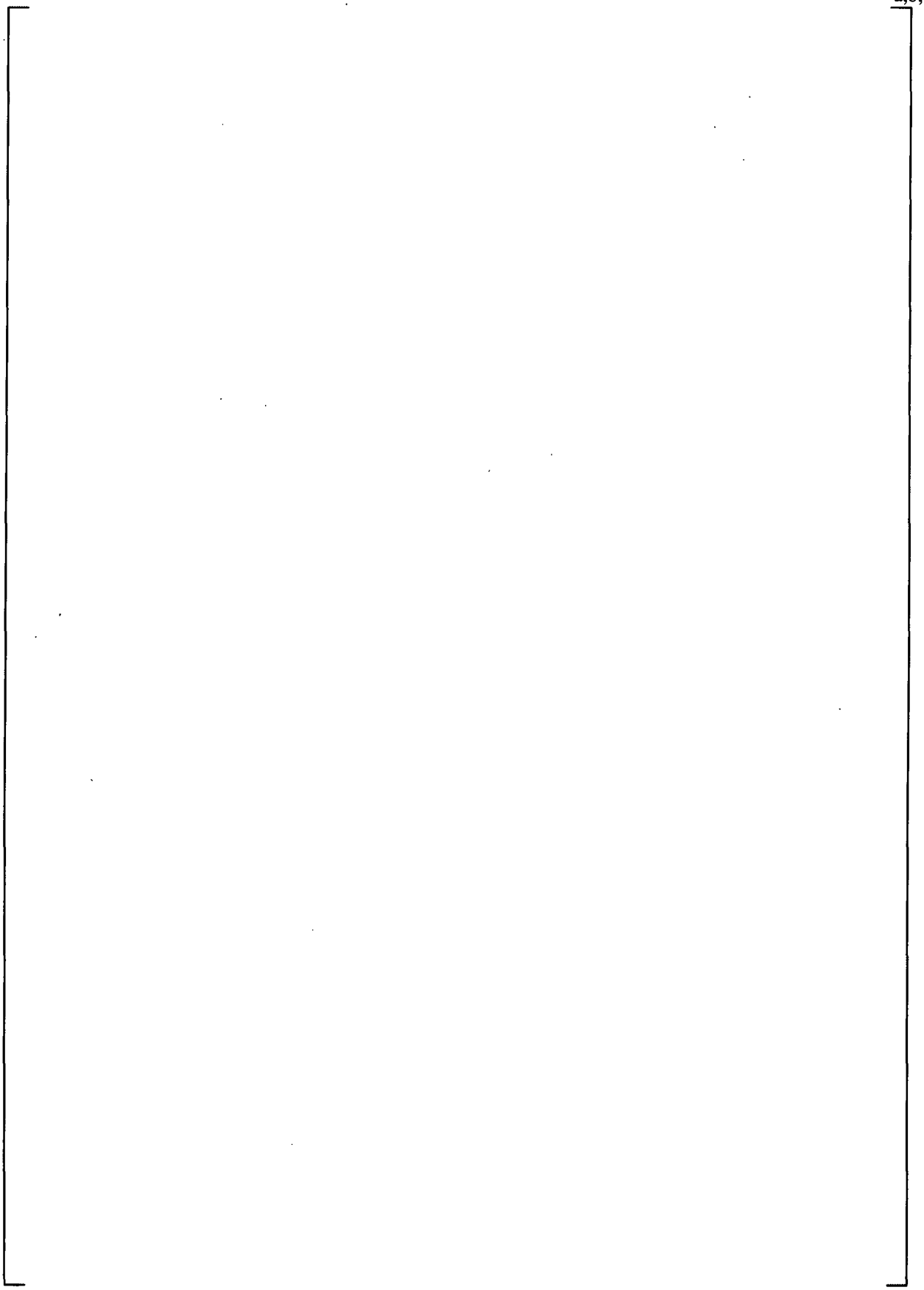

a,b,c

a,b,c

APPENDIX C
SVEA-96 OPTIMA3 STEADY STATE CRITICAL POWER TEST DATA
TOP-PEAKED AXIAL POWER SHAPE

a,b,c

a,b,c

a,b,c

[

]

a,b,c

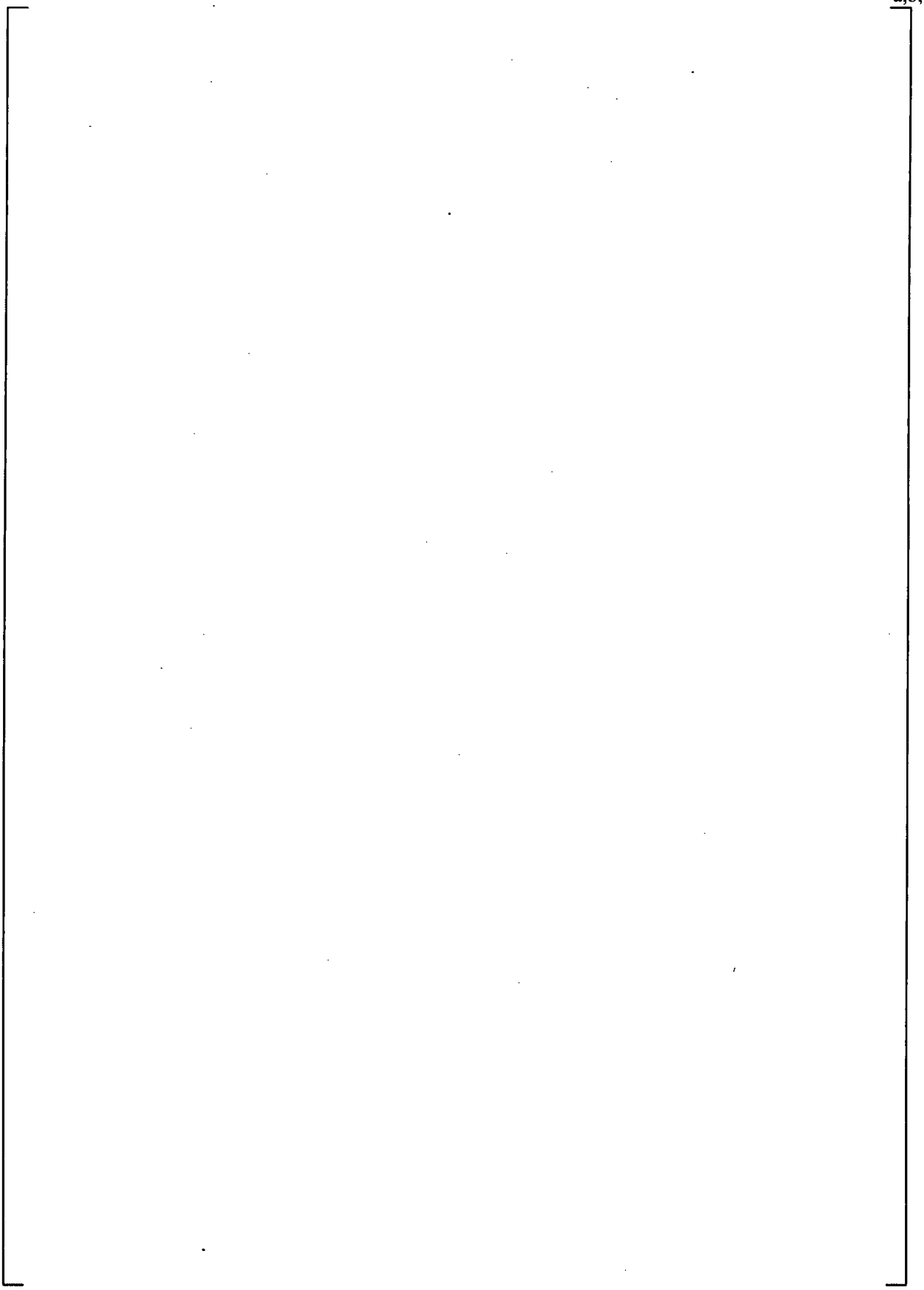

a,b,c

[

]

a,b,c

a,b,c

a,b,c

[

]

a,b,c

a,b,c

a,b,c

[

]

a,b,c

[

]

a,b,c

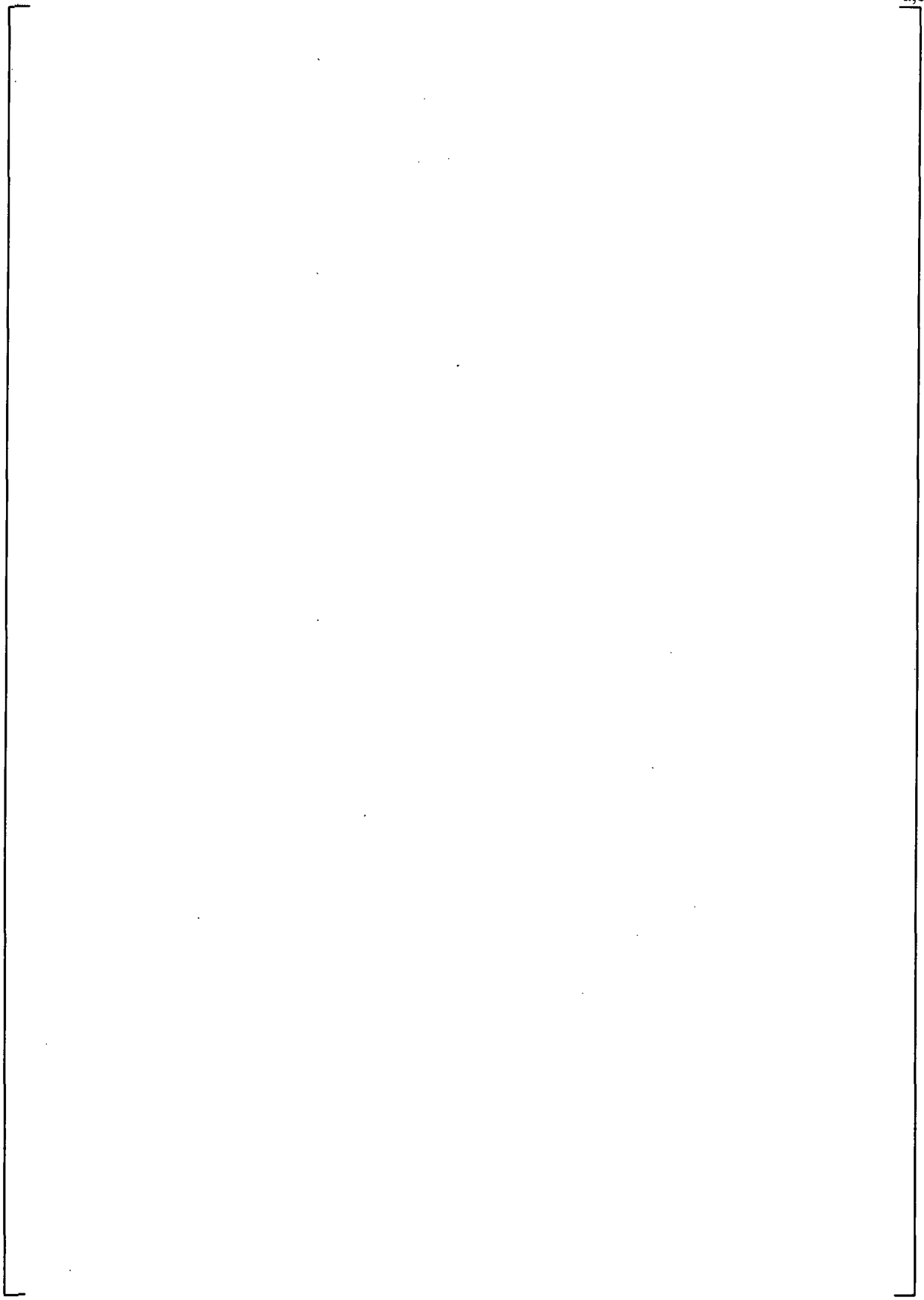

a,b,c

[

]

a,b,c

[

]

a,b,c

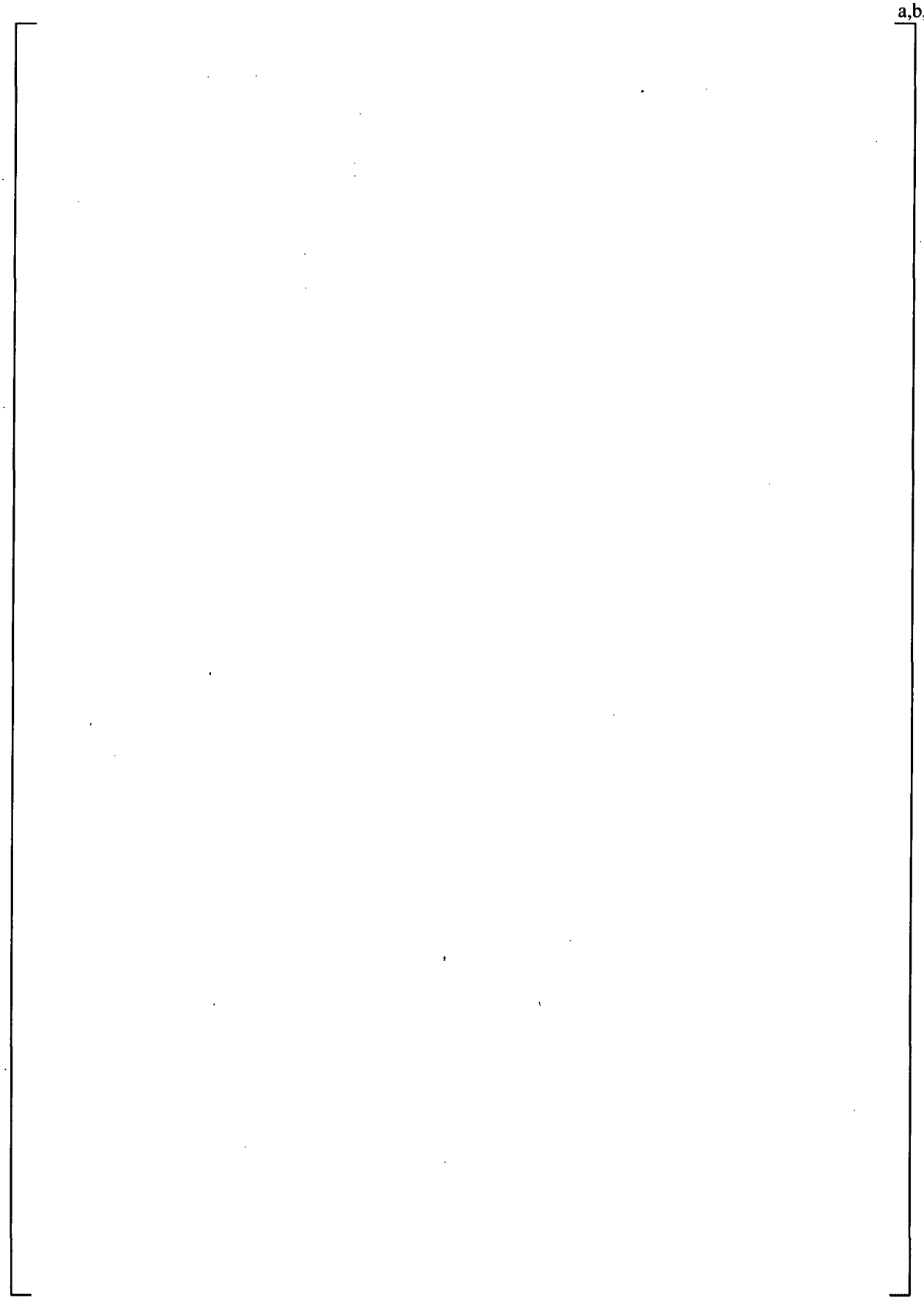

a,b,c

[

]

a,b,c

a,b,c

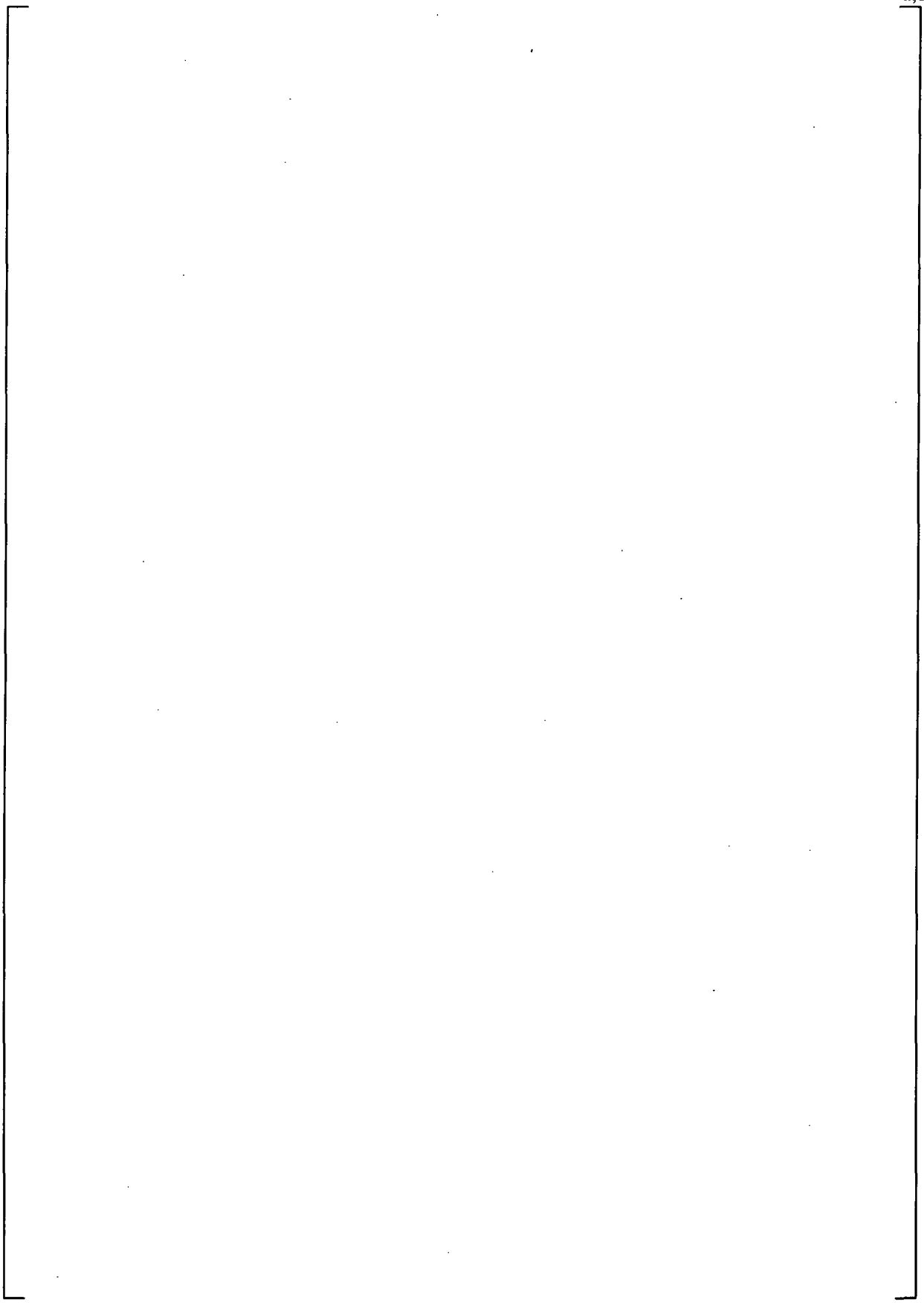

a,b,c

[

]

a,b,c

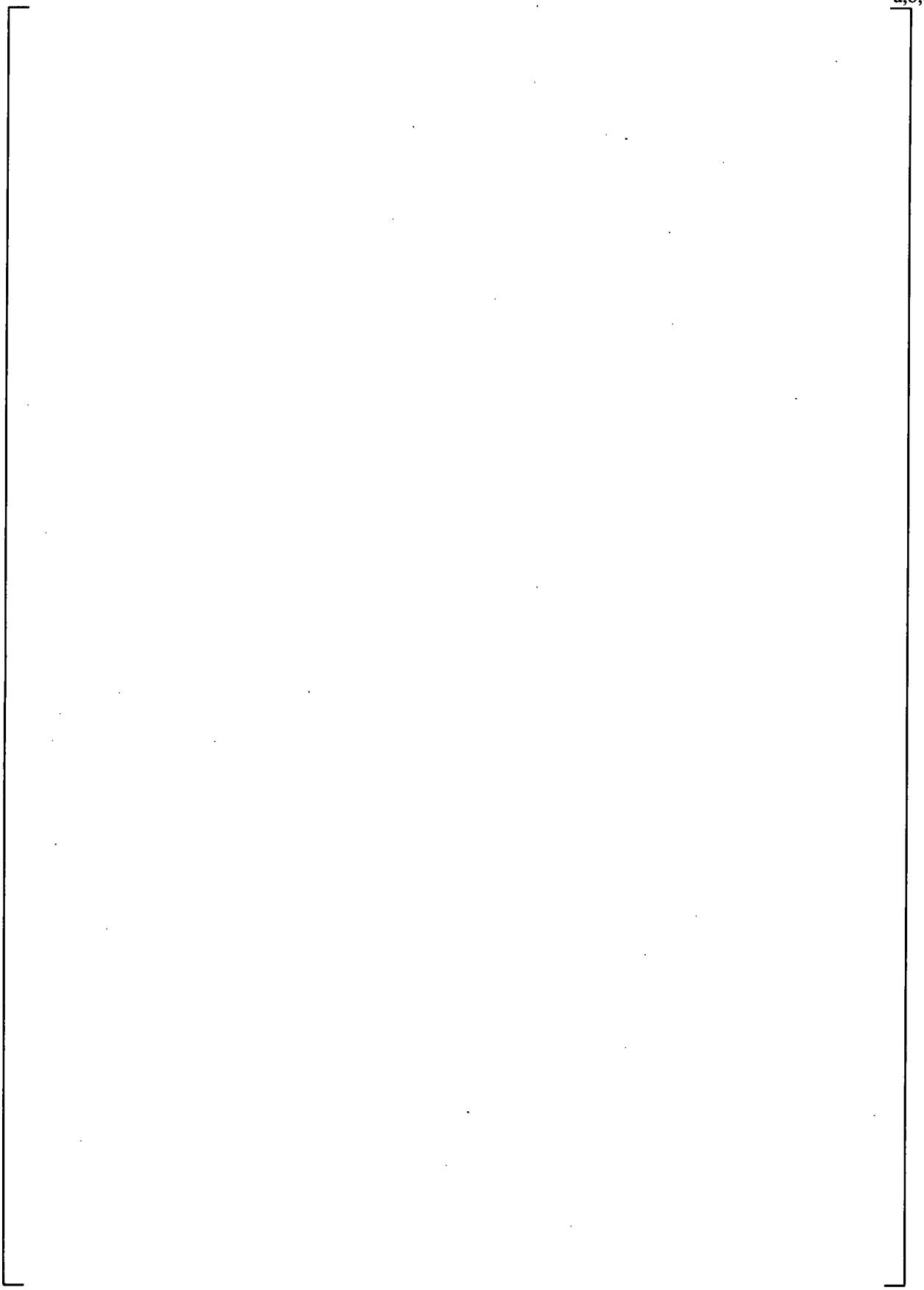

a,b,c

[

]

a,b,c

[

]

a,b,c

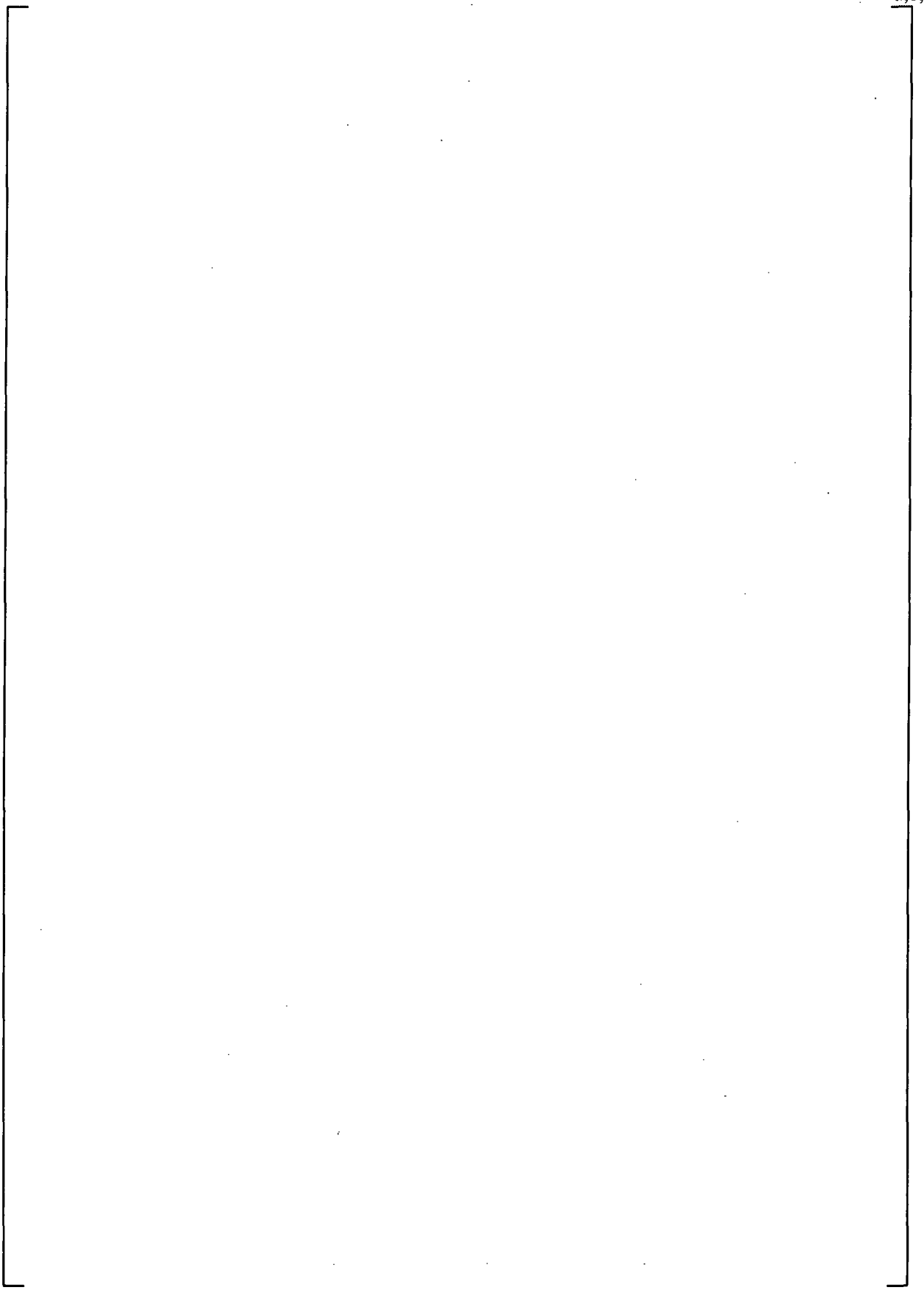

a,b,c

[

]

a,b,c

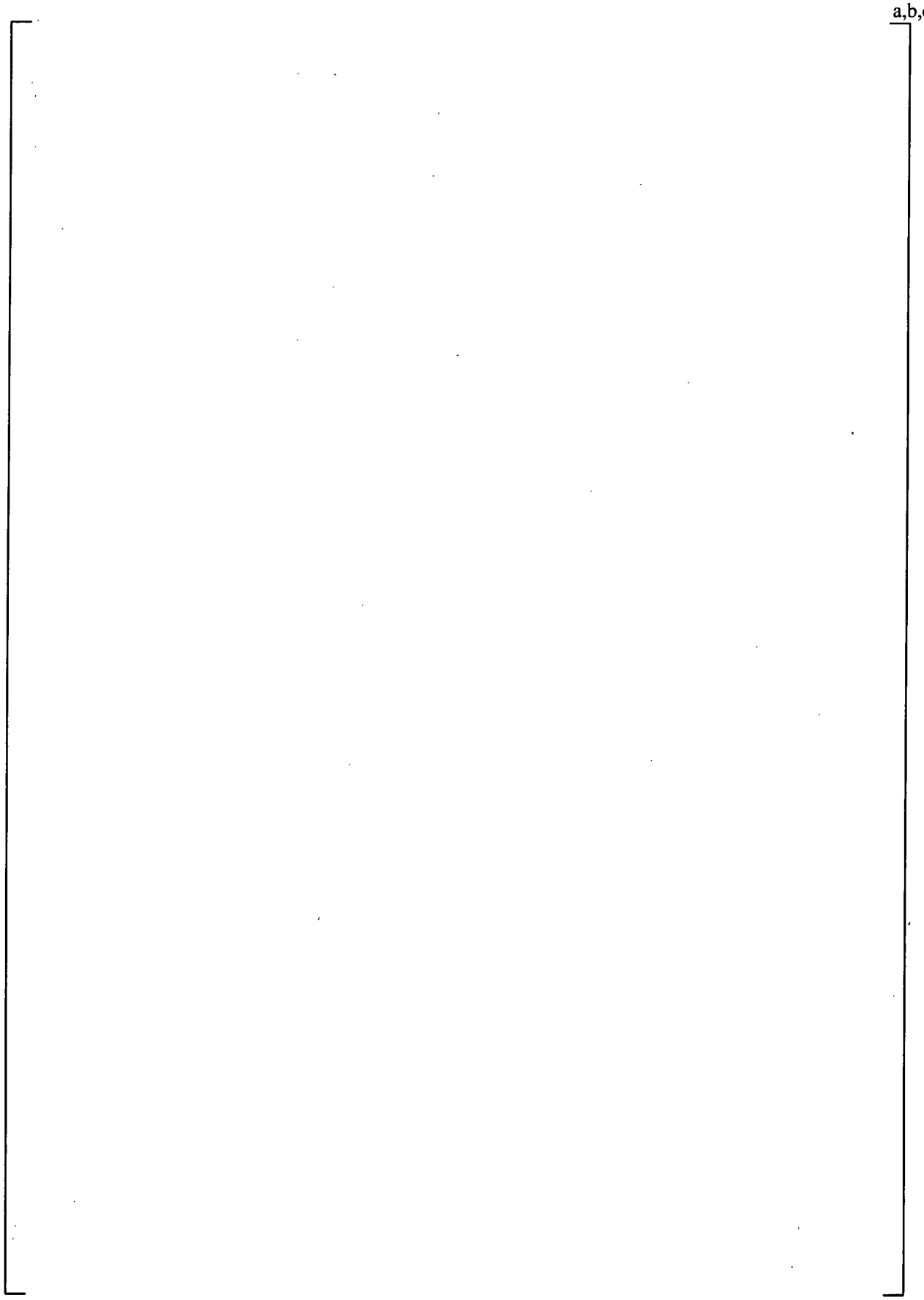

a,b,c

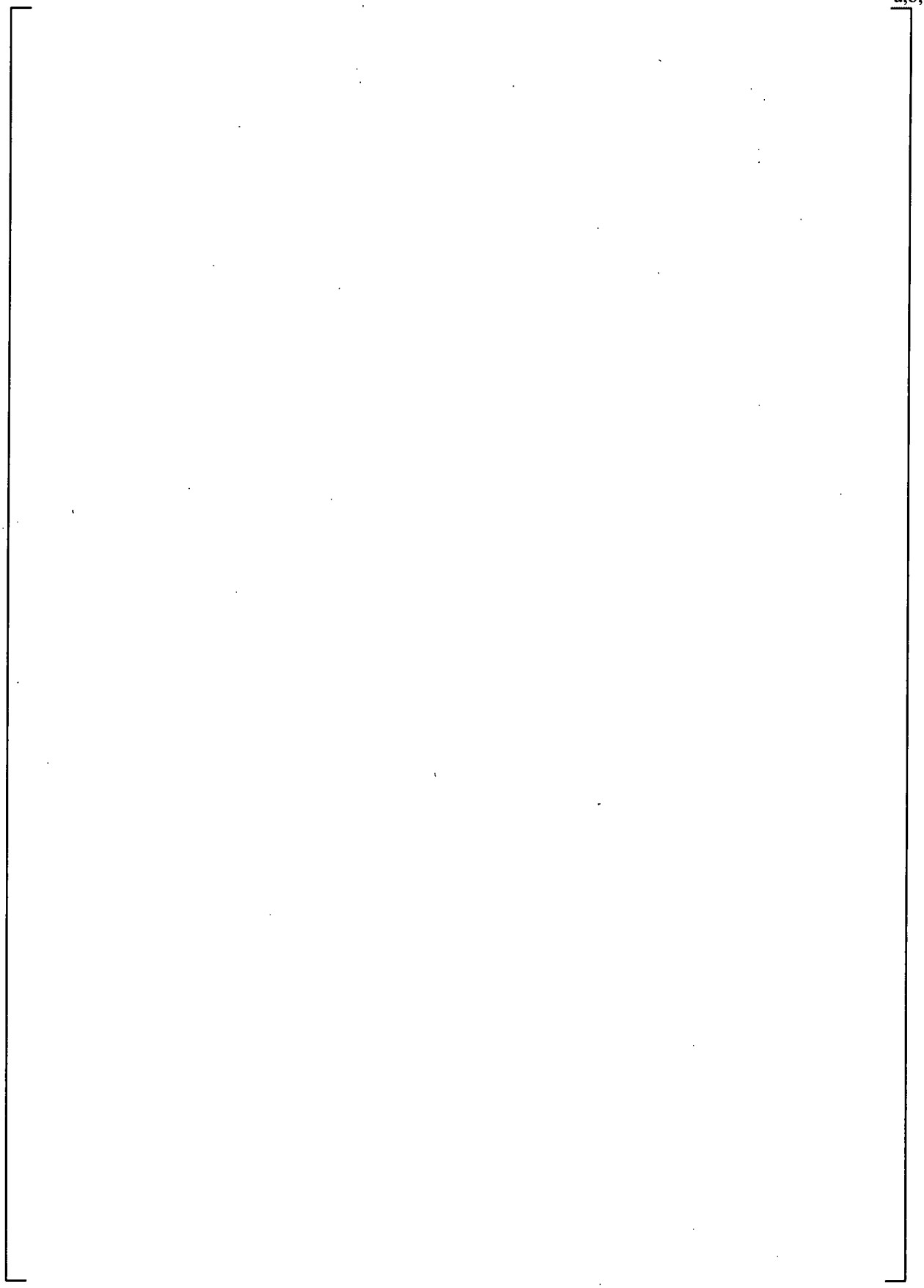

a,b,c

[

]

a,b,c

[

]

a,b,c

a,b,c

a,b,c

[

]

a,b,c

a,b,c

[

]

a,b,c

a,b,c

[

]

a,b,c

a,b,c

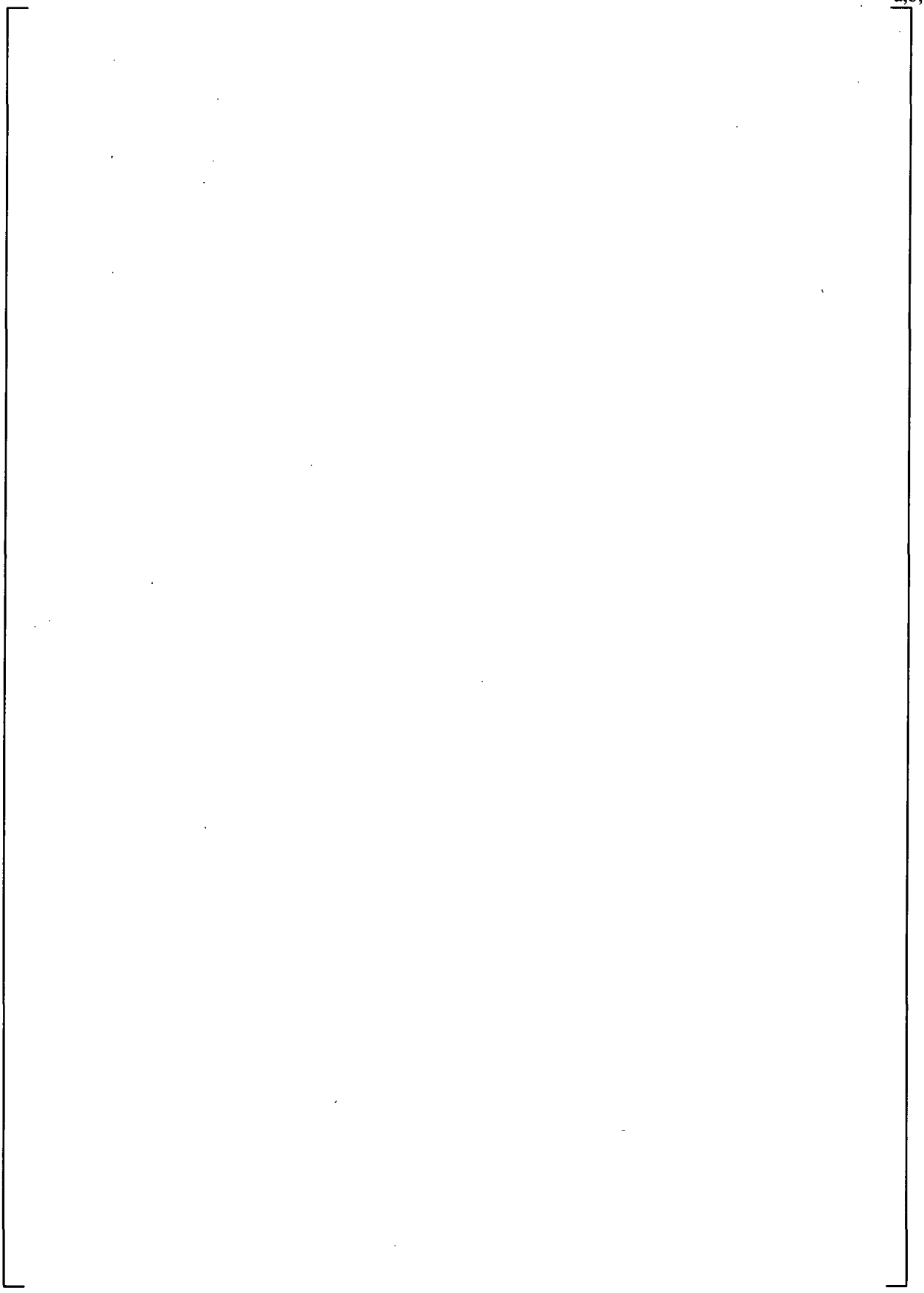

a,b,c

[

]

a,b,c